CHARACTERISATION OF NATURALLY FRACTURED RESERVOIRS USING GEOLOGICAL WELL-TESTING

DAVID OKA EGYA

Submitted for the degree of Doctor of Philosophy
Institute of Petroleum Engineering
Heriot-Watt University
August 2018

ABSTRACT

In naturally fractured reservoirs (NFR), fractures often constitute the main heterogeneities, yet the pressure responses observed in the wells may not show the conventional well-test signatures for NFR. In order to better characterise a reservoir with well-test data, it is important to properly analyse and understand the diagnostic signatures of fracture flow. Dual-porosity model is the underlying concept for interpreting well-tests data from NFR. However, pressure behaviours in real fractured reservoirs defy the simulated pressure responses corresponding to the dual-porosity model. To overcome the limitations of this model, this thesis applies a geoengineering workflow using discrete fracture-matrix modelling approach and unstructured-PEBI grid to simulate flow behaviour in fractured reservoirs. The workflow allows for a systematic correlation of the pressure responses observed in the reservoir to the known geological features in the reservoir model. Using this approach, the thesis presents new insights into why the classical dual-porosity V-shape is observed in some NFR and absent in others; explains why different unconventional pressure transient responses emerge in NFR for scenarios where fracture conductivities differ and locations of the producer within the fracture network varies; and successfully applied the theoretical findings from this research work to provide new understanding about the flow system in a newly discovered fractured offshore carbonate reservoir. Overall, this thesis provide novel reference solution for interpreting well-test data from NFR.

To my beloved wife, Jemimah and son, Jedidiah.

ACKNOWLEDGMENTS

This PhD is graciously funded by PTDF Nigeria. This research work would not have been possible without an active and indirect contribution of many incredible people that I worked or interacted with over the period of my studies. I am indebted to Sebastian Geiger who was exceptionally available to supervise my PhD research right from our first communication to this point. Thank you for your thorough feedback to this research work, all my writings and presentations, and every support. I am grateful to Patrick Corbett for the productive discussions, review of my research results and papers, and the concept of the geoengineering workflow adapted in this thesis.

This research benefited from valuable collaborations with Delft University and Lundin Norway AS. Thanks to Kevin Bisdom, Giovanni Bertotti and Jens Petter Nørgård for providing the outcrop and DST data presented in this thesis. I enjoyed working with you. Thanks to other IPE staff that I met and interacted with during my programme, including Adrian Todd, Eric Mackay, Jami Mahmoud, Florian Doster and Dan Alnold. I would also like to thank Kirsty Morton, George Stewart and Andreas Busch for agreeing to examine this piece of work for the award of a PhD. I hope you find reading and evaluating this thesis interesting.

Thanks to all the members of the great Carbonate Research Group. To Jane Wells, who provided administrative support for travels and organised Christmas dinners and other events for the group. Special thanks to Rafael for the collaboration in developing the fracture meshing code used in this research work, help with programming matters, and for sharing the LaTex template used in presenting this thesis. Thanks to Alesandro, Adnan and Zhao for the great discussions over tea and lunch breaks. My view of European, Middle Eastern and Asian culture and politics has been greatly enhanced by my regular interactions with you. My trip to the beautiful city of Muscat was made possible by the invitation from Adnan. Thanks to Emmanuel, Jackson, and others for co-labouring in His vineyard. To all the other members of the Carbonate Research Group: Simeon, Daniel, Ali, Tianshen, Saheeda, Mohammed, Fahed, Dima, Jorge, Saideep, Masoud, Mark, Julien, Victoria, Christine, Fran, Herwald, Lesley, Alfredo among others, thanks for the interactions and time shared together. Apart from gleaning from the diversity of this research group, I have learned so much about different cultures, countries and feel blessed to be part of this mini "United Nations" in Heriot-Watt University. No wonder Heriot-Watt was awarded the 2017 international university of the year.

Through the rigours of the PhD research, I also enjoyed love and friendship of many. To my beloved wife, Jemimah and son, Jedidiah who made great sacrifices, showed understanding and supported me all the way. Thanks a million times! I am also thankful to the entire families of Egya and Yabaya, and all my friends who believed in my desire for further education, and shared in my opportunities and challenges to realise it. My appreciation also goes to the International Fellowship (IF), Charlotte Chapel, Hope City, SIG4IPE, ECWA and ESM UK family for the labour of love and friendship. Thanks for the fellowship and the constant reminder to live once and with eternal perspective.

To the beautiful city of Edinburgh, you are amazing and lovely. I would remember your warm-hearted and friendly people, and your pleasant spring and summer blooms long after I forget the unpredictable Scottish weather. My time in Edinburgh has been a guided tour and you, oh Lord, have been my tour guide. You are my delight and the anchor of my soul. Thanks and praise be to you for all the people and support you provided to make my adventure worthwhile. Please take my hand, precious Lord, and lead me on.

David Egya
Edinburgh, August 2018

ACADEMIC REGISTRY

Research Thesis Submission

Name*:*			
School:	EGIS – INSTITUTE OF PETROLEUM ENGINEERING		
Version: *(i.e. First, Resubmission, Final)*		Degree Sought:	PhD

Declaration

In accordance with the appropriate regulations I hereby submit my thesis and I declare that:

1) the thesis embodies the results of my own work and has been composed by myself
2) where appropriate, I have made acknowledgement of the work of others and have made reference to work carried out in collaboration with other persons
3) the thesis is the correct version of the thesis for submission and is the same version as any electronic versions submitted*.
4) my thesis for the award referred to, deposited in the Heriot-Watt University Library, should be made available for loan or photocopying and be available via the Institutional Repository, subject to such conditions as the Librarian may require
5) I understand that as a student of the University I am required to abide by the Regulations of the University and to conform to its discipline.
6) I confirm that the thesis has been verified against plagiarism via an approved plagiarism detection application e.g. Turnitin.

* *Please note that it is the responsibility of the candidate to ensure that the correct version of the thesis is submitted.*

Signature of Candidate*:*		Date:	

Submission

Submitted By *(name in capitals):*	
Signature of Individual Submitting:	
Date Submitted:	

For Completion in the Student Service Centre (SSC)

Received in the SSC by *(name in capitals):*			
Method of Submission *(Handed in to SSC; posted through internal/external mail):*			
*E-thesis Submitted (**mandatory for final theses)***			
Signature:		Date:	

Please note this form should be bound into the submitted thesis.

CONTENTS

ACRONYMS

AF - Asymmetric Factor

BU - Build Up

DFM - Discrete Fracture-Matrix

DST - Drill Stem Test

DP - Dual-Porosity

ELR - Effective Length Ratio

EOR - Enhanced Oil Recovery

FCD - Dimensionless Fracture Conductivity

GOR - Gas-Oil-Ratio

MRST - Matlab Reservoir Simulation Toolbox

NFR - Naturally Fractured Reservoirs

OOIP - Original Oil in Place

PEBI - PErpendicular BIsector

PI - Productivity Index

PSLG - Planar Straight-Line Graph

PSS - Pseudo-steady State

PSSIF - Pseudo-steady State Inter-porosity Flow

PTA - Pressure Transient Analysis

PVT - Pressure, Volume and Temperature

REV - Representative Elementary Volume

TIF - Transient Inter-porosity Flow

WBS - Wellbore Storage Effect

PUBLICATIONS

This thesis contains excerpts from the following papers:

Egya, D., Geiger, S., Corbett, P., Bisdom, K., Bertotti, G. and Bezerra, H. (2016). Assessing the Validity and Limitations of Dual- porosity Models Using Geological Well Testing for Fractured Formations. In 78th EAGE Conference and Exhibition, Vienna, Austria.

Egya, D., Geiger, S., Corbett, P. and March, R. (2017).The effect of fracture skin, network connectivity, and network size on well-test responses in naturally fractured reservoirs. In 79th EAGE Conference and Exhibition, Paris, France.

Egya, D. O., Geiger, S., Corbett, P. W. M., March, R., Bisdom, K., Bertotti, G. and Bezerra, F. H. (2018). Analysing the limitations of the dual-porosity response during well tests in naturally fractured reservoirs, Petroleum Geoscience. https://doi.org/10.1144/petgeo2017-053.

Egya, D., Geiger, S., Corbett, P., Norgard, J. P., Hegndal-Andersen, S. and Sundal, L. (2018). New calibration of fracture properties using geological well-testing, Third EAGE Workshop on Naturally Fractured Reservoirs, Muskat, Oman.

Egya, D., Geiger, S., Corbett, P. W. M. (2018). Effect of Variation in Fractures Conductivity and Well Location on Pressure Transient Response from Fractured Reservoirs, SPE EUROPEC/EAGE Conference and Exhibition, Copenhagen, Denmark. Accepted for Journal publication

Egya, D., Geiger, S., Corbett, P. W. M., Norgard, J. P., Hegndal-Andersen, S. and Sundal, L. (2018). Calibration of dual-porosity systems using geological well-testing - a case study from the Norwegian North Sea. To be submitted for peer-review.

1

INTRODUCTION AND BACKGROUND

1.1 INTRODUCTION

Naturally fractured reservoirs (NFR) account for a significant volume of the remaining conventional hydrocarbons and represent some of the most productive fields across the globe (Aguilera, 1998; Bratton et al., 2006; Lemonnier and Bourbiaux, 2010b). A major part of these reserves - over 60% of the world's proven oil and 40% of the world's gas reserves, are contained in fractured carbonates reservoirs (Schlumberger, 2008). Fractures often influence production behaviour in naturally fractured reservoirs (NFR). They can dominate reservoir performance and recovery from the initial primary recovery to tertiary (enhanced oil) recovery. They create exploration targets in otherwise low-permeability reservoirs by providing an interface with the matrix that contains the hydrocarbons, thereby facilitating hydrocarbon charge into a producer and enhancing production rates for a given pressure drop (Nelson, 2001; Luo et al., 2017). Apart from increasing the productivity of a reservoir, fractures can also impede hydrocarbon production and recovery by acting as baffles and barriers to flow (Bourbiaux, 2010; Spence et al., 2014).

Modelling and characterisation of NFR have a wide range of geoscience applications, including hydrocarbon recovery, hydrogeology, waste management, or geothermal energy resources (Aguilera, 1983; Pruess, 1990; Berkowitz, 2002; Geiger and Emmanuel, 2010; Flemisch et al., 2017). Characterising flow behaviour in fractured formations from both static and dynamic data is difficult because of the heterogeneity and complex geometry of fractured networks. Hence, analysing, quantifying, and modelling the impact of multiscale fractures on reservoir performance and recovery remains a challenging task to multiple disciplines, and is particularly constrained by limited availability of data (Bratton et al., 2006). To improve the exploitation of hydrocarbons from NFR, we need to improve our understanding of the nature and behaviour of the fractures and the degree to which they influence reservoir performance during the field development. This knowledge enables us to develop suitable field development strategies for NFR, such as the positioning of wells, planning of water flooding and the design of

improved oil and enhanced oil recovery methods (Beliveau et al., 1993; Wei et al., 1998; Nelson, 2001; Fernø, 2012).

Many geological and engineering techniques are often integrated to first detect the presence and extent of fractures in a reservoir; secondly to characterise and model the fractures; lastly to understand whether the fractures enhance production or provide barriers to fluid flow. (Brown, 2010; Spence et al., 2014). Outcrop-based analogues are used to complement other information as they allow a more direct and detailed observation of the key geological features and principal reservoir properties that control reservoir performance (Monsen et al., 2006; Geiger and Matthäi, 2014; Agada et al., 2014). Nonetheless, characterising flow behaviour in fractured formations from both static and dynamic data remains a challenging task. Fracture characterisation methods of particular interest to this research work are related to the analysis of well-test data from NFR and the linking of the inherent pressure behaviours to the subsurface reservoir geology.

1.2 RESEARCH BACKGROUND

The dual-porosity model (also sometimes referred to as the double-porosity model) is an important concept for modelling and interpreting flow processes in NFR (Warren and Root, 1963; Gringarten, 1984, 1987; Moench, 1984; Chen, 1989). This model was first proposed by Barenblatt et al. (1960) to simulate flow behaviour in fractured reservoirs and developed by Warren and Root (1963) to model pressure transient behaviour in well-test from NFR (Figure 1.1). It has been the industry standard for modelling NFR and interpreting well-test data from NFR for more than 50 years (Chen, 1989; Cinco-Ley, 1996; Bourdet, 2002; Syihab, 2009; Lemonnier and Bourbiaux, 2010a; Kuchuk and Biryukov, 2014; Morton et al., 2015). The general assumptions of the dual-porosity model are:

i. The dual-porosity model consists of two regions with distinct porosities and permeability, representing the matrix and fractures within the formation (Figure 1.1).

ii. The matrix constitutes the region with negligible flow capacity but significant pore volume that is providing the primary porosity to the reservoir system.

iii. The fracture system provides the main flow path and capacity for fluid flow from the formation to the well but has low porosity (i.e. storage).

iv. Flow can occur between the matrix and fractures, but flow cannot occur between matrix blocks or from the matrix directly into the well.

v. The inter-porosity flow from matrix to fractures occurs under pseudo-steady state (PSS) conditions. PSS inter-porosity flow (PSSIF) in a dual-porosity model supposes that at any given time, the flow and pressure at all points in the matrix blocks are distributed equally, resulting in uniform transfer within the matrix and between the matrix to fracture.

vi. The dual-porosity model assumes a continuum approach in which matrix and fracture systems are considered continuous and uniform at the scale of a reservoir model grid block.

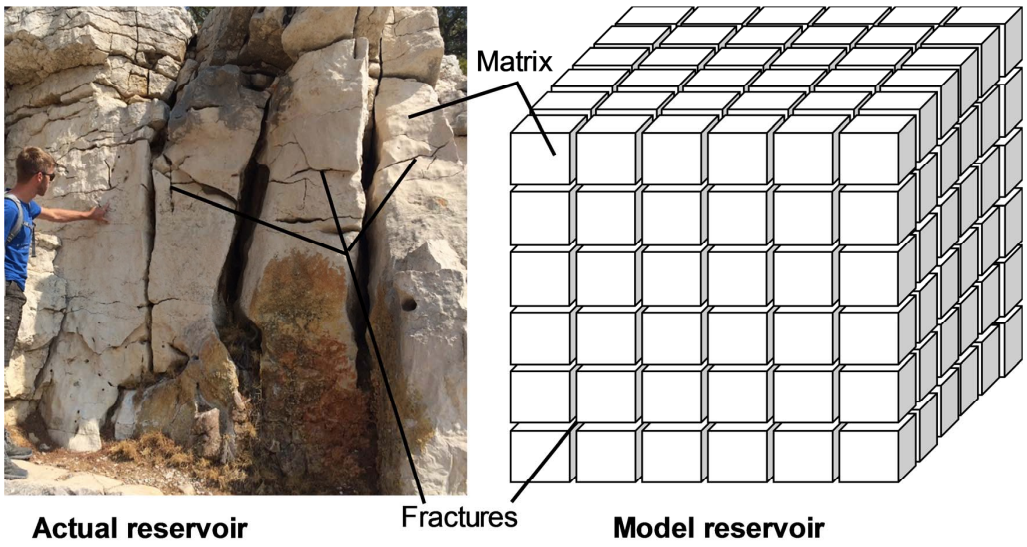

Figure 1.1: Idealisation of a dual-porosity medium. (a) Fractured and jointed carbonate reservoir image at the well-test scale at Cap Câble (Barremian, Lower Cretaceous, Cassis, France) which is a world-class reservoir analogue for many fractured carbonate fields, and (b) reservoir simulation model. After Warren and Root (1963).

Nelson (2001) classified NFR into four main categories depending on the contribution of fractures to the reservoir quality and recovery, namely Type 1, 2, 3, and 4 reservoirs (Figure 1.2).

Type 1: Fractures provide all the porosity and permeability of the reservoir. Most hydrocarbon fields in this category contain high fracture density. Early and accurate estimate of fracture width (or conductivity), spacing, and fracture volume are necessary for reserve estimates, determination of well spacing and rates, and pressure maintenance in the drainage area. Examples of Type 1 reservoirs are fractured basement reservoirs.

Type 2: Fractures provide the essential reservoir permeability while the rock matrix provides the storage. In this category, fractures control flow in the reservoir and hence an early estimate of fracture conductivity is critical for adequate reservoir management decisions. As most of the storage is in the rock matrix, an estimate of fracture volume is not critical for Type 2 reservoirs, in contrast

to Type 1. On the other hand, knowledge of fracture and matrix exchange is needed to evaluate how effectively hydrocarbons stored in matrix can replenish the fractures to maintain productivity once the fractures are depleted. Examples of Type 2 reservoirs are Agha Jari field (Iran), La Paz/Mara field (Venezuela), and Rangely field (Colorado).

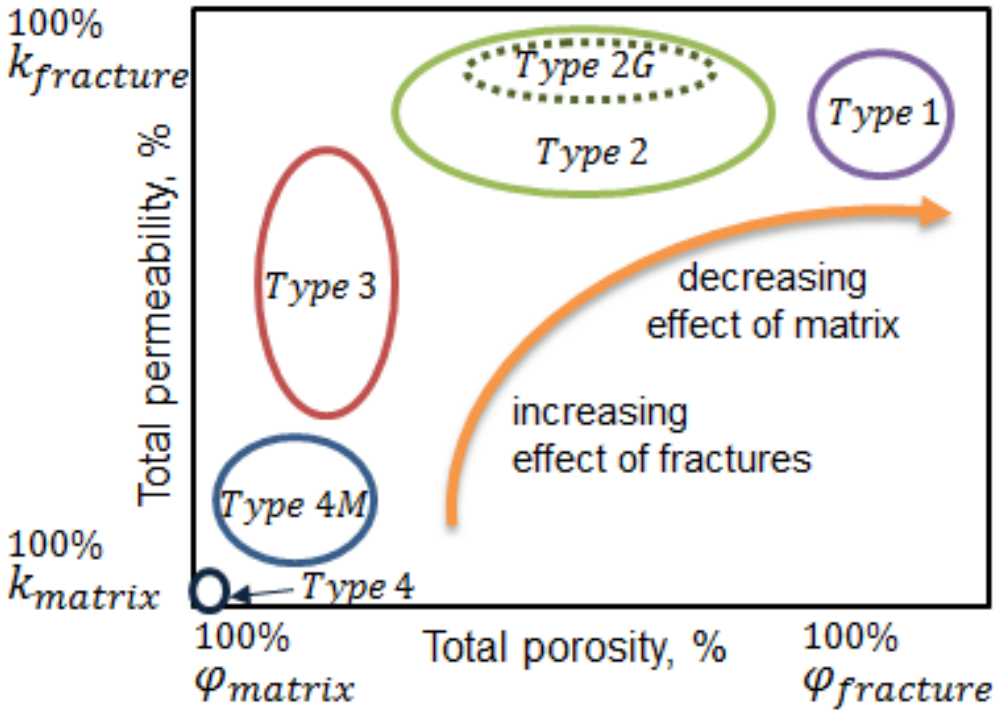

Figure 1.2: Nelson's classification of NFR. After Nelson (2001).

Type 3: Fractures contribute to but do not control reservoir permeability. The permeability of fractures can be similar to that of Type 2. However, it is only in addition to an already producible reservoir because the matrix has good porosity and permeability. Examples of Type 3 reservoirs are Kirkuk field (Iraq), Lacq field (France), and Dukhan field (Qatar).

Type 4: Fractures contribute no additional porosity or permeability but instead create barriers to reservoir flow, impeding reservoir performance.

Within Nelson's classification of NFR, other categories or special subsets of reservoirs have been identified. These include Type G and M (simply referred here as Type 2G and 4M, respectively, in Figure 1.2 because they are subset of Type 2 and 4 reservoirs in Nelson's classification scheme). Type 2G are unconventional fractured gas reservoirs (e.g. coalbed methane and fractured gas-condensate reservoirs) (Bratton et al., 2006; Vasilev et al., 2016). Most reservoirs of this category are either subsets of or similar to the characteristics to Type 2 reservoirs. Type 4M are reservoirs with a high-quality matrix porosity and permeability but may sometimes contain fractures that act as barriers to flow. Fractures in this type of reservoirs have negative impact on productivity as the

reservoirs underperform in terms of production and recovery compared to unfractured reservoirs with similar matrix quality.

From Nelson's classification, the first three types (Type 1, 2, and 3) of NFR indicate positive and/or negative features of fractures in a reservoir whereas Type 4 describes reservoirs in which fractures impact production and recovery negatively. Based on the Nelson's (2001) classification, the assumptions inherent to the dual-porosity model are only applicable to Type 2 reservoirs where the matrix is stagnant but not the other fracture-matrix systems. Where the matrix is permeable and allows for flow between matrix blocks, the dual-porosity model is extended to a dual-permeability model (Lemonnier and Bourbiaux, 2010a,b). Unlike in dual-porosity model where exchange in NFR is only between matrix and fractures, and flow into the well is via the fractures, dual-permeability model allows additional exchange between matrix blocks as well as flow from the matrix directly into the well.

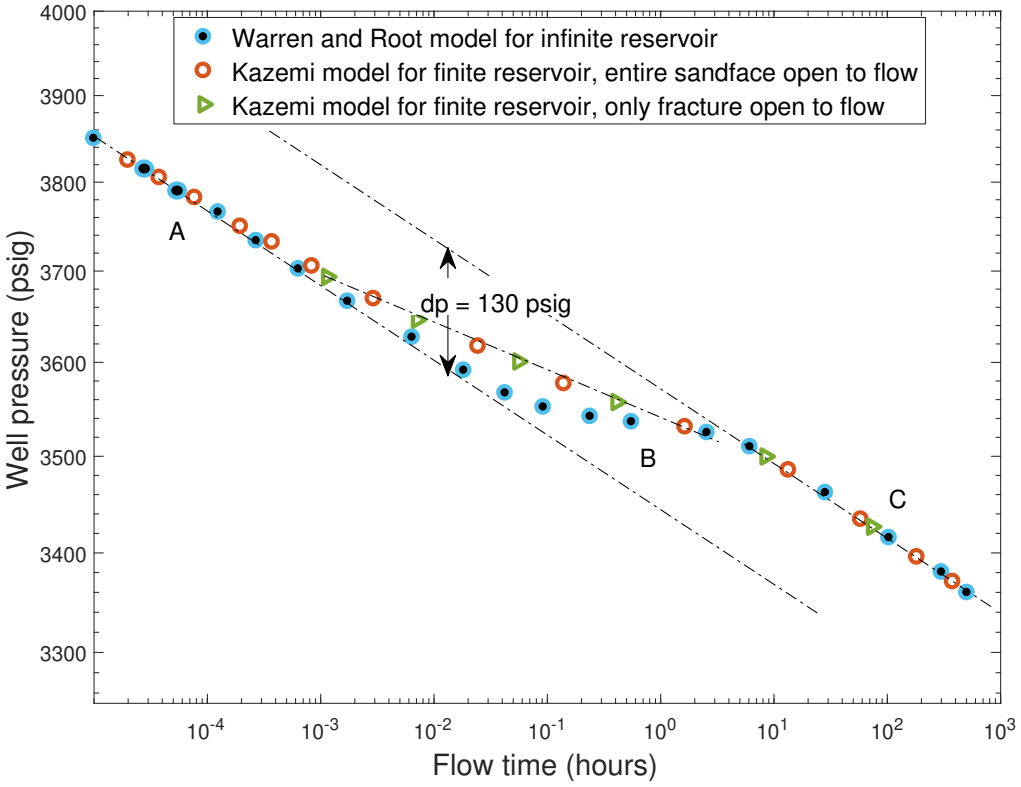

Figure 1.3: Pressure drawdown showing the dual-porosity behaviour according to Warren and Root (1963) and Kazemi et al. (1969). "dp" denotes the vertical separation of the drawdown curves for the fracture and matrix system. A and C denotes two straight lines indicating radial flow and B indicates the transition period between A and C.

Warren and Root (1963) introduced the first technique to identify and interpret a well-test signature from an NFR using the dual-porosity model. Their results, which were reproduced by Kazemi (1969), (see Figure 1.3), show that the pressure drop or build up on a semi-log plot is characterized by two parallel straight

lines, representing the fracture and matrix system, in the reservoir. If transient pressure data are plotted on such a semi-log plot, the first straight line (A in Figure 1.3) indicates the pseudo-radial flow from the fracture system. This is followed by the transition period (B in Figure 1.3) when the depleted fractures are recharged by the matrix until both systems attain equilibrium. Pressure stabilisation in the two systems yields the second straight line indicating radial flow again (C in Figure 1.3).

The development of the pressure derivatives and type-curves (Bourdet and Gringarten, 1980; Bourdet et al., 1983; Gringarten, 1987; Bourdet et al., 1989) provided more efficient ways to interpret dual-porosity behaviours and to determine permeability-thickness (kh), and fracture volumes in NFR. Pressure derivatives on log-log plots also aid the identification of other flow regimes that are not discernible by the semi-log plot (Figure 1.3). Specifically, on a log-log plot (Figure 1.4), the dual-porosity model is depicted by a dual-porosity "dip" (V-shape) - a minimum on the pressure derivative profile (B in Figure 1.4). This V-shape is sandwiched between the first stabilisation (corresponding to a period of flow from the fracture system, see A in Figure 1.4), and second stabilisation (the combined flow from both fracture and matrix system, see C in Figure 1.4).

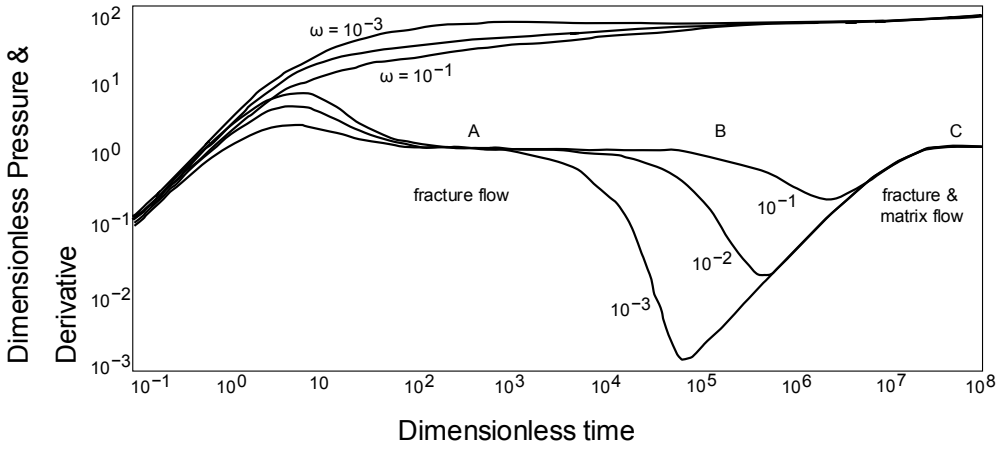

Figure 1.4: A dual-porosity V-shape on a log-log plot showing the influence of the storativity ratio ω on the pressure derivative. The inter-porosity flow coefficient λ is 10^{-7}. After Bourdet (2002).

Warren and Root (1963) proposed that two characteristic parameters control the deviation of the dual-porosity systems from the homogeneous (unfractured) reservoirs. These parameters are the storativity ratio and inter-porosity flow coefficient. The storativity ratio, ω is defined as the ratio of fluids stored in the fracture system to the fluids stored in the total reservoir system (Equation 1.1).

$$\omega = \frac{\phi_f C_f}{\phi_f C_f + \phi_m C_m}, \tag{1.1}$$

where ϕ_f, ϕ_m, C_f, and C_m denote fracture porosity, matrix porosity, fracture compressibility, and matrix compressibility respectively. For dual-porosity systems, ω is typically 0.01 to 0.1. The inter-porosity flow coefficient λ reflects the contrast between the permeability of the matrix and fractures (Figure 1.5) - i.e., it is a measure of the ability of the fluid to flow from the matrix into the fractures and defined as

$$\lambda = \alpha r_w^2 \frac{k_m}{k_f}, \tag{1.2}$$

where r_w, k_m and k_f denote well radius, matrix permeability, and fracture permeability respectively. α is a shape factor that depends on the size and geometry of the matrix. In the original work of Warren and Root (1963) it is defined as $\alpha = 4n(n+2)l^2$, where n is the number of orthogonal (normal) sets of fractures planes (1, 2, or 3) surrounding a matrix block and l is the typical length of the matrix block. For one set of parallel fractures ($n = 1$), two sets of intersecting fractures ($n = 2$) and for a cubic matrix block surrounded by fracture planes ($n = 3$), $\alpha = 12/l^2$, $32/l^2$, and $60/l^2$, respectively. Typical values of λ for dual-porosity systems are 10^{-4} to 10^{-8}.

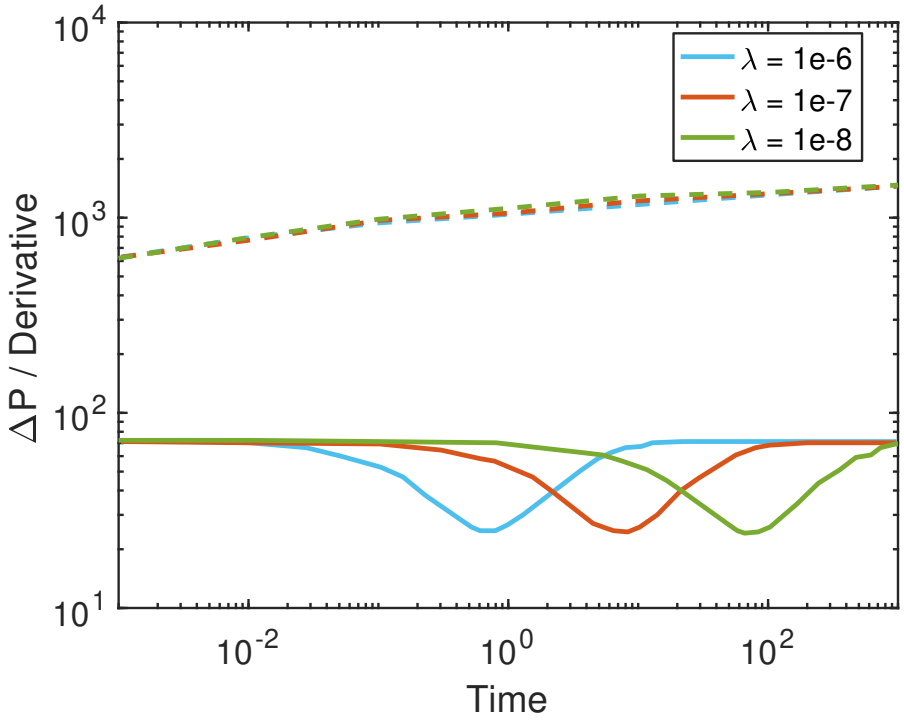

Figure 1.5: A dual-porosity V-shape on a log-log plot showing the influence of the inter-porosity coefficient λ on the pressure derivative. The storativity ratio ω is 0.1. After Houze et al. (2017).

Other authors including Odeh (1965), Kazemi et al. (1969), Streltsova (1976), Mavor and Cinco-Ley (1979) subsequently shared Warren and Root model as-

sumptions. Kazemi (1969), de Swaan O. (1976), Boulton and Streltsova (1977), Najurieta (1980), Cinco-Ley and Samaniego (1982), Serra et al. (1983), and Streltsova (1983) developed alternatives to Warren and Root model that overcome the PSSIF assumption and proposed transient inter-porosity flow (TIF) between fracture and matrix (i.e., the pressure in the matrix blocks can vary locally). This implies that although the response to pressure changes for a fracture intersecting a well is faster in the fracture system compared to the matrix, both systems respond simultaneously at the early time of flow. The TIF assumption argues that PSSIF would be reached only after a considerable period of flow.

Warren and Root's (1963) original model did not consider the effect of wellbore storage and skin. Mavor and Cinco-Ley (1979) added the wellbore effects. Bourdet and Gringarten (1980) extended Mavor and Cinco-Ley's (1979) wellbore storage effect to the TIF model. Moench (1984) and Cinco-Ley et al. (1985) further showed that the early PSSIF regime can be linked to a skin effect (damage at the surface of the blocks) between the matrix and the fractures. Under these restricted inter-porosity flow conditions, the partial plugging of fractures caused by mineralisation, or any form of formation damage result in permeability reduction normal to the fracture face, thus allowing an impaired flow of fluid discharged from the matrix to the fractures. Both PSSIF and TIF flow behaviours have been found in fields and/or have been discussed in the literature (Gringarten, 1984; Wei et al., 1998; Bourdet, 2002; Kuchuk et al., 2015), leading to a debate as to which of these assumptions is more reliable and justified in modelling and interpreting NFR. However, Serra et al. (1983) and Kuchuk and Biryukov (2012) argued that the probability of well-test responses from NFR not yielding the classical dual-porosity V-shape is higher. Therefore, like other evaluation techniques discussed in Chapter 2, well-test interpretation of fractures should be combined with other sources of information to avoid erroneous conclusions (Cinco-Ley, 1996).

There are further limitations to the dual-porosity model which have been addressed in subsequent studies. Several authors, including Wei et al. (1998), Corbett et al. (2012), Morton et al. (2012), Morton et al. (2013), and Morton et al. (2015), Nogueira et al. (2013), Agada et al. (2014), Kuchuk and Biryukov (2014, 2015), and Morton et al. (2015) have demonstrated that the pressure behaviour in an NFR can be notably different from the theoretical dual-porosity behaviour predicted for an NFR with well-connected fracture networks. These studies further suggest that neither form, PSSIF or TIF, of the dual-porosity model assumptions may be adequate to interpret well-test data from certain NFR, e.g. discretely fractured reservoirs. On the other hand, simulation of discretely fractured reservoirs with a single porosity model would not be sufficient to match the well-test data nor honour the field geological model (Morton et al., 2012; Nogueira et al.,

2013). The dual-porosity model assumes that the matrix acts as a source that recharges the continuous fracture network, which in turn flows in to the well (Figure 1.6). In moderately and/or discretely fractured reservoirs, the matrix interaction with the well is significant because the fracture networks are not well-connected and the matrix contributes to flow (Morton et al., 2012). These reservoirs relate to Type 3 of Nelson's classification of NFR. In this case, the pressure responses observed in well-tests do not exhibit the classical dual-porosity behaviour. Hence, the use of the dual-porosity model may not be appropriate for identification and interpretation of all NFR, particularly for moderately and/or discretely fractured reservoirs. Yet, the fractures present in these reservoirs can be a first-order control on reservoir performance.

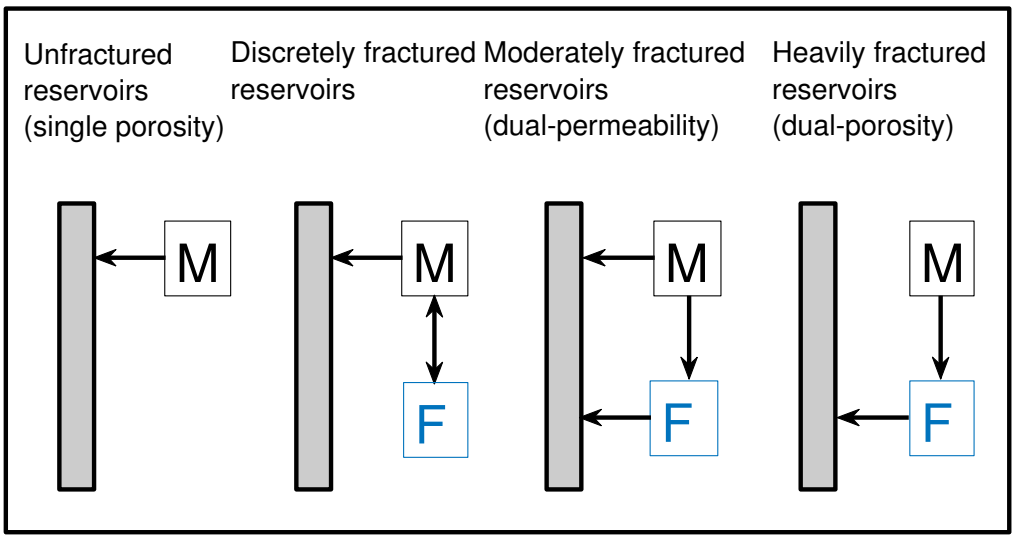

Figure 1.6: Well-test models for naturally fractured reservoirs. After Morton et al. (2012).

This observation raises the important question as to what properties of the fracture network cause the dual-porosity signal to be absent in some NFR and to be present in others. Since the location, orientation, and connectivity of fractures are very difficult to quantify directly and unambiguously in the reservoir, linking known properties of the fracture network to the dynamic response during a well-test remains elusive and is not captured by standard well-testing analysis workflows. One key motivation for this research hence is to provide answers to the important question as to why the so-called characteristic well-test dual-porosity signature (i.e. the V-shape) appears in some pressure transient data from NFR but is absent in others.

As previously stated, there is a clear distinction when assuming PSSIF and TIF in NFR. The original dual-model assumes PSSIF and shows the classical V-shape if ω and λ are within a typical range of 0.1 to 0.01 and 10^{-4} to 10^{-8}, respectively. On the other hand, TIF implies that the fluid exchange between fractures and matrix is always transient even if the permeability contrast be-

tween fractures and matrix is small (Cinco-Ley and Samaniego, 1977; Mavor and Cinco-Ley, 1979; Kuchuk and Biryukov, 2012). For this reason, a number of field examples do not show a V-shape (Bourdet and Gringarten, 1980; Nogueira et al., 2013; Kuchuk and Biryukov, 2014, 2015) . Other authors (Streltsova, 1976; Gringarten, 1984) stated that PSSIF can only occur after a long time of the well testing and should be treated as a long-time approximation of TIF. The debate is then which of these exchange mechanisms is more realistic since the behaviours corresponding to both PSSIF and TIF are found in the field (Gringarten, 1984). Several studies have been undertaken to explain why NFR that show TIF during production also yield dual-porosity V-shape (a classic feature of PSSIF) at early time of well testing. The factors listed below highlight the most common explanations provided in the literature to address observations why an NFR where TIF is assumed to control production shows the classic dual-porosity V-shape but other NFR do not. This is in addition to pressure behaviours observed in moderately and/or discretely fractured reservoirs and fields examples where the classic dual-porosity response is not observed on pressure data.

a. *Inter-porosity skin*. This factor assumes that inter-porosity flow in NFR always occurs under TIF conditions but pressure behaviour can exhibit PSSIF due to inter-porosity skin, i.e. an impediment to flow between matrix and fractures (Cinco-Ley and Samaniego, 1977; Mavor and Cinco-Ley, 1979; Cinco-Ley and Samaniego-V., 1981; Gringarten, 1984, 1987; Bourdet, 2002; Valdes-perez et al., 2011; Kuchuk and Biryukov, 2015). The skin restricts communication between and/or within the matrix-fracture systems and could result from damage caused by mineral deposits within fractures or along fracture faces, well completion, drilling mud, etc. The inter-porosity skin factor led to categorising the pressure behaviours into the restricted or pseudo-steady state and unrestricted or transient inter-porosity flow. The former produce the classical dual-porosity response but the latter do not.

b. *Wellbore storage* (*WBS*). *WBS* often masks the pressure transient at early time. When combined with skin effect, this can exhibit pressure behaviour similar to the classical dual-porosity response (Cinco-Ley and Samaniego, 1977; Mavor and Cinco-Ley, 1979; Kuchuk and Biryukov, 2015).

c. The fracture pseudo-radial flow at early time can occur so quickly that the pressure response corresponding to the first dual-porosity straight line is absent in real field-tests. At early time ($t \rightarrow 0$), the classic dual-porosity response occurs due to the reservoir behaving as if it contains only fractures (ω and $\lambda \rightarrow 0$) (Serra et al. 1983). This period occurs often too early during a well-test and hence cannot be recorded for practical purposes (Odeh, 1965; Kazemi, 1969). Thus, the fracture pseudo-radial flow at early time is only

a mathematical characterisation rather than a measurable behaviour (Najurieta, 1980). In addition, the early time pressure response is obscured if WBS is present (Cinco-Ley et al., 1976; Bourdet and Gringarten, 1980). Thus, the dual-porosity response would likely not be observed in practice.

d. The radial flow corresponding to fracture-matrix exchange at pressure equilibrium may occur so late that the pressure response corresponding to the second dual-porosity straight line is therefore absent in practice. Others (Cinco-Ley et al., 1976; Serra et al., 1983) have argued that second line may not be observed in the field because the test does not last long enough. At this time ($t \rightarrow \infty$), the reservoir behaves like an homogenous system with a constant diffusivity (de Swaan O., 1976; Najurieta, 1980). Gringarten (1984) suggested that when the duration is short, only the first fracture pseudo-radial flow behaviour would appear. If the test stops during the transition time, the pressure profile would resemble that of an homogenous reservoir with a boundary.

e. *Significant matrix permeability*. A central assumption in the DP model is negligible matrix permeability, i.e. fluid flow between matrix blocks is absent (Warren and Root, 1963). The pressure behaviour in a NFR will not show two parallel straight lines before the early flow in fracture system can be clearly identified as an equivalent homogenous medium if the matrix permeability is large enough to enable flow between matrix blocks (Kuchuk and Biryukov, 2012). This factor is also important in moderately and discretely fractured reservoirs.

f. *Other factors*. A number of studies (Wei et al., 1998; Kuchuk et al., 2014; Morton et al., 2015) stated that Warren and Root's (1963) model is oversimplified. As such, the classic dual-porosity behaviour is absent when realistic flow exchange between fractures and matrix is modelled using transient well tests. In addition, since inter-porosity flow between fractures and matrix in NFR is always transient, a dual-porosity model with PSSIF would be inadequate to describe the behaviour of fractured reservoirs (Wei et al., 1998). Furthermore, the complexity of fractured reservoirs defies one complete and satisfactory mathematical model (Odeh, 1965; Gringarten, 1987). Thus, pressure behaviour corresponding to the dual-porosity model is only one possible well-test interpretation but does not necessarily apply to all NFR. Kuchuk and Biryukov (2014) and Kuchuk et al. (2014) suggest that the Warren and Root original model did not contain any fracture, but rather an equivalent (fictitious) homogenous medium. Therefore, the pressure behaviours corresponding to such models represent neither a well that intersects fractures nor a well that is located in the matrix.

The above overview on the applicability and limitations of the dual-porosity model provides the background and motivation for the development of this PhD research. Of particular interest in this PhD thesis is a systematic study to answer the question why the classical well-test dual-porosity signature can be absent in some NFR with well-developed fracture networks but is present in others, including reservoirs with discrete fracture networks. Some of the limitations of the dual-porosity model highlighted above will be demonstrated in different sections of the thesis; this enables us to develop new insights on the reservoirs features that cause the dual-porosity response in NFR. Other contributions of this thesis relate to the interpretations of some unconventional well-test responses that will improve our general understanding as to which geological features in an NFR can be detected from well-tests. This thesis further describes how the research findings are applied to interpret well-test data in a newly discovered, fractured carbonate reservoir.

1.3 OUTLINE OF THE THESIS

1.3.1 *Aims and Objectives*

The aim of this thesis is to use geological well-testing to, first, explore when and why the conventional assumptions and the characteristic flow behaviour inherent to the dual-porosity model break down when interpreting well-test data from NFR. Secondly, we aim to provide insights into the geological features in a reservoir that cause the classic dual-porosity response and control other unconventional signatures in well-tests data from NFR. The following specific objectives are defined for this research project:

i. To apply a geoengineering workflow with Discrete Fracture Matrix (DFM) modelling techniques and unstructured-grid reservoir simulations for integrated well-testing analysis of NFR.

ii. To quantify limitations of existing well-test analysis techniques for NFR.

iii. To systematically develop alternative interpretation methods and analyse which geological features of a NFR can be detected from well-tests.

iv. To apply the research findings to analyse the data of a real field production test.

1.3.2 *Scope of Investigation*

The scope of our investigation relates specificially to vertically oriented natural fractures of the Type 2 and 3 reservoirs of Nelson's (2001) classification. However, some of our observations and findings may also apply to other types of NFR in Nelson's classification. In addition, modelling of hydraulic fractures, faults and vugs is out of the scope of this study.

1.3.3 *Structure of the Thesis*

The thesis is divided into introduction, literature review, methodology, numerical simulations and application of geoengineering workflow and research findings to real field data. Synopses of the individual chapters are presented below:

Chapter 1 - the current chapter provides the thesis overview. It highlights the importance of the NFR, defines the challenges in characterising and developing this type of reservoir, introduces the classical methods used in simulating and interpreting dynamic pressure behaviour of NFR, and discusses their limitations. This chapter hence establishes how the knowledge generated in this study helps to improve the understanding of fluid flow behaviour in NFR to enable better interpretations of well-test data from NFR.

Chapter 2 - provides a comprehensive review of previous studies that focus on the characterisation of NFR. It highlights the existing classifications of NFR from a geological and an engineering point of view, and describes both positive and negative impacts of fractures on reservoir performance and recovery. The effects of the fractures underscore the need for thorough characterisation of NFR prior to field development. To this end, a summary of direct and indirection sources of information for reservoir characterisation is presented.

Chapter 3 - describes the methodology adopted for the research investigations, including details on how a geoengineering workflow with explicitly represented fractures simulated using unstructured grids is applied. It also states the equations that govern fluid flow in a fractured reservoir. The basic well-test analysis techniques including the use of pressure derivative curves for identification of flow regimes for a range of reservoir conditions are described. The chapter also provides background information to the realistic outcrop fracture data used in the study.

Chapter 4 - explores when and why dual-porosity well-test responses are present in some NFR and absent in others. It also provides insights into the geological features present in a reservoir that cause the dual-porosity behaviour observed on pressure derivatives.

Chapter 5 - presents results for different fracture properties including variation in fracture geometry, fracture conductivity, averaging of fracture conductivity, and the effect of well location in a fracture network.

Chapter 6 - this chapter describes how the geoengineering workflow used in this study and the resulting insights can be applied to improve the interpretation of a well-test in a recently discovered naturally fractured reservoir. The chapter further describes how the pressure data from the reservoir was used to develop deterministic geological concepts that aid the calibration of the reservoir model. Overall, the chapter presents novel reference solution for interpreting NFR with dual-porosity or triple-porosity pressure signatures.

Chapter 7 - summarises the contribution to knowledge of this research and provides conclusions on the key outcomes of the thesis. This is followed by recommendations for future work in this area of research.

2

NATURALLY FRACTURED RESERVOIRS

In this literature review, the concept of naturally occurring fractures in geological formations will first be introduced; then an overview of the existing classifications for naturally fractured reservoirs (NFR) from a geological and an engineering point of view will be provided. The main characteristics of the reservoir types and their implications on the reservoir behaviour will also be highlighted. Next, the effects of natural fractures on reservoir performance from appraisal to production to ultimate recovery will be summarised. The review section will close with a brief description of the most common direct and indirect methods used in characterisation of NFR, the fracture attributes that each of the methods provide, and the limitations of the characterisation techniques if used in isolation.

2.1 BACKGROUND

In the majority of sedimentary and nearly all basement fractured reservoirs, hydrocarbon production and recovery are impacted by the presence of natural fractures. Hence, the petroleum industry has adopted the approach that "all reservoirs should be considered fractured until proven otherwise" (Narr et al., 2006). Characterising reservoirs without accounting for the effect of fractures would not result in a suitable reservoir management scheme and may lead to costly remedial actions at later time of the field development. Therefore, the impact of fractures should be considered early during field development planning in order to minimise the impact on production and thus improve recovery.

A simple definition of a NFR is a reservoir that contains fractures that occur from natural geologic processes as opposed to those that result from man-made, stress differences introduced to the rock as part of a reservoir stimulation or drilling operation (Aguilera, 1998). Others define NFR in terms of the effect of the fractures on recovery, that is as a reservoir in which the existing natural fractures have or are predicted to have a significant impact on reserves and/or recovery (Narr et al., 2006). The effects of natural fractures on a reservoir can be positive, neutral, or negative (Pirson, 1953; Huskey and Crawford, 1967; Dean and Lo, 1988; Berkowitz, 2002; Gilman, 2003; Narr et al., 2006; Bourbiaux, 2010;

Spence et al., 2014). Where these natural fractures do not impact fluid flow or if their effect is negligible, the fractured formations may not be treated as NFR (Aguilera, 1998; Nelson, 2001).

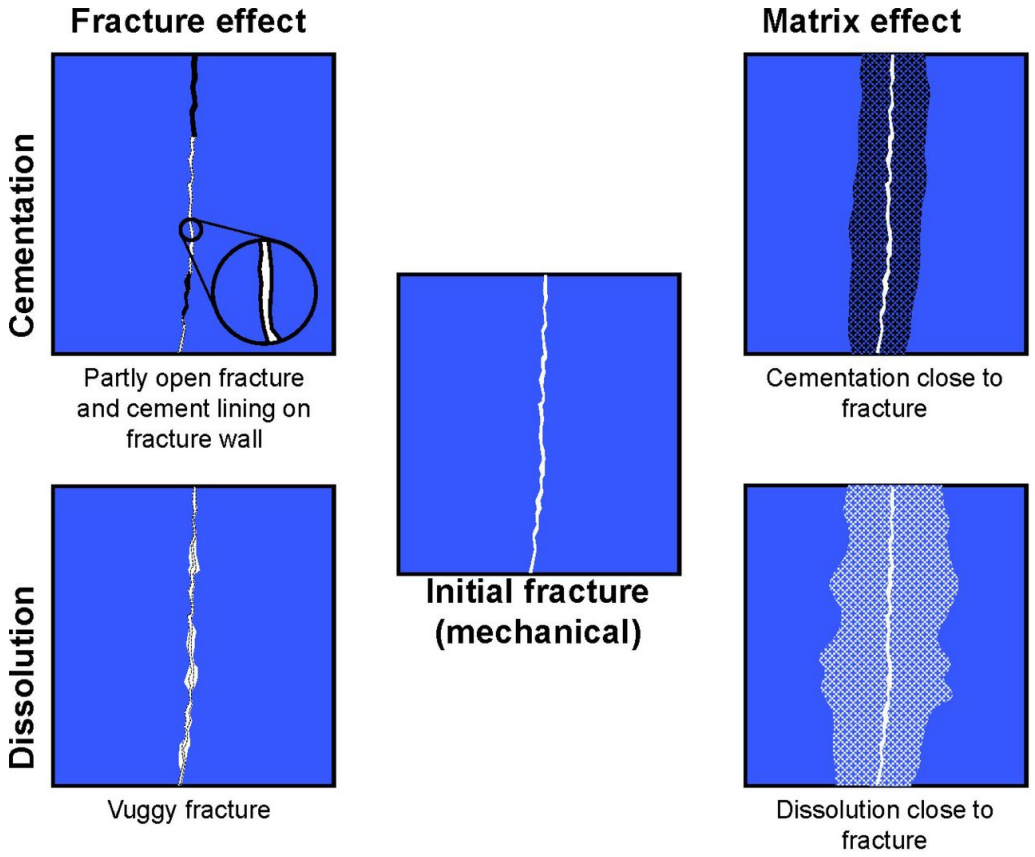

Figure 2.1: Diagenetic effects on fracture properties may be destructive by cementation or constructive by dissolution. The matrix porosity and permeability may also decrease by cementation or increase by dissolution. After Wennberg et al. (2016).

A natural fracture, also simply referred to as "fracture" in this thesis, unless otherwise qualified, is defined as a macroscopic planar discontinuity in a rock (Committee on Fracture Characterization and Fluid Flow, 1996; Nelson, 2001; Tiab and Donaldson, 2016) formed due to deformational or physical diagenetic stresses that exceed the rupture strength of the rock (Stearns and Friedman, 1969). Diagenesis comprises all physical, chemical and/or biological processes that convert deposited sediments into sedimentary rock (Ali et al., 2010; Haile et al., 2017). Diagenetic processes include burial compaction and cementation, pressure solution, and dissolution, mineral precipitation, dolomitisation etc. The chemical changes (e.g. dissolution, precipitation of calcites etc.) that occur during diagenesis are more prevalent in carbonates reservoirs. Since fractures can be formed in a reservoir prior to, during, and/or after hydrocarbon accumulation, these processes continue to modify the properties of the fractures as well as the matrix with time resulting in variable properties within and between fractures (Figure 2.1). These changes can enhance, modify, or destroy reservoir porosity

and permeability, which will ultimately determine the quality and commercial viability of a reservoir (Ali et al., 2010; Gale et al., 2014; Wennberg et al., 2016).

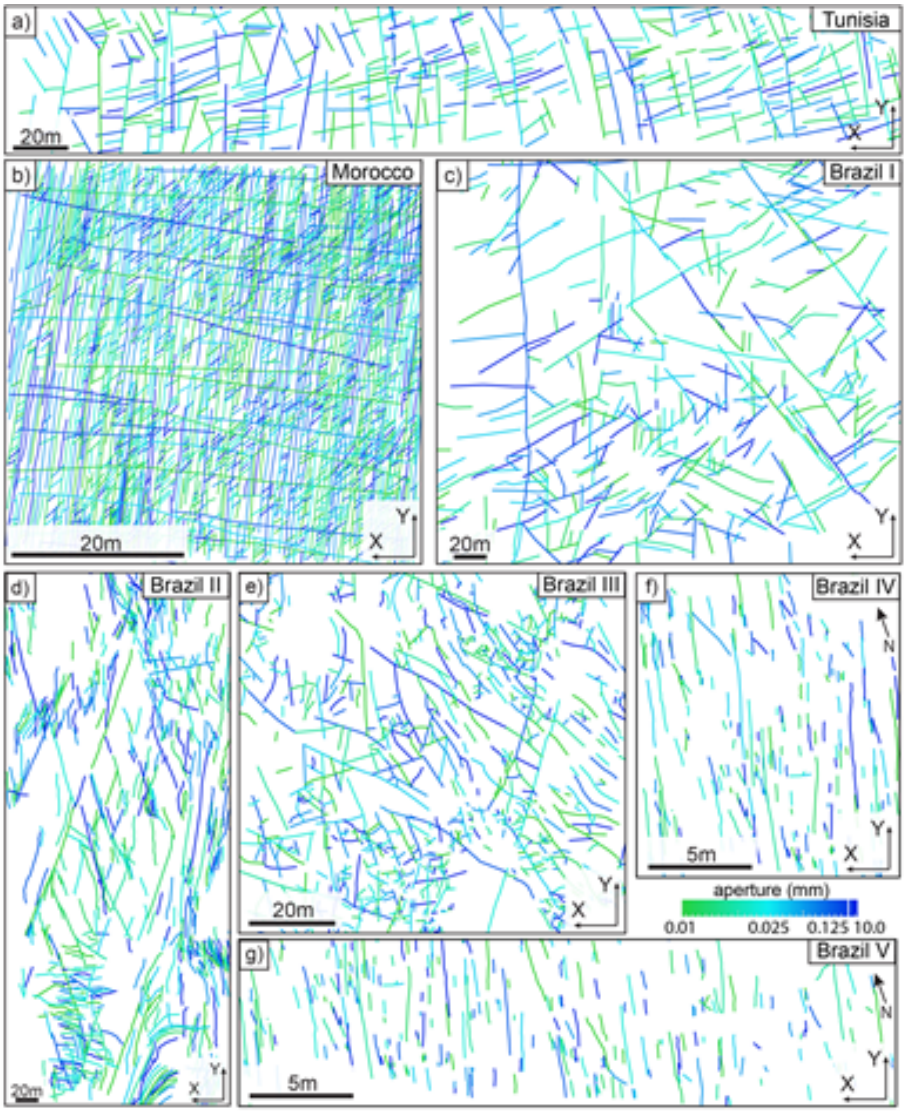

Figure 2.2: Map-view of multiscale fracture geometry and aperture distributions mapped in different outcrops. Taken from Bisdom et al. (2016).

Fractures are multiscale in nature and their lengths can scale from micrometres (micro-fissures) observed in cores to several kilometres (regional fractures/-faults) in basins and are hence detectable on seismic data (Hardebol et al., 2015; Bisdom et al., 2016; Tiab and Donaldson, 2016; Bisdom et al., 2017a). The multiscale nature of fractures is apparent in outcrops (Figure 2.2).

Fractures can be open, partially closed (mineralised) or fully closed. This results in different effects on fluid flow in a reservoir performance (e.g., Cinco-Ley and Samaniego, 1977; Gonzalez-Chavez and Cinco-Ley, 2006; Valdes-perez et al., 2011; Egya et al., 2018c). Closed fractures create barriers to flow and reservoir compartments. These permeability barriers could lead to poor or uneconomical recovery. Open fractures might have a positive effect on production by providing flow path and pressure support to the producer but a negative effect on water

and gas flow due to conning and early breakthrough. During production (and pressure depletion) in over-pressured reservoirs, open fractures may close due to an increase in the effective normal stress on the fracture due to the decrease in reservoir pressure (Aguilera, 2003; Friedel, 2004; Makel, 2007). Mineral deposits in partially closed fractures may act as proppants and hold fractures open during depletion. This preserves the required conduit for production of fluid from the reservoir to the wellbore and result in better ultimate recovery (Aguilera, 1998; Makel, 2007).

2.2 CLASSIFICATIONS OF NATURAL FRACTURES

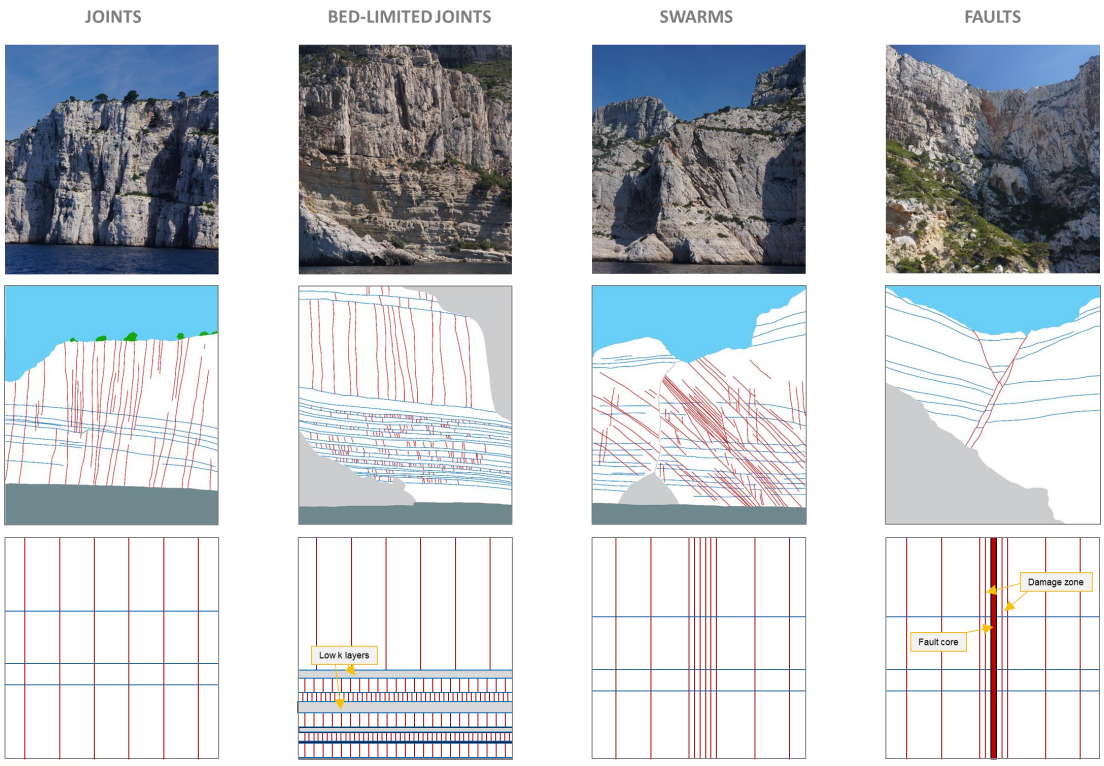

Figure 2.3: Top: Fracture styles observed in a Lower Cretaceous (Barremian) carbonate reservoir outcrop analogue near Cap Câble close to Cassis, France. Middle: Sketch of the fractures observed on the outcrop. Bottom: The fractures representation in reservoir model. Taken from Bentley et al. (2017).

Different geological and engineering classifications of NFR exist in the literature (Stearns and Friedman, 1969; Aguilera, 1998, 1999; Nelson, 2001; Bratton et al., 2006; Tiab and Donaldson, 2016). Geological classifications are based on fracture patterns that are observed in laboratory experiments, outcrops and the subsurface. These classifications enable us to understand and predict the characteristic behaviours of fractures during production because there is an established relationship between fractures flow properties and their origin (Committee on Fracture Characterization and Fluid Flow, 1996). Knowledge of fractures types

also improves the quality of static and dynamic reservoir modelling (Bratton et al., 2006). Figure 2.3 shows different fractures styles observed in an outcrop analogue for a Lower Cretaceous carbonate reservoir, and how these fractures can be conceptualised and modelled. The engineering classifications are based on the overall contribution of fractures to the reservoir's storage (porosity) and flow (permeability) capacity.

2.2.1 *Geological Classifications*

Stearns and Friedman (1969) and Nelson (2001) classified NFR on the basis of stress/strain conditions in controlled laboratory experiments and fractures observed in outcrops. These are shear, extension and tension fractures (Table 2.1 and Figure 2.4) and are summarised briefly as follows:

Shear fractures. These fractures show displacement parallel to the fracture plane. In the laboratory, shear fractures form at an acute angle to the maximum compressive principal stress direction ($\sigma 1$) and at an obtuse angle to the minimum compressive stress direction ($\sigma 3$). They form when all three principal stresses are compressive.

Extension fractures. These fractures also form when all three principal stresses are compressive and can occur together with shear fractures. They show displacement perpendicular to and away from the fracture plane (parallel to $\sigma 1$ and $\sigma 2$ and perpendicular to $\sigma 3$). They are formed perpendicular to the minimum stress direction.

Tension fractures. They are sometimes described interchangeably with extension fractures. They also show displacement perpendicular to and away from the fracture plane and experience relatively low differential stresses. However, at least one of the principal stresses ($\sigma 3$) is tensile.

Experimental Fracture Classification	**Naturally Occurring Fracture Classification**
1. Shear fractures 2. Extension fractures 3. Tensile fractures	1. Tectonic fractures (due to surface forces) 2. Regional fractures (due to surface forces or body forces) 3. Contractional fractures (due to body forces) 4. Surface-related fractures (due to body forces)

Table 2.1: Experimental and natural fracture classification (Nelson, 2001).

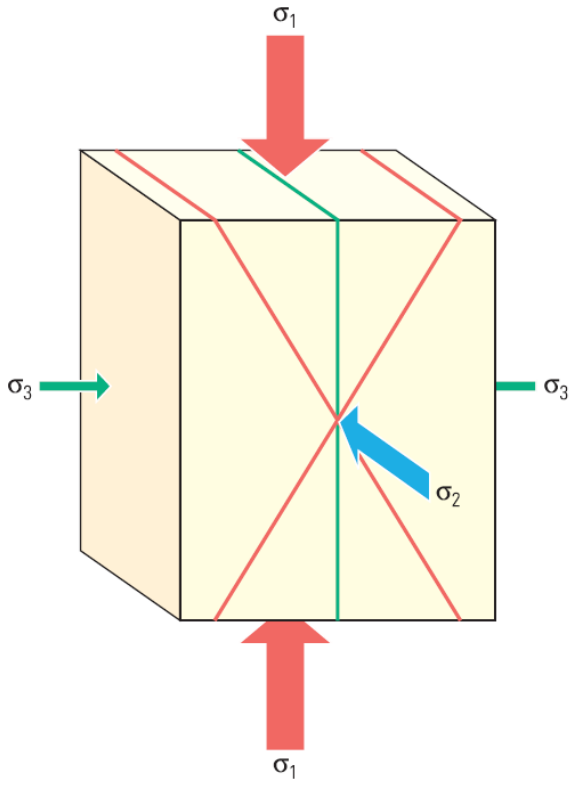

Figure 2.4: Creation of fractures relative to the direction of the three principal stresses. $\sigma 1$, $\sigma 2$ and $\sigma 3$ denote the maximum compressive principal stress, the intermediate stress, and the minimum compressive principal stress, respectively. Tension fractures (green) form parallel to $\sigma 1$ and $\sigma 2$. The acute angle that forms between two shear fractures (red) is called the conjugate angle. The angle that forms between the shear fracture and $\sigma 1$ is called the dihedral angle. An obtuse angle forms between the shear fracture and $\sigma 3$, while the shear fractures are parallel to $\sigma 2$. Taken from Bratton et al. (2006).

The fractures observed in laboratory experiments (Table 2.1) have correlations with naturally occurring fractures observed in outcrops (Nelson, 2001; Bratton et al., 2006). These natural fractures have been classified on the basis of their geological origin, i.e. the paleo stress conditions at the time of their formation, as tectonic, regional, and diagenetic fractures (Stearns and Friedman, 1969; Aguilera, 1998; Nelson, 2001; Tiab and Donaldson, 2016), as discussed in the following:

Tectonic fractures. The origin of tectonic fractures, likewise their orientation, distribution, and morphology, are related to local tectonic events. The resulting fracture networks are spatially associated with faults and folds. The fault-related fractures are mostly observed in outcrops as shear fractures that formed parallel to faults or at an acute angle to the fault plane. The intensity of fault-related fractures is a function of formation's lithology, distance from the fault plane, magnitude of fault displacement, total strain in the rock mass, and depth of burial. Others fractures associated with both faulting and folding processes can be shear fractures as well as extension fractures bisecting the acute angle

between two fault shear directions. Tectonic fractures are the most important fracture types with respect to hydrocarbon production (Aguilera, 1998).

Regional fractures. The origin of the regional fractures is related to large scale plate tectonics (faulting and/or folding). These fractures are formed over a large area of the earth's crust. They occur perpendicular to main bedding surfaces and are usually long fractures with relatively little change in orientation over their lengths (orientation is constant within 10-15° over 100 miles). Regional fractures seem unrelated to local structures, tend to develop orthogonal patterns, and have relatively large spacing compared to tectonic fractures. Regional fractures tend to be conducive to fluid flow because there is no offset and damage to the host rock along the fracture plane. Where regional fractures are superimposed on tectonic fractures, production is enhanced (Aguilera, 1998).

Diagenetic fractures. These fractures are also referred to as contractional fractures. They form due to diagenetic changes in the rock and result from bulk volume reduction mechanisms within the rock and not from external forces. The most common examples are syneresis fractures (e.g. chickenwire texture), desiccation cracks (e.g. shrinkage cracks), thermal contraction fractures, and fractures caused by mineral phase changes. Syneresis fractures are formed by chemical processes that cause dewatering and associated volume reduction. Mud cracks are the most common desiccation fractures and they result from shrinkage upon loss of water in subaerial drying. Whereas desiccation fractures are tensile fractures, syneresis fractures can be either tensile or extension fractures and have been observed in both carbonates and clastic reservoirs (Tiab and Donaldson, 2016). Of these, syneresis fractures, and fractures caused by mineral phase change in carbonates have the greatest importance in oil and gas production (Bratton et al., 2006). Furthermore, mineral changes in rocks, especially in carbonates and clay rich sedimentary rocks, may also result in the formation of fractures and other structures that influence reservoir performance of NFR. Examples include the chemical change from calcite to dolomite result in changes in bulk volume, which can lead to complex fracture patterns (Tiab and Donaldson, 2016).

Figure 2.5 illustrates the modes of fracture formation. Mode I tension fractures correspond to joints while Mode II and III shear fractures correspond to faults. Anti-mode fractures are closing Mode I fractures such as pressure solution surfaces or stylolites. Faults form oblique to the bedding and show visible displacement along the planar discontinuity whereas, joints and fractures form perpendicular to bedding and have no visible displacement. Since fractures do not result in displacement of bedding, they cannot be directly observed on seismic data. However, they can be detected in core samples, well-logs, and borehole

images. In addition, fractures can be either layer-bound (i.e. stop at bedding surfaces) or non-layer-bound (i.e. cut through bedding). Layer-bound fractures can occur at regular spacing and develop into a well-organised connected fracture network. Nonlayer-bound fractures are spatially clustered as discrete fractures (Bratton et al., 2006; Rogers et al., 2007; Hooker et al., 2013).

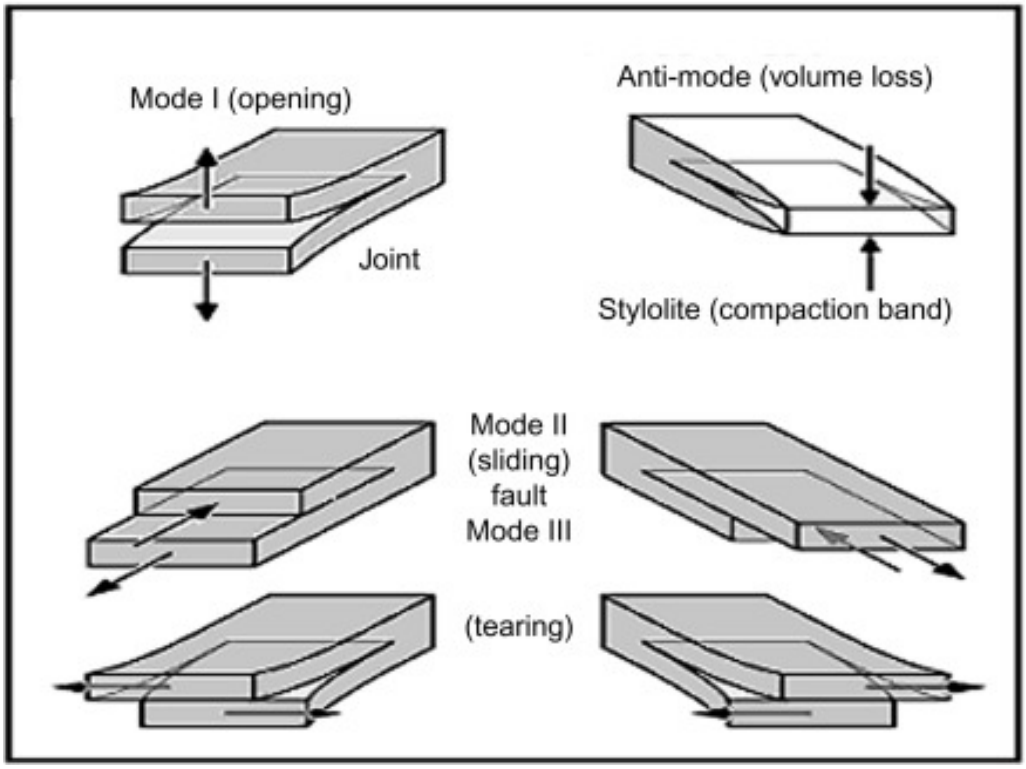

Figure 2.5: Modes of fracture formation. Taken from Tiab and Donaldson (2016).

Furthermore, NFR can be geologically classified, on the basis of their porosity systems, into intercrystalline-intergranular, fracture-matrix, and vugular-solution (Aguilera, 1998; Tiab and Donaldson, 2016). The classification describes the geometry and pore size typical to carbonate reservoirs. Using these descriptions, (Aguilera, 1999) related the performance of NFR types to their petrophysical properties (e.g. immobile water saturation and capillary pressure curves). Carbonate rocks can dissolve in fresh water and other fluids to form caves or vugs. The resulting porosity is termed karst and is important in many fractured carbonate reservoirs (Bratton et al., 2006). Pressure solution, a dissolution process that reduces pore space under pressure during diagenesis have the tendency to form stylolites with uneven surfaces of insoluble residue. Stylolites can result in local permeability reduction or enhance permeability by facilitating subsequent dissolution.

Other classifications (Committee on Fracture Characterization and Fluid Flow, 1996) simply group fractures into dilating fractures/joints, shearing fractures/-faults, and closing fractures/pressure solution surfaces. Closing fractures relate to diagenetic alterations in which fractures faces are welded together by pressure

solution and mineralisation. It is apparently challenging to prescribe one simple geological classification to describe natural fractures comprehensively, appeal to multidisciplinary aspects of oil industry and yet be technically unambiguous. However, this classification scheme (Committee on Fracture Characterization and Fluid Flow, 1996) is comprehensive yet technically precise. It distinguishes fractures in terms of the mode of formation, common to above-mentioned classifications, yet with terms that are common to many disciplines of the petroleum industry. In addition, the classification also indicates the current status of the fractures.

2.2.2 *Engineering Classifications*

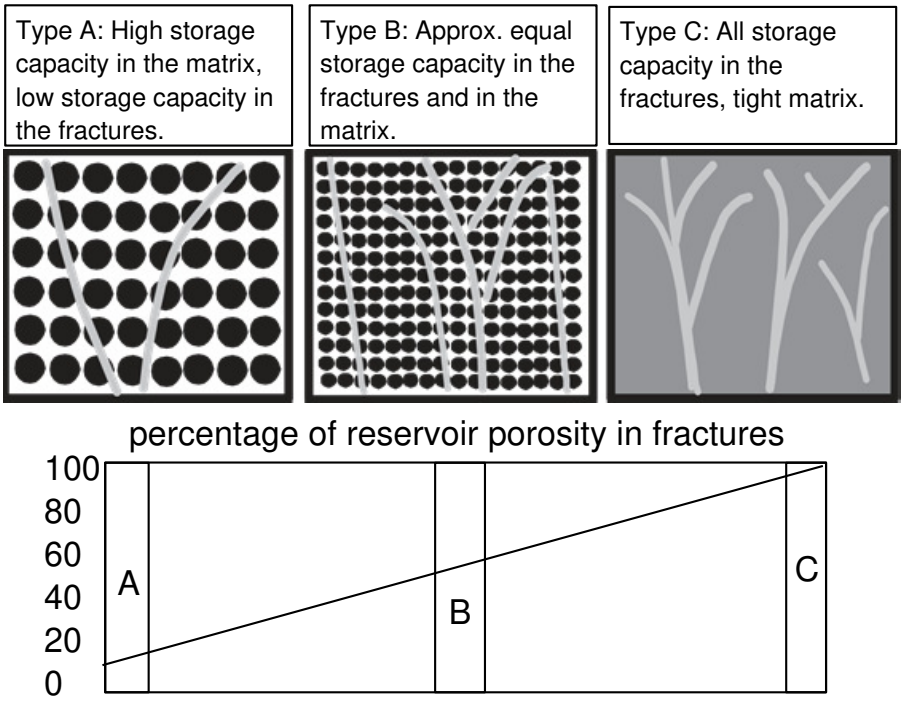

Figure 2.6: NFR classification by porosity distribution. Percentage of fracture porosity is given by $\frac{\phi_f}{\phi_f+\phi_m}$ X 100. After Aguilera (1983).

Aguilera (1983) and Nelson (2001) classified NFR on the basis of permeability and porosity and the overall contribution of fractures to the reservoir's storage (porosity), and flow capacity (permeability). Nelson's classification is described in Chapter 1. Aguilera's classification (Figure 2.6) divides NFR into Type A, B and C based on the percentage of reservoir storage that is contained in fractures. Type A has low storage capacity in the fractures and high storage capacity in the matrix. Type B has approximately equal storage capacity in the fractures and in the matrix. All storage capacity in Type C is in the fractures surrounded by tight matrix.

In addition to the engineering classifications of Aguilera (1983) and Nelson (2001) which consider porosity and permeability, Kuchuk and Biryukov (2014, 2015) developed a classification of NFR based on pressure transient behaviours. The basis of Kuchuk and Biryukov's classification is similar to Morton et al. (2012) NFR types described in Chapter 1. They suggest the following types of NFR:

1. Continuously fractured (dual-porosity) reservoirs;
2. Discretely fractured reservoirs;
3. Compartmentalised faulted reservoirs;
4. Unconventional fractured basement reservoirs.

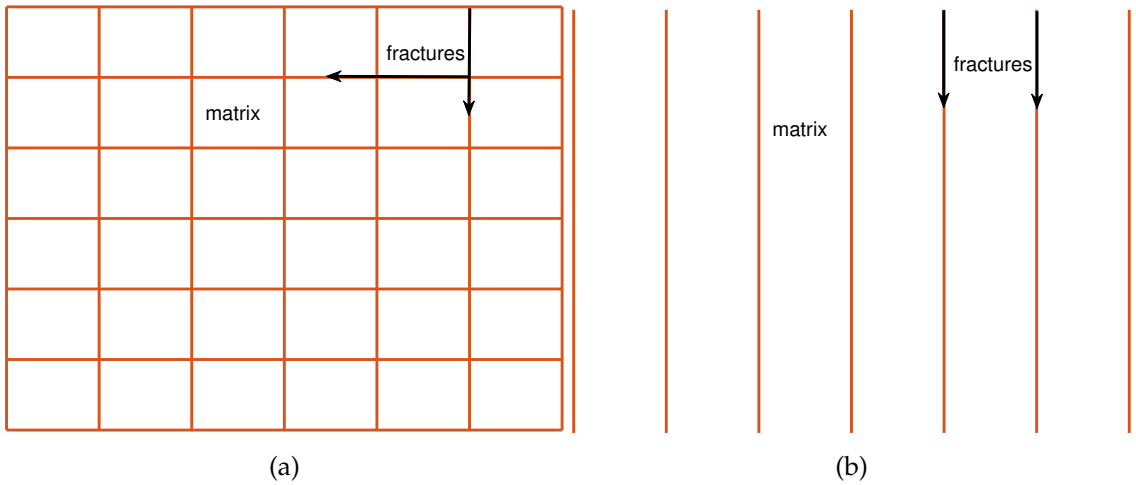

Figure 2.7: Idealised connected fracture network (a) and disconnected fracture network (b).

Continuously fractured reservoirs, also referred to as dual-porosity and dual-permeability reservoirs, contain connected fracture networks (Figure 2.7a) that communicate directly with each other and provide the overall reservoir conductivity/permeability. The matrix provides the overall reservoir storage capacity, but it is also permeable enough to allow fluid flow from the matrix into the fractures. The fracture network could be orthogonal and non-orthogonal. Discretely fractured reservoirs, which are also called disconnected fracture networks (Figure 2.7b), contain only a limited number of fractures that communicate hydraulically with each other. Reservoirs with vertically stacked fractured and unfractured layers also belong to this category. In addition, continuously fractured reservoirs that are partially filled with minerals (i.e. the hydraulic communication between individual fractures is impeded) can also be regarded as discretely fractured reservoirs. In this type of reservoir, the contribution of matrix permeability could be high or low. The fracture network in this category tends to be

non-orthogonal rather than orthogonal in nature. In compartmentalised faulted reservoirs, the matrix provides both the storage and flow capacity. Fractures are non-conductive and act as baffles or barriers to flow. In unconventional fractured basement reservoirs, the matrix does not contribute to flow capacity and/or porosity.

Even though Nelson (2001), Aguilera (1995, 2010), Kuchuk and Biryukov (2014, 2015) classified NFR using difference criteria such as porosity, permeability and pressure transients, their classification can be correlated based on the dominating attributes of fractures for each fracture categories. Table 2.2 attempts to correlate these classification schemes based on the equivalent fracture attributes.

Nelson (2001)	**Aguilera (1995, 2010)**	**Kuchuk and Biryukov (2014, 2015)**
Type 1	Type C	Unconventional fractured basement
Type 2	Type B	Continuously fractured
Type 3	Type A	Discretely fractured
Type 4	-	Compartmentalised

Table 2.2: Correlation of NFR classification schemes based on equivalent fracture attributes.

Aguilera (1998, 2003) stated that "rules of thumb and naturally fractured reservoirs do not mix well. What appears to work in one might fail miserably in the next. Consequently, each naturally fractured reservoir exploration play must be an individual research project". Nonetheless, the classification of natural fractured systems into geological and engineering terms allows for a preview of what is to be expected from a given field with characteristic features of a reservoir type. Once classified, the impact of fractures in NFR can be evaluated in specific terms using their predictor (Table 2.3). This way, the degree to which a fracture attribute is expected to impact the reservoir performance will determine the depth of investigation for such effect (Bratton et al., 2006). Because different fractures conduct fluids differently and not all NFR are the same, knowledge of fracture types and classifications enhances our ability to simulate fluid flow through them. This in turn allows us to better characterise and develop NFR. The next section of this literature review highlights the various effects of fractures during the production life of a reservoir.

POSITIVE ATTRIBUTES	POTENTIAL NEGATIVE ATTRIBUTES
Type 1: fractures provide essential porosity and permeability	
• Drainage areas per well are large • Few wells needed in development (in-fill for rate acceleration only) • Good correlation between well rates and well reservoirs • Best wells are often early • Generally high Initial Potentials (IPs) • Can produce from nonstandard and non-reservoir quality rocks	• Often a rapid decline curve • Possible early water encroachment • Size and shape of drainage area is difficult to determine • Reserve calculations difficult to constrain • Many development wells add rate but not additional reserves
Type 2: fractures provide essential permeability	
• Can develop low permeability rocks • Often higher than anticipated well rates • Hydrocarbon charge often facilitated by fractures	• Poor fracture and porosity communication leads to poor matrix recovery and disastrous secondary recovery Possible early water encroachment (production rates may need to be controlled) • Fracture intensity and dip critical • Development pattern must be tailored to the reservoir • Recovery factor difficult to determine and quite variable • Fracture closure in overpressured reservoirs may occur
Type 3: fractures provide a permeability assist	
• Reserves dominated by matrix properties • Reserve distribution fairly homogeneous • High sustained well rates • Great reservoir continuity	• Highly anisotropic permeability • Often unusual response in secondary recovery • Drainage areas often highly elliptical • Often interconnected reservoirs • Correlation between log/core analysis and well test/performance often poor
Type 4: fractures create flow barriers	
	• Reservoir compartmentalisation • Wells underperform compared to matrix capabilities • Recovery factor highly variable across the field • Permeability anisotropy opposite to other adjacent fractured reservoirs of other fracture types

Table 2.3: Attributes of fractures by NFR types. Compiled from Nelson (2001).

As earlier stated, fractures in hydrocarbon reservoirs may remain completely open, can be partially sealed, or can be completely sealed, all of which can have either positive, negative, or neutral impact on reservoir performance. Furthermore, the impact of fractures on productivity can change during the field production lifecycle (primary to tertiary recovery phases), in response to changes in reservoir pressure and fluid types. This section highlights the key effects of fractures on reservoir performance and field development from appraisal to production and late-field life.

2.3.1 *Pre-production*

Natural fractures have long been considered as an important factor for hydrocarbon accumulation and production. They are the target of hydrocarbon exploration (Aguilera, 1983; Nurmi et al., 1993; Nelson, 2001; Gale et al., 2014). They are associated with stratigraphic traps, provide the connection between matrix blocks containing hydrocarbon and producing wells, and enhance production from low porosity and low permeability reservoirs. On the other hand, they can compromise recovery and make large reserves uneconomical if they occur as barriers to flow. Thus, investigation of effect of fractures should start during the exploration stage (Bratton et al., 2006). Knowing the general orientation of fractures in a field helps to improve well planning and increases the chances for a well to intersect a conductive fracture. This is useful in appraising the potential of hydrocarbon intervals in NFR as many potentially producible reservoirs are classified as "dry hole" and abandoned because the wells did not intersect fractures (Aguilera, 1983). A properly targeted and oriented (horizontal or vertical) well in relation to fractures further allows for the collection of qualitative and quantitative geological data (such as core and image logs) for better reservoir characterisation. On the other hand, core samples with fractures will easily disintegrate and become unsuitable for estimation of bulk reservoir properties from thin sections analysis (Pirson, 1953).

Often, heterogeneity in fractured reservoirs exist across multiple length scales. Hence a representative elementary volume (REV), generally used for calculating effective reservoir properties, cannot be readily defined (Berkowitz, 2002) or has to be defined at several scales for the same reservoir ("multi-scale REV") depending on which development decision needs to be to addressed (Figure 2.8) (Bentley, 2015; Ringrose and Bentley, 2015; Bentley et al., 2017). Fractures also affect well construction and completion. Drilling through open fractures may result in loss of drilling mud, well collapse, or formation damage. Hence existing

information about fractures helps to avoid complications during drilling which may need to be rectified later through costly workovers.

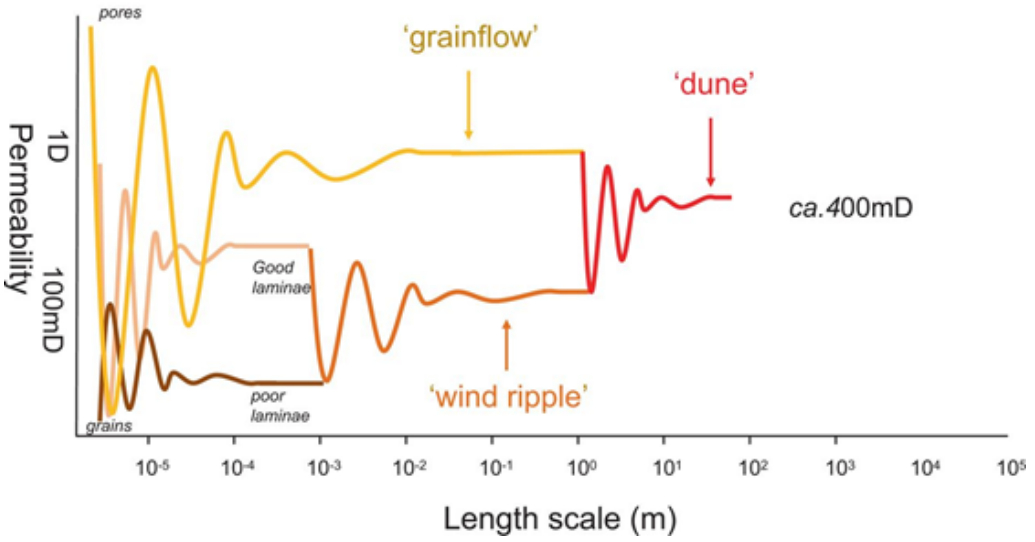

Figure 2.8: The concept of a representative elementary volume (REV). The flat portions on the REV plot indicate the average properties for each scales of the REV. After Bentley (2015).

Early reserve estimates are needed for any field development to define economic viability of a play and to select development alternatives. This is particularly difficult in NFR where fractures contribute significantly to reservoir porosity. The efficacy of conventional methods for estimation of reservoir pore volumes and reserves is impeded by the complexity of and lack of information about the fracture network (Groves and Abernathy, 1968). A sound understanding of fracture frequency, size, height, and length distribution is essential for better characterisation of reservoir connectivity, well drainage areas, inter-well connectivity, and well rates. However, it is notoriously difficult to quantify these fracture properties during the early time of reservoir development (Gale et al., 2014). Thus, fractures have significant importance and are a major source of uncertainty during the appraisal and early development stage.

2.3.2 *Primary Recovery*

The first stage of hydrocarbon production (Figure 2.9) can account for about 10-25% recovery of the original oil in place (OOIP) (Lake et al., 1992). In this case, only the reservoir's natural energy such as fluid expansion, water drive, gas drive, or gravity drainage displaces hydrocarbons from the reservoir to the surface via the wellbore. However, NFR are characterised by high initial flow capacity and rates, rapid pressure and rate decline, and low ultimate recovery during primary production (Groves and Abernathy, 1968; Allan and Sun, 2003).

In many NFR, most of the storage is in the low-permeability matrix (e.g. Type 2 and 3 of Nelson's classification) such that only the fluids in the high-permeability and low-storage fractures are produced during primary production. In particular, fractures enable production by providing and enhancing the permeability in otherwise tight matrix reservoirs such as tight gas and shale gas or shale oil reservoirs (Gale et al., 2014). Generally, both high fracture permeability and high fracture density increase a well's productivity (Huskey and Crawford, 1967). A well-connected fracture network with high permeability also implies that a reservoir can be produced using a smaller number of wells during primary production (Elkins, 1953).

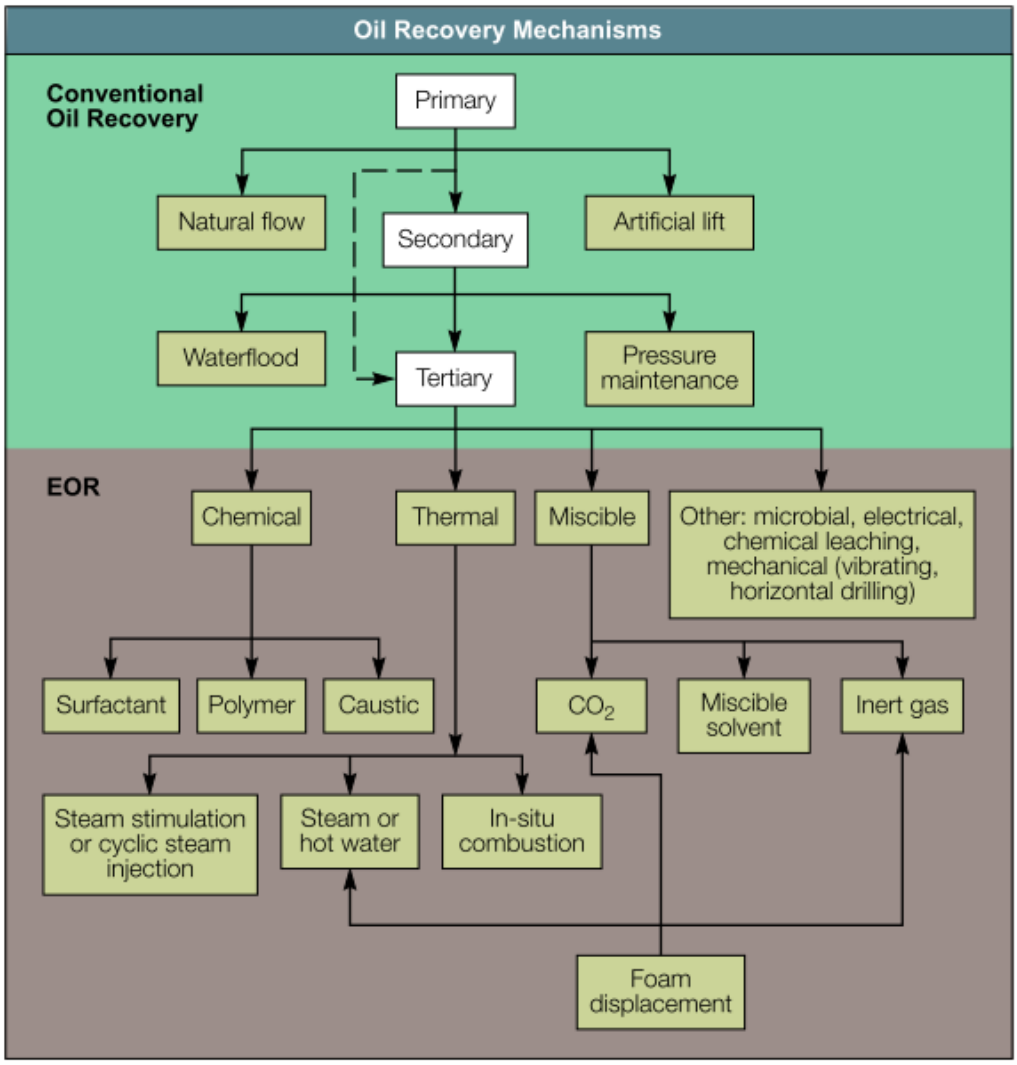

Figure 2.9: Oil recovery mechanisms. Taken from Lake et al. (1992).

On the other hand, the high-permeability of fractures can result in directional permeability and flow anisotropy. This leads to variable wells productivity indices (PI) across a reservoir, depending on whether a well is located along the fracture orientation or not. NFR also suffer from early water and gas breakthrough that sweeps only oil from the fractures but leaves behind volumes of oil

in the matrix blocks. Premature gas production can also reduce reservoir energy, may lower ultimate recovery, or damage downhole pumps. All these production problems require costly remedial actions. Even though fractures can provide connectivity to matrix blocks and link different reservoir horizons, vertical fractures also cause water, or gas coning as fluids are rapidly drawn towards the producing section of a well. As mentioned above, fractures may also close during production as the reservoir pressure decreases, which alters the impact of fractures on production over the lifetime of the reservoir.

Capillary retention and gravity segregation of gas and oil can also increase the Gas-Oil-Ratio (GOR) and reduce recovery factors in NFR (Elkins, 1953; Pirson, 1953). The GOR in an NFR can remain lower during production if the field is adequately evaluated and the intricate balance between reservoir pressure and recovery is properly managed. In this case, the solution gas can preferentially flow through fractures and form gas cap while the oil, which has a lower gas content, flows horizontally below the gas cap towards to the well. However, the GOR can increase rapid if production rates are high and the balance between pressure maintenance and recovery is lost (Allan and Sun, 2003). This effect is exacerbated in Type 3 reservoirs if the matrix is mixed- to oil-wet. A water-wet rock matrix has a strong imbibition potential, i.e. water in the fracture imbibes the matrix due to capillary forces, displacing oil from the matrix into the fractures. This effect is reduced, respectively absent, in mixed- to oil-wet reservoirs (Schmid and Geiger, 2013). Hence, the ultimate recovery tends to be higher in water-wet NFR compared to mixed- to oil-wet NFR Figure 2.10.

Generally, correlation between reservoir production performances and static geological analysis is poor in NFR. For this reason, it is difficult to calibrate static and dynamic models (Ahmed Elfeel and Geiger, 2012; Ahmed Elfeel, 2014; Arnold et al., 2016) to constrain reserve calculations and/or forecast future production behaviours.

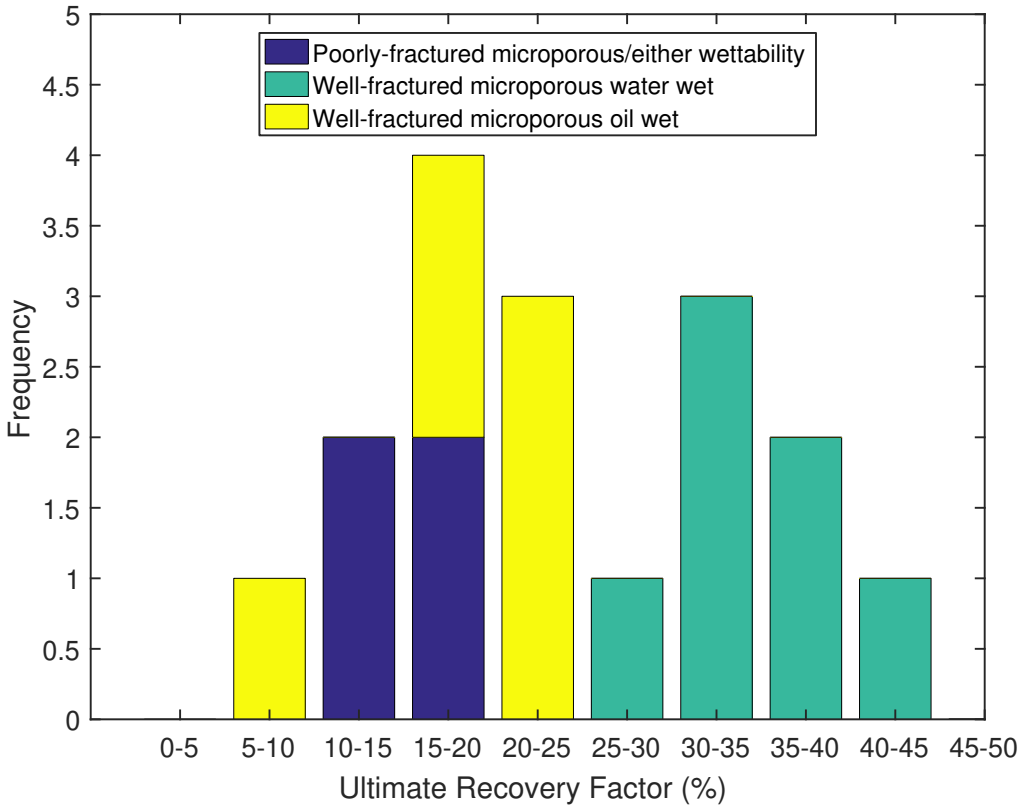

Figure 2.10: Recovery factors for 17 different NFR of Type 3. The NFR are classified by wettability and fracture intensity. After Allan and Sun (2003).

2.3.3 *Secondary Recovery*

Secondary recovery refers to the second stage of hydrocarbon recovery (Figure 2.9). Secondary recovery involves the injection of fluids (normally water and/or gas) into the reservoir in order to maintain reservoir pressure and sweep hydrocarbons from the injectors towards the producers. The challenges of secondary recovery in NFR are similar to the ones encountered during primary recovery in that fractures reduce the sweep efficiency of the injected fluids due to anisotropic permeabilities in the main fracture direction, cause channelling of the injected fluids along the fractures by passing oil in the matrix, and lead to early breakthrough of the injected fluids (Lawry, 1946; Beliveau et al., 1993; Narr et al., 2006). As during primary production, recovery factors also depend strongly on the reservoir wettability because the rate at which the matrix releases oil and replenishes the fractures is critical to the productivity of an NFR (Schmid and Geiger, 2013). Figure 2.11 and Figure 2.12 contrast the production performance of the Ekofisk and Natih fields, a water-wet and oil-wet Type 3, respectively, during waterflooding. The water-wet Ekofisk reservoir responds better to the waterflood, although other effects such as compaction drive are present in the Ekofisk field.

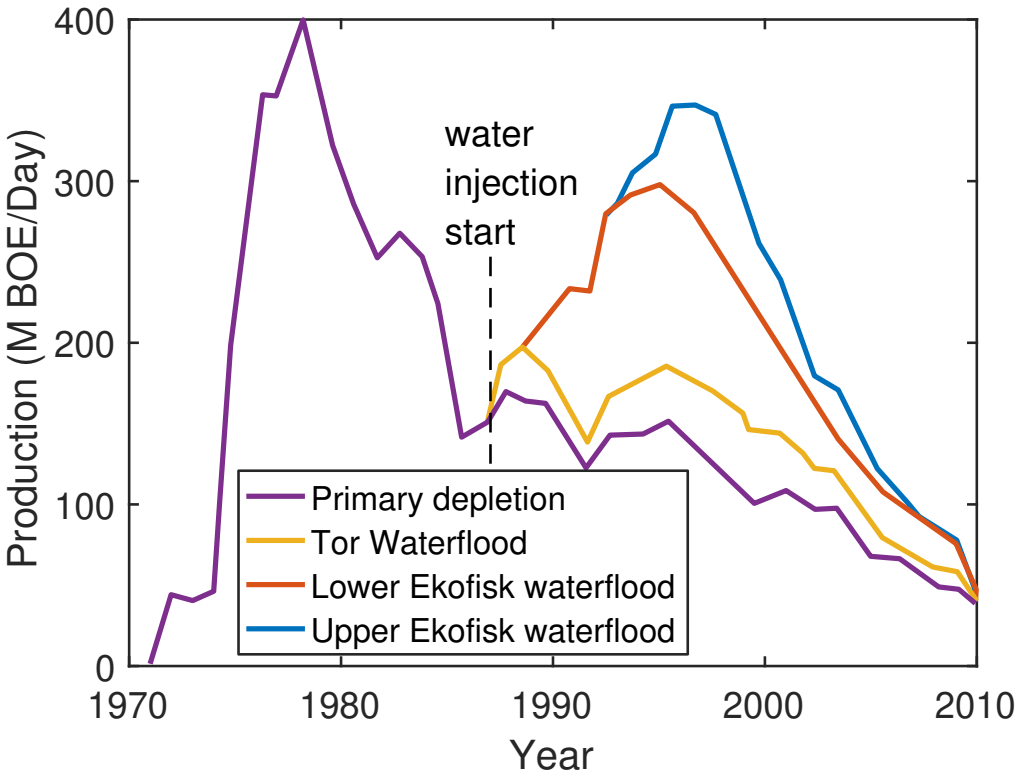

Figure 2.11: Waterflood performance from the Ekofisk Field in the North Sea, a water-wet Type 3 NFR. After Allan and Sun (2003).

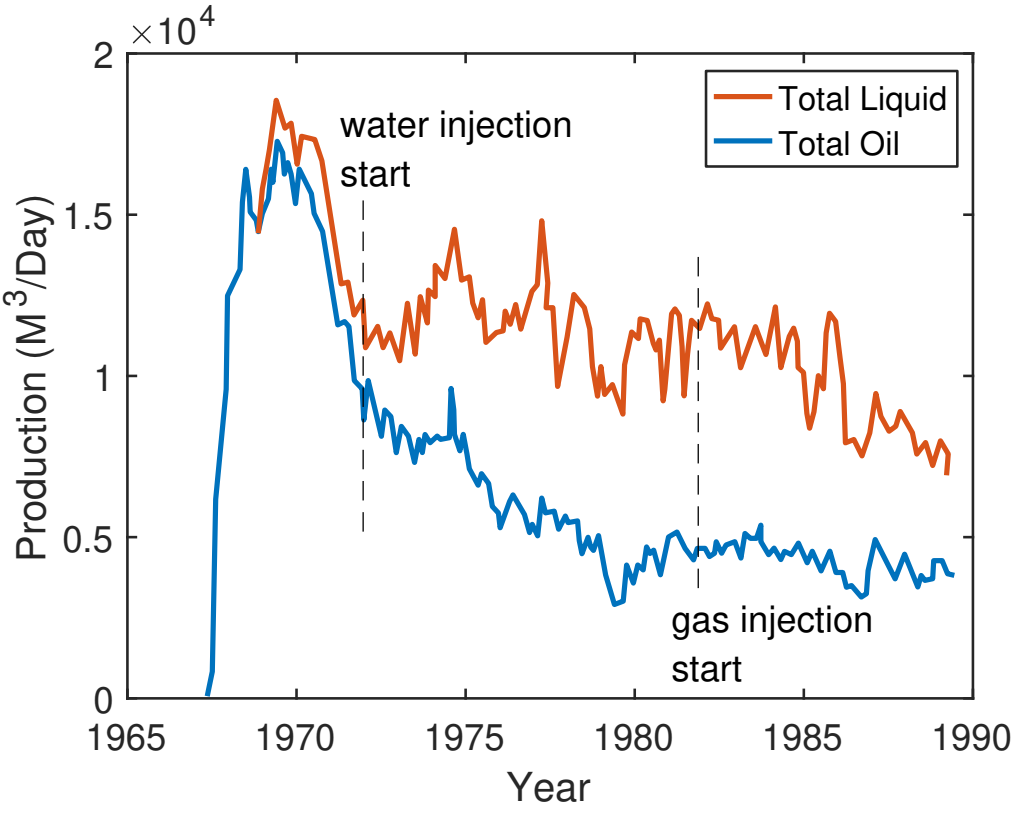

Figure 2.12: Waterflood performance in the Natih Field in Oman, an oil-wet Type 3 NFR. After Allan and Sun (2003).

2.3.4 *EOR*

EOR (also called tertiary recovery or improved oil recovery) refers to the last stage of hydrocarbon recovery (Figure 2.9). EOR aims to enhance oil displacement by altering the properties of the oil and/or reservoir, e.g. by changing interfacial tension, mobility ratios, or wettability. EOR can also help to restore the formation pressure after primary and secondary recovery. Examples of EOR methods include miscible displacement (mixing of oil with a solvent, e.g. carbon dioxide, CO_2, or hydrocarbon injection), chemical flooding (e.g. alkaline or polymer flooding), and thermal recovery (i.e. in-situ combustion or steam injection).

The approach to deploying EOR techniques has recently changed, as it has been observed that EOR methods may be most effective when they are deployed early during production rather than after secondary recovery (Al-Mjeni et al., 2010). Yet, despite the success of EOR techniques in laboratory studies (Salimi and Alikarami, 2006; Trivedi and Babadagli, 2008; Al Maqbali et al., 2015; Bourbiaux et al., 2015; Singh and Mohanty, 2016) field trails of EOR in NFR remain relatively low because of the additional geological complexity inherent to NFR (Lake et al., 1992; Firoozabadi, 2000; Al-Mjeni et al., 2010). Vertical fractures can result in gravity segregation during water-alternating-gas (WAG) EOR (Fernø, 2012). This makes it difficult to get surfactants and gas into NFR for foam injection (Al Maqbali et al., 2015). Many of attributes of fractures highlighted earlier for primary and secondary recovery also impact EOR.

2.4 CHARACTERISATION OF NFR

As discussed in the previous sections, fractures impact reservoir performance throughout the field life and have enormous effects on the way a reservoir is evaluated, developed, and abandoned. Yet it remains challenging to determine to what degree a reservoir is fractured and predict how fractures impact reservoir performance (Narr et al., 2006). The evaluation and description of a reservoir for development purposes is commonly referred to as reservoir characterisation (Corbett et al., 1998; Gringarten, 1998; Narr et al., 2006; Bush, 2010; Corbett et al., 2013). Reservoir characterisation in NFR involves the following:

- detect the presence and extent of fractures in a reservoir
- model and characterise the fractures flow behaviour, and
- understand the effects (positive or negative) of fractures on reservoir performance

Fractures are common in reservoirs but if the effect of fractures on reservoir performance is negligible, the reservoir can be treated as "conventional" reser-

voir (Aguilera, 1998). Hence the degree to which fractures affect production and recovery performance determines whether a reservoir is treated as NFR (Narr et al., 2006). Multiple geological, petrophysical, and geophysical techniques are typically integrated to first detect the presence and extent of fractures in a reservoir, secondly to characterise and model the fractures, and lastly to understand whether the fractures enhance production or provide barriers to fluid flow (*e.g.*, Bratton et al., 2006; Schlumberger, 2008; Brown, 2010; Spence et al., 2014). Data and techniques including the use of outcrop analogues, seismic attributes, well-logs (including image logs), production data, geomechanical simulations, and reservoir simulations are integrated to evaluate fractures; however, not all data may be available for a given NFR. A typical example of a detailed NFR modelling and characterisation workflow is shown in Figure 2.13. The workflow shows how various geological and reservoir engineering data are integrated in NFR characterisation. NFR characterisation begins with identifying fractures in the reservoir.

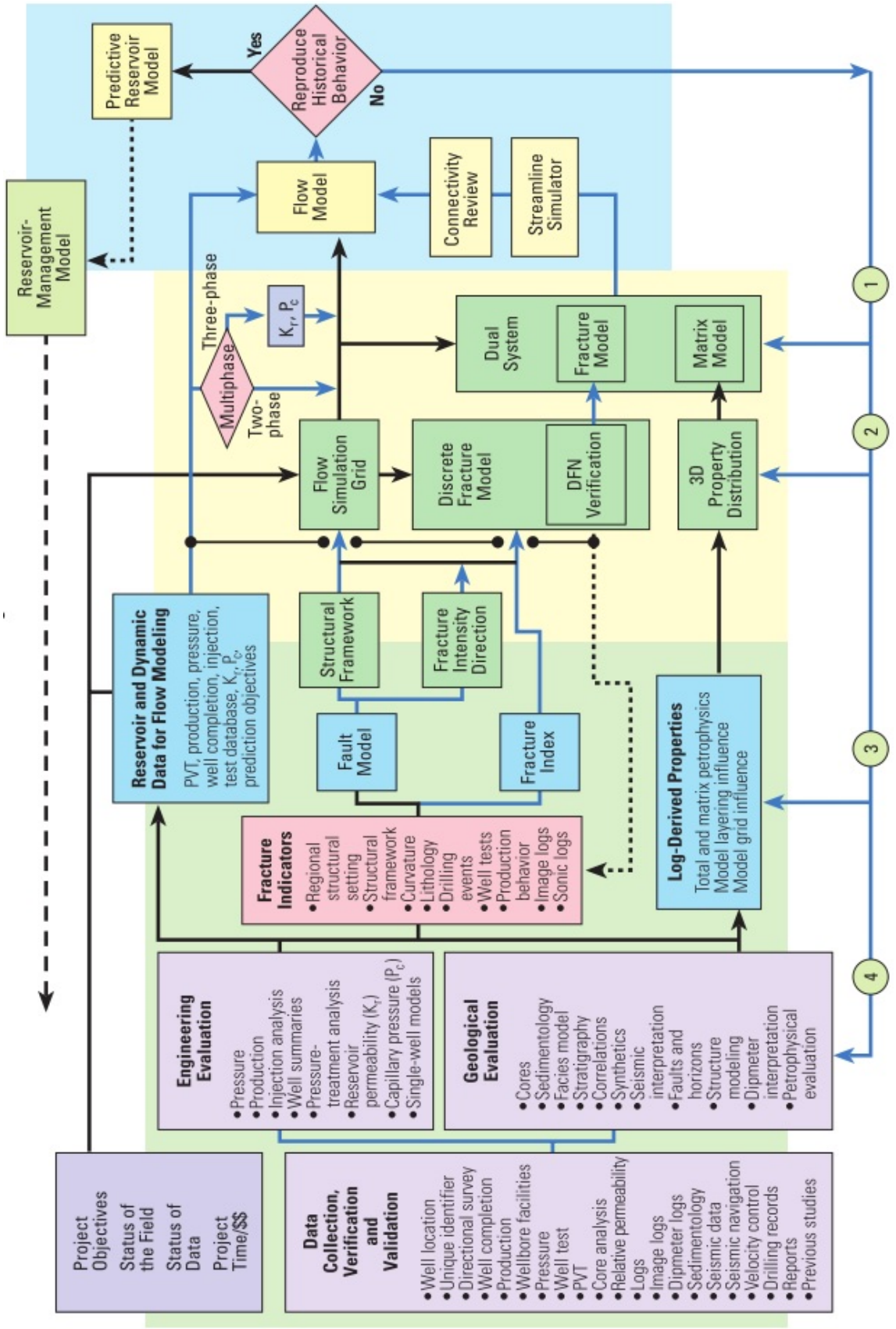

Figure 2.13: A typical industry-standard NFR modelling workflow describing the major elements involved in NFR modelling during the project startup (green background), model creation (yellow background), and model tuning (blue background). The numbers at the bottom indicate where in the workflow model tuning should take place; numbers indicate the order of preference. After Bratton et al. (2006).

2.4.1 *Identifying Fractures*

NFR characterisation should start at exploration stage, as early detection of fractures in a reservoir is invaluable to effective field development. A significant number of studies (e.g., Saidi, 1987; Aguilera, 1995, 2003; Committee on Fracture Characterization and Fluid Flow, 1996; Nelson, 2001; Bratton et al., 2006; Narr et al., 2006; Heinemann and Mittermeir, 2014; Tiab and Donaldson, 2016), describe and categorise the various methods used to identify fractures from the subsurface. These methods broadly fall into direct and indirect methods and are summarised briefly below.

Direct sources of information. These sources permit direct examination of fractures in-situ or as recovered to the surface with rock sample. Examples include core samples, wellbore images, drill cuttings, and impression packers. Reservoir cores allow for a detailed and direct evaluation and description of reservoir rocks. They can be used to determine the occurrence and orientation of fractures (Figure 2.14), and can provide information about the fractures' origin, type, geometry, aperture, porosity, permeability, density, geomechanical modifications, and mineralisation, as well as the fluid saturation, and petrophysical properties of the rock matrix. However, natural fractures observed in cores can be mistaken as drilling induced fractures. Cores that contain fractures can also be disrupted during recovering from well, handling, transportation, and storage. Core data is always one-dimensional and only samples a tiny volume of the reservoir. This is particularly difficult for fractures, as properties such as fracture spacing and fracture size are inevitably undersampled, especially in vertical wells, as these hardly intersect the frequently occurring vertical fractures. Therefore, the use of core of analysis is most effective when combined with other methods such as well logs and geophysical analysis.

Wellbore images and videos devices based on optical, acoustic, and electrical techniques can provide direct in-situ information on subsurface fractures from the interior of the wellbore. This includes the location, size, aperture and orientation of the intersected fractures. They can also indicate if a fracture is filled with minerals and provide information of present day stress direction using the orientation of reservoir features intersected by the wellbore. The drawback to these methods is that they can be negatively impacted by the presence of drilling mud and, as with core samples, they only provide one-dimensional information.

Drilling cuttings, as well as thin sections of drilling cuttings, also provide useful indication of fractures as fractures planes may be preserved on the cuttings. However, a reservoir may be fractured without any indication on the drilling cuttings.

Another direct indicator of fractures are impression packers coated with soft pliable impression packers. Uninflated packers are lowered to the wellbore section of interest and then pressured. The soft coating presses against and conforms to features on the walls of the wellbore, including fractures. The impression on the coating materials provide good indication of fractures that are intersected by the well. This method is limited to uncased wellbores and only provides one-dimensional information.

Figure 2.14: 10cm vertical core showing fractures observed in a vertical well. The core is continuous from upper left to lower right. Taken from Narr et al. (2006).

Indirect sources of information. These include drilling history, mud logs, well logs, seismic information, outcrop analogues, production logging tool (PLT), production history, and well-test data.

Drilling history and mud logs obtained during the drilling provide useful information regarding the presence of fractures. Loss of circulation, change in rates

of penetration, and rapid increase in gas shows in the mud while drilling may all be good indicators of open and conductive fractures. While loss of circulation indicates the presence of fractures, it also causes mud circulation problems and results in the loss of expensive drilling mud, and potentially even the loss of the well.

When combined with image logs, well logging can provide useful information about the fracture characteristics. Examples of well logs include Stoneley Wave logs, used to indicate the aperture of open fractures or sonic and density logs for the recognition of open fractures, and their porosity. Photoelectric effect logs also detect open fractures, if used with barite mud. Spontaneous potential logs indicate anomalous contrast in electrical potential between drilling mud and formation water, and the clay materials of the permeable fracture zones. Temperature logs can detect fractures as fracture zones often exhibit cooler temperatures because cool drilling mud was circulated through them.

Table 2.3 shows how fractures can be interpreted from various well logs. Well logs are more effective when they are combined with other methods. They can be misleading when used in isolation; for example, vugs, washout zones, or borehole rugosity could be mistaken as fractures in Stoneley wave and photoelectric effect logs, or drilling fluids can yield erroneous readings on temperature logs.

Seismic data such as time of arrival of reflection (or refraction) of acoustic waves from a geological surface and the shape of the reflection can provide information on the reservoir structures, lithology and stratigraphy. Major structures such as faults with sufficient vertical displacement can be identified and used to establish the dominant structural orientation and style of reservoir. In addition, the presence and direction of propagation of reservoir anisotropy influence seismic wave velocity. Since fractures produce anisotropy, the anisotropic reflection and refraction of seismic waves can support the identification of fracture characteristics such as fracture orientation and density. However, many fractures are below seismic resolution and hence can go undetected on seismic data.

Another important source for fracture characterisation comes from outcrop analogues as outcrops allow for a detailed observation of 2D and 3D fracture distributions, types, styles, and orientation, possibly even at the inter-well scale (Seers and Hodgetts, 2013; Geiger and Matthäi, 2014; Howell et al., 2014).

Production logging tools (PLT) are useful to identify fractures based on dynamic data and can estimate flow capacities of fractures prior to the actual production. PLT information can be correlated with the core-derived facies permeability to analyse any impact of fractures.

The production history also allows us to evaluate the effect of fractures in a reservoir. During hydrocarbon recovery, the actual production rates and reservoir performance may be many times higher than estimated. On the contrary,

the reservoir may underperform. This may indicate the presence of fractures that were undetected and/or misinterpreted during evaluation.

Log Type	Measurement	Conventional Interpretation	Fracture Interpretation	Reference
Natural gamma	Formation gamma emission	Clay mineral fraction	Radioisotopes as infilling	Keys, 1979; Aguilera 1980
Neutron	Neutron flux attenuation	Porosity, clay fraction, water saturation	Alteration minerals and hole enlargements	Nelson and others, 1983; Paillet, 1991a
Resistivity	Formation electrical resistivity	Water salinity and lithology	Alteration minerals, hole enlargements, water quality, and permeability	Keys, 1979; Katsube and Hume, 1987
Gamma-gamma	Gamma flux attenuation	Density and porosity	Lithology and hole enlargements	Keys, 1979; Paillet, 1991a
Acoustic	Compressional wave travel time along borehole wall	Porosity and lithology	Alteration and fracture porosity	Paillet, 1991a; Keys, 1979
Acoustic waveform	Acoustic pressure signal	Shear velocity	Tube-wave attenuation, fracture transmissivity	Paillet, 1991a, 1983; Hornby and others, 1989; Tang and others, 1991
Temperature	Borehole fluid temperature	Thermal conductivity of formation	Inflow and outflow to borehole	Keys, 1979; Paillet, 1991a: Keys and Sullivan, 1979
Spontaneous potential	Natural shale "membrane" effect	Water salinity and clay mineral fraction	Streaming potential	Keys, 1979
Fluid conductivity	Electrical conductivity of borehole fluid	Salinity of borehole fluid	Inflow and outflow to borehole	Keys, 1979; Hess and Paillet, 1990; Paillet, 1991a
Caliper	Borehole diameter	Drilling damage and fractures	Hole enlargement	Keys, 1979; Paillet, 1991a
Flowmeter	Vertical flow in borehole	Permeability	Inflow and outflow to borehole	Hess, 1986; Hess and Paillet, 1990

Table 2.4: Interpretation of fractures from well logs. After Paillet (1994).

2.4.2 *Pressure Transient Response in NFR*

Another indirect and important source of information on fractures comes from well-tests. Linking well-test data to fracture detection is the central focus of this PhD thesis because pressure transient data obtained during well-testing can offer important information as to whether a reservoir is fractured or not, and can help to identify large-scale flow behaviours, especially during the appraisal and development stage (Earlougher, 1977; Bourdet, 2002). It should be noted that well-testing is not restricted to detecting fractures in a formation. For completeness, Table 2.5 shows the various applications of well-test analysis throughout the field life.

Activity	**Exploration**	**Appraisal**	**Early Production**	**Late Production**
Objective	Are there hydrocarbons in the reservoir?	What types of hydrocarbons? Productivity?	Completion efficiency Changes in productivity Reservoir pressure response to production	Understand productivity anomalies After stimulation to check PI improvement
Type of test	DST or production test	Production test	Production test	Production test
Frequency	Once	Once	Once	By exception

Table 2.5: Typical objectives of well-testing during the field life cycle. After AGR Tracs (2014).

3

GEOENGINEERING WORKFLOW FOR INTEGRATED WELL-TESTING

3.1 INTRODUCTION

Different methods for modelling of NFR have been developed and are well reported in the literature (Barenblatt et al., 1960; Warren and Root, 1963; Aguilera and Van Poollen, 1977; Dean and Lo, 1988; Chen, 1989; Kazemi and Gilman, 1993; Kim and Deo, 2000; Berkowitz, 2002; Bogdanov et al., 2003; Karimi-Fard et al., 2004; Monteagudo and Firoozabadi, 2004; Li and Lee, 2008; Geiger et al., 2009; Lemonnier and Bourbiaux, 2010a; Hajibeygi et al., 2011; Kuchuk and Biryukov, 2012; Krevor and Fitch, 2015; Moinfar et al., 2013; Ahmed Elfeel, 2014; Maier, 2014; Bosma et al., 2017). These techniques can be broadly divided into two categories - equivalent continuum models and discrete methods. Examples of equivalent continuum models are the dual-porosity and dual-permeability models. Examples of discrete methods are the Discrete Fracture Network (DFN) model, the Discrete Fracture Matrix (DFM) model and the Embedded Discrete Fracture Matrix (EDFM) model. Table 3.1 shows comparisons of continuum models and discrete models using common simulation criteria and Figure 3.1 illustrates the representation of fractures with different methods. A brief description of the dual-continuum model and the DFM model, which is used in this study, are presented below.

CRITERIA	CONTINUUM MODELS	DISCRETE MODELS
Computational cost	Low (hours)	High (days)
Simulation scale	Large (reservoir)	Small (outcrop)
Simplification of geology and physics	High (e.g. transfer functions)	Low (e.g. fractures represented explicitly)
Effective properties	Required	Optional
REV	Required	Optional
Upscaling	Required	Optional
Fracture representation	Implicit	Explicit
Level of resolution	Uniform properties in each reservoir model grid block	Features below scale of a reservoir model grid block are resolved

Table 3.1: Comparison between continuum models and discrete models

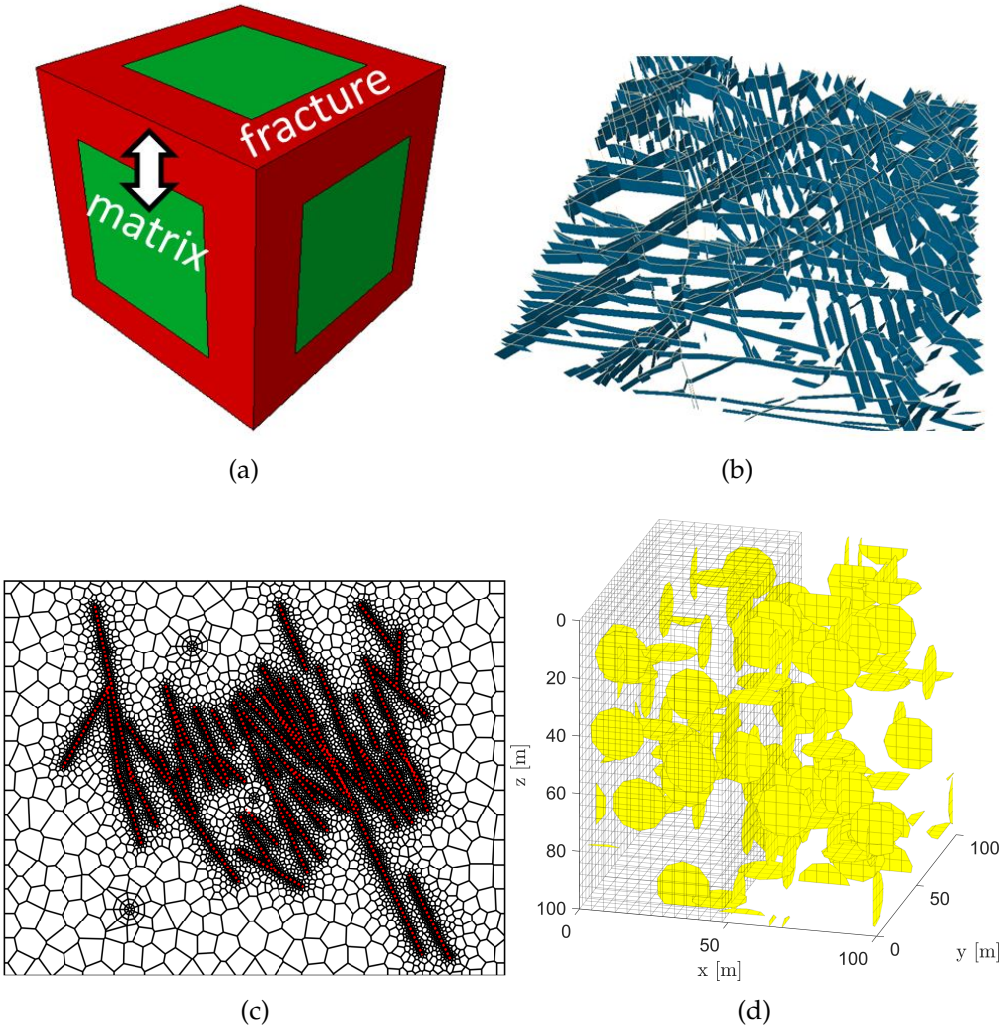

(a) (b)

(c) (d)

Figure 3.1: Types of fracture models showing, (a): the dual-porosity model (Ahmed Elfeel, 2014), (b): the discrete fracture network model (Ahmed Elfeel, 2014), (c): the discrete fracture matrix model of this thesis, and (d): the embedded discrete fracture matrix, (courtesy of Daniel Wong, PhD student at HWU).

3.1.1 *Dual-Continuum Models*

The dual-porosity model, introduced by (Barenblatt et al., 1960) and developed by (Warren and Root, 1963), for simulation of fluid flow in NFR consist of two systems: fractures with high flow capacity but low storativity and a matrix with negligible flow capacity but significant storage. This model has been adopted as the industry standard for simulating NFR and remains the underlying model in commercial reservoir simulators. Typical features of this model are listed in Table 3.1 and other assumptions have been discussed in Chapter 1. As fractures are not explicitly represented in this model, the interaction between matrix blocks and fractures is modelled via transfer functions (Kazemi et al., 1976). Furthermore, the dual-porosity model has been extended to dual-permeability for scenarios where matrix flow is significant. Other extensions include the multiple subregion (MSR) model (Gong et al., 2013), the multi-rate dual-porosity model (Geiger et al., 2013; Maier, 2014), or the triple-porosity model (Clossman, 1975; Abdassah and Ershaghi, 1986). The classic dual-porosity V-shape in simulated well-tests data is a characteristic pressure behaviour corresponding to the interaction of fractures and matrix in this model, as discussed in detail in Chapter 1.

3.1.2 *Discrete Fracture-Matrix (DFM) models*

The DFM model is an important alternative to the dual-porosity model when simulating fluid flow in NFR (Kim and Deo, 2000; Karimi-Fard et al., 2004; Geiger et al., 2009; Moinfar et al., 2013; Geiger and Matthäi, 2014). The DFM approach allows us to resolve the fractures in dynamic reservoir models without over-simplification of the reservoir geology. One of its key differences compared to the dual-porosity model is the explicit representation and simulation of fractures and matrix (other features of this model are listed in Table 3.1). Hence, the exchange of fluids between fractures, between fractures and matrix, and between matrix blocks occurs naturally in flow simulations and without the need for transfer functions (although at significantly increased computational cost). This approach can provide reference solutions for the validation and calibration of the fracture-matrix transfer formulations used in dual-porosity simulators (Lemonnier and Bourbiaux, 2010a). It also has the potential to provide results that support the correct interpretation of transient pressure responses in NFR (Geiger and Matthäi, 2014; Egya et al., 2018c). Geological well-testing with the use of DFM techniques allows us to properly rank different geological scenarios considered for a field development (Corbett, 2009; Corbett et al., 2012; Agada et al., 2013) and calibrate simulation models considering the key reservoir features that control fluid flow (Egya et al., 2018a).

A geoengineering workflow (Figure 3.2) introduced by Corbett (2012); Corbett et al. (2012) and adapted in this thesis (Egya et al., 2018c,a,b) combined DFM modelling techniques using unstructured-grid reservoir simulations to generate synthetic pressure transients for different fracture geometries. The workflow enabled us to correlate the pressure transients to the known geological features present in the reservoir model in order to investigate which geological features account for a given pressure response. The geoengineering workflow can be summarised in the following steps:

i. Build high-resolution synthetic geological models comprising conceptual fracture networks or realistic fracture patterns (e.g., observed in an outcrop-analogue). Data required at this stage include fracture orientation, length, aperture, connectivity, and reservoir horizons.

ii. Use petrophysical properties from logs that are representative of a given subsurface reservoir. This data included permeability, porosity, PVT etc.

iii. Represent the geological model in a reservoir simulation model that employs unstructured grids so that the fractures can be preserved explicitly. Details of the unstructured-grid generations is provided in the section below.

iv. Numerically simulate drawdown / build-up for a wide range of possible reservoir parameters (e.g., fracture conductivity and well locations). This stage requires initial reservoir conditions e.g., pressure and saturation as well as well parameters including radius, length and orientation.

v. Analyse the resulting numerical pressure transient data in a standard well-test package. Besides pressure and rate data collated from the flow simulation, the minimum data required for the analysis are fluid type, well orientation, wellbore radius, formation thickness, porosity, formation volume factor, viscosity and total compressibility.

vi. Estimate the effective reservoir parameters for the simulation model. Typical reservoir properties that is estimated from the analysis include permeability thickness product, skin, fracture length and conductivity, radius of investigation etc.

vii. Correlate the pressure transient to the known geological features in the reservoir model. Where the analysis disagrees with model input and geological understanding, make necessary changes to the reservoir model to test other reservoir concepts and improve model performance.

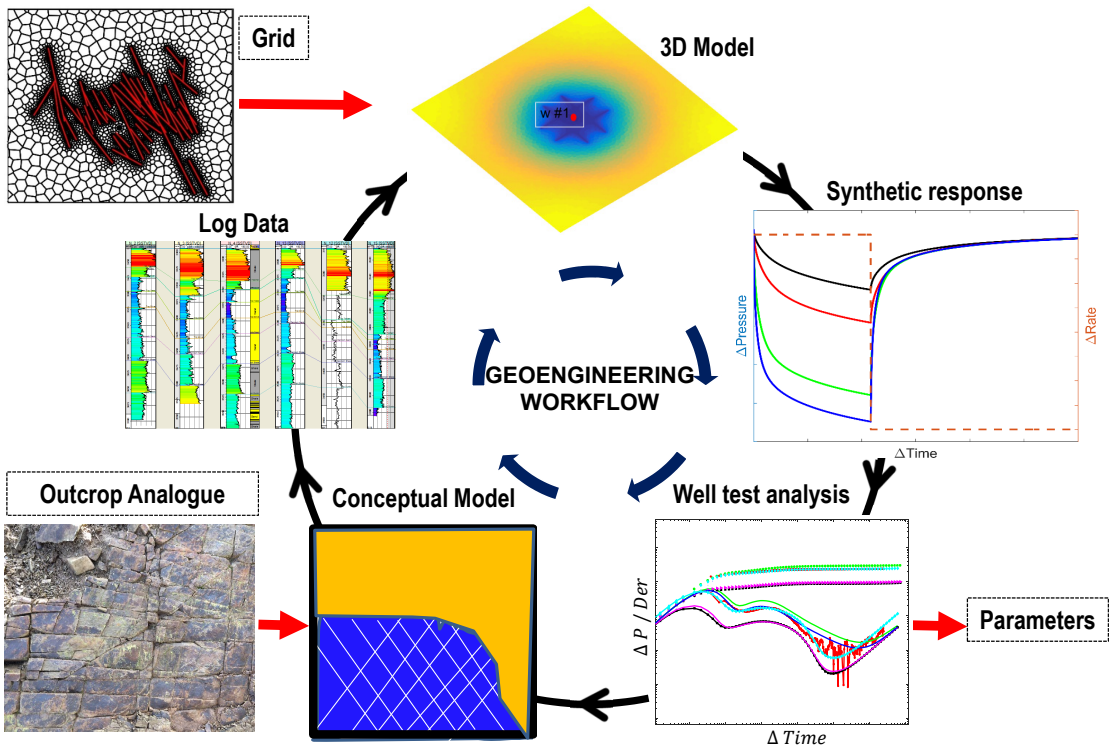

Figure 3.2: Geoengineering workflow for integrated well-testing.

The reservoir models can be created using various geophysical, geological, petrophysical and production data. Examples of this include geological / regional structural setting, structural framework, reservoir horizons, lithology, drilling events (such as mud loss and changes in rate of penetration) borehole images, and flow logs. Fluid properties (PVT), rock properties (e.g. permeability and porosity) are derived from petrophysical analysis. For investigations of field data in this thesis, the conceptual models are created and constrained using both the field's static geological data and dynamic (pressure and rate) data. Where synthetic, idealised fracture geometries are used, realistic subsurface reservoir properties are used for the flow simulation. The DFM-based geoengineering workflow in this thesis uses the numerical methods available in the open-source Matlab Reservoir Simulation Toolbox (MRST) (Lie et al., 2012). The DFM simulations solve the diffusivity equation numerically and explicitly resolve the fractures in the reservoir models. This approach hence allows us to analyse the impact of the fracture network geometry as well as well locations on the pressure transient signals. MRST offers a range of discretization methods. Here, we employ the PErpendicular Bisector (PEBI) method, which has proven to be efficient, robust and accurate when discretizing complex fracture networks (Sun and Schechter, 2015). The conditions for accurate PEBI simulations are that the permeabilities are isotropic and permeability orthogonality is guaranteed. However, the main advantage of the PEBI approach is its flexibility, enabling the grids to conform

to complex geometrical features, including fractures and radial gridding around the wells, whilst resolving the early time transients (Zheng et al., 2007).

3.2.1 *Fracture Mesher Implementaion in MRST*

The gridding of the simulation model with explicit fractures is completed using a new Carbonate Research Group in-house module (2D fracture mesher) developed in MRST for this PhD research. This unstructured PEBI grid mesher is implemented using existing Triangle (Shewchuck, 2002) and PEBI grid algorithm available in MRST (Lie et al., 2012). The code excerpt below outlines the implementation of the fracture mesher in MRST.

```
2D Fracture Mesher Developed in MRST
%% Define Specify grid information
% Create cell arrays with fracture cordinates
fractures = cell(0,0);
% Import/define fracture cordinates(X1,Y1;X2,Y1)for fractures{i}=1:n
fractures{i}= [X1,Y1;X2,Y2];
% Divide fractures into segments equal to desired aperture
function[fractures] = smart_refine_fractures(fractures,grid_aperture);
    for i=1:length(fractures)
    end
end
% Define the reservoir model boundary
xylimits = [x1 x2;y1 y2];
% Specify max area of the triangle mesh to be created
max_area = [];
% Well locations for number of wells, i=1:n
Wpt{i} = [x1,y1];
%% Generate triangle grid over a 2D domain limited by 'xylimits' array
% and having as restrictions the fractures defined by 'fractures' cell
% array. 'max_area' define the general size of a triangle and controls the
% refinement of the final mesh
G = create_triangle_fractured_grid(xylimits,fractures,max_area, varargin);
function [G,points,triangles] = create_triangle_fractured_grid(xylimits,...
           fractures,max_area, varargin)
    % Input arguments to call Triangle Mesh Generator.
    arg = ['-a' num2str(max_area) 'Anepq30CVF'];
        %where NUM2STR Convert numbers to character representation
    filename = '.temporary_triangle_files';
        function []=write_poly_file(filename,xylimits,fractures,max_area);
        end
    %% Generates Triangle2D files
```

```
    run_Triangle_poly(filename,arg);
        function []=run_Triangle_poly(filename,arguments)
        end
    % Reading Triangle2D files
    points = read_Triangle_nodes([filename '.1.node']);
        function [ points ] = read_Triangle_nodes( filename )
        end
    triangles = read_Triangle_elements([filename '.1.ele']);
        function [ triangles ] = read_Triangle_elements( filename )
        end
    % Generating Grid, assigning tags and appertures
    opt = struct('randomPerturb', [],...
                 'padding', [],  ...
                 'uniform', true, ...
                 'wells',   [], ...
                 'wellseg', [], ...
                 'radius',  [], ...
                 'radnum', [], ...
                 'growthfactor', [], ...
                 'extraPts',    [], ...
                 'lines',       {{}}, ...
                 'randomizePoints', false);
    opt = merge_options(opt, varargin{:});
        function [prm, varargout] = merge_options(prm, varargin)
        end
    % Add radially refined wells
    Pts = points(:,2:3);
        if ~isempty(opt.wells)
            for i = 1:size(opt.wells, 1)
            Pts = insertWellRefinement(opt.wells(i, :), Pts, R(i),...
                WS(i), NR(i), GF(i));
            end
        end
    %% Delaunay Triangulations
    Tri = delaunayTriangulation(Pts);
    G = triangleGrid(Pts, Tri.ConnectivityList);
        function G = triangleGrid(p, varargin)
        end
    %Delete all the files no longer required after the mesh generation
    clean_the_mess();
        function [  ] = clean_the_mess(  )
        end
end
```

```
%% Compute dual grid (G2) of triangular grid (G).
G2 = pebi(G);
%Extrude 2D grid to layered 3D grid with n layers.
G2 = makeLayeredGrid(G2, n); %n = number of layers
%Compute geometry of grid.
G2 = computeGeometry(G2);
```

3.2.2 *PEBI Grid Generation*

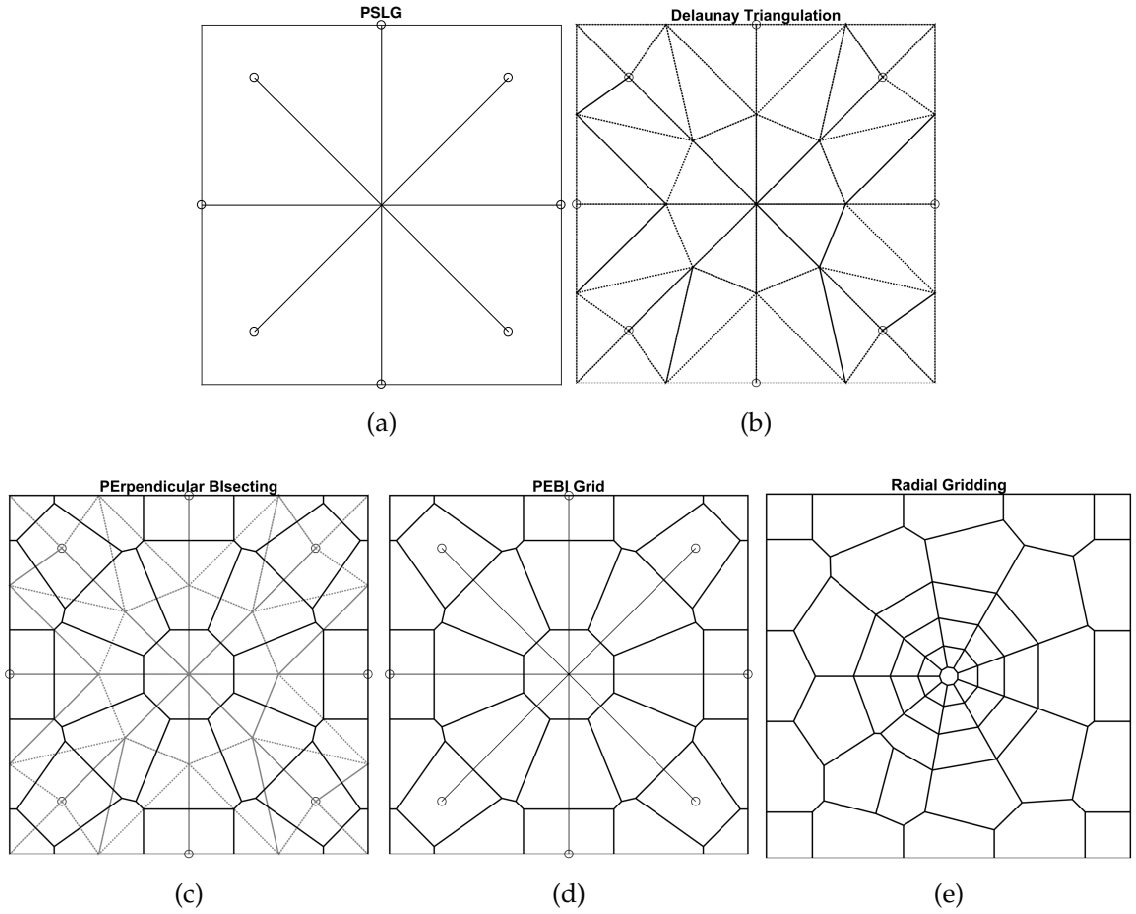

Figure 3.3: Mesh generation showing a planar straight-line graph (PSLG) representing sets of fracture nodes and adjoining edges (a), the Delaunay triangulation (grey dash lines) (b), the PEBI grid built around triangular mesh nodes (c), the resulting PEBI grid with respect to the initial PSLG (d) and a separate meshing example showing radial gridding around a well (e).

The PEBI gridding workflow used in this study is illustrated in Figure 3.3. Fracture traces, well locations, and domain boundaries are represented in the form of linear coordinates. Edges are then delineated by creating a planar straight-line graph (PSLG) containing a set of fracture vertices and adjoining edges (Figure 3.3a). The PSLG provides the input for a constrained Delaunay triangulation (Figure 3.3b) that honours the original model geometry (Shewchuck, 2002). The

resulting triangulation forms the basis on which the complementary PEBI grid is generated such that the centres of the PEBI cells correspond to the nodes of triangular elements (Figure 3.3c). Finally, the 2D PEBI grid (Figure 3.3d - without the drawn PSLG) is extruded vertically, resulting in a 2.5D reservoir simulation grid that is horizontally unstructured but vertically structured (Mallison et al., 2010; Lie et al., 2012; Sun and Schechter, 2015). It is often referred to as 2.5D rather than 3D because the geology/geometry does not change in the third dimension. Throughout this work, we assume that the thickness of the formation is small compared to its lateral extent, and hence no variations in structure occur in the third dimension. Furthermore, the grid around the wells and fractures was locally refined to ensure that steep pressure gradients near wells and, at early time, near the fracture-matrix interfaces, can be preserved accurately.

To enable this grid refinement, a procedure was implemented to improve the quality of the mesh at multiple fracture intersections as well as at asymmetric and low-angle intersections. Various approaches have been used to resolve meshing of complex geometry features including small features, sharp angles in intersection features, multiple features intersection, or non-uniform fracture apertures (Branets et al., 2009; Syihab, 2009; Mallison et al., 2010; Olorode et al., 2013; Hyman et al., 2014; Bahrainian et al., 2015; Sun and Schechter, 2015; Houze et al., 2017). Here, we developed an algorithm that involves creating a protective area where only one finite element node is allowed at the intersection and no grid refinement is applied within this area local to the intersection (Figure 3.3a to Figure 3.3c). Note that the image in Figure 3.3d shows an improved mesh where the PEBI cell is constructed around the initial finite element node and the adjoining cells conform to the defined fracture geometry. In addition, we applied the algorithm of Møyner and Lie (2016) to refine the grid radially around the well, especially in cases where wells are located in the matrix and close to fractures (Figure 3.3e).

To ensure that numerical artefacts do not impact the simulation results, we tested how grid refinement around the fractures and well, as well as the selection of time-steps, influence the numerical simulations by comparing numerically generated pressure profiles to analytical solutions for various levels of grid refinement and time-steps. Based on this analysis, all models use grids that coarsen logarithmically away from the smallest geometric feature (i.e., the grid blocks containing the fractures) and set the maximum grid block size to be four orders of magnitude larger than the smallest grid block in the model. Simulation time-steps are also increased logarithmically to ensure smooth pressure transients. The simulation results were further compared, for simple orthogonal fracture patterns, to a commercial simulator (CMG IMEX).

3.2.3 *Numerical Simulation Model*

All simulations presented in this study assume that Darcy's law applies and consider single-phase flow of a slightly compressible fluid where gravity effects can be ignored. The matrix of the reservoir is homogenous and isotropic and the reservoir and fluid properties (i.e. the hydraulic diffusivity, η) are constant outside the fracture network and independent of pressure. The total compressibility, C_t is derived from the formation compressibility, C_{fm} and a single-phase fluid compressibility, C_{fd}, and given by

$$C_{fm} = \frac{1}{\phi}\frac{\partial \phi}{\partial p}, \qquad C_{fd} = \frac{1}{\rho}\frac{\partial \rho}{\partial p}. \tag{3.1}$$

where p, ϕ, and ρ denote pressure, porosity, and fluid density respectively.

Assuming that the fluid compressibility is constant and independent of pressure, C_t is defined as

$$C_t = C_{fm} + C_{fd} = constant. \tag{3.2}$$

The geoengineering workflow then numerically solves the diffusivity equation

$$\frac{\partial p}{\partial t} = \nabla \cdot [\eta \nabla p], \qquad \eta = \frac{\mathbf{k}(\mathbf{x})}{\phi \mu C_t}, \tag{3.3}$$

for given reservoir properties and reservoir geometries where t, $\mathbf{k}(\mathbf{x})$, and μ denote time, the (spatially varying) permeability tensor, and constant fluid viscosity, respectively.

Consider a well (Figure 3.4) producing at constant rate q from a reservoir with an initial reservoir pressure p_0 at time $t = 0$. The reservoir is infinite, isotropic and homogeneous and contains a vertical wellbore, without wellbore storage and skin, that fully penetrates the formation. From the radial form of the diffusivity equation, the following dimensionless variable are presented for simplicity

$$\text{Dimensionless time, } t_D = c_1 \frac{k_m}{\phi \mu \ C_t r_w^2} \Delta t, \tag{3.4}$$

$$\text{Dimensionless pressure, } p_D = c_2 \frac{k_m h}{q \beta \mu} [p_0 - p_{wf}(\Delta t)], \tag{3.5}$$

where c_1 and c_2 are unit conversion coefficients given as 0.0002637 and 0.007082 in oilfield units, respectively, and k_m, h, q, β, p_0, and p_{wf}, denote matrix permeability (in mD), formation thickness (in ft), rate of production (in stb/day), formation volume factor (in Rb/stb), initial pressure (in psi), flowing well pressure (in psi). For fractured wells with vertically oriented fractures as modelled in this study, the well radius, r_w, is replaced with fracture half length, l_w.

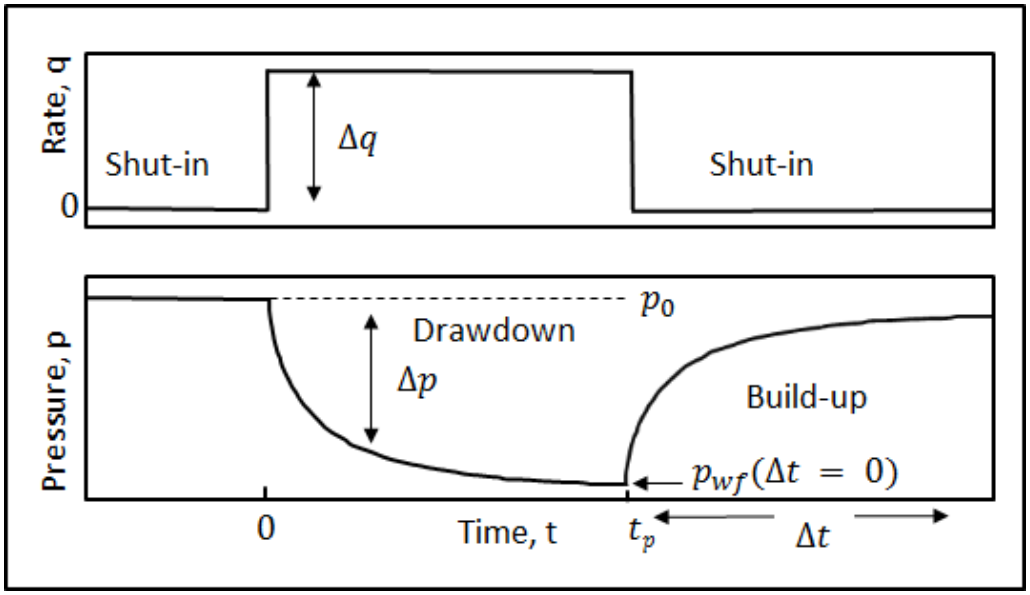

Figure 3.4: Idealised well-test flow rate and pressure response. Δq, p_0, Δp, p_{wf} denote change in flow rate, initial reservoir pressure, change in pressure and reservoir pressure at the point of well shut-in. t_p and Δt denote time of at the point of well shut-in and elapsed time after shut-in.

Once the 2.5D reservoir model is constructed (Figure 3.3), it is populated with representative subsurface petrophysical properties, including porosity and permeability that are used as input for flow computations. For simplicity, the reservoir matrix is assumed to be isotropic and homogeneous so that single constant values of petrophysical properties can be used, but heterogeneous matrix properties are possible too. The fractures are assumed to be open (100% porosity), have higher permeabilities than the matrix, and also have constant properties (either uniform or heterogeneous) that do not change as a function of pressure (i.e., the reservoir is stress-insensitive). Fracture permeability k_f is computed from the fracture aperture, a, using the parallel plate law, i.e., $k_f = a^2/12$. To avoid infeasibly small grid cells in the fracture, we rescaled the fracture permeability and porosity, in case a fracture grid block was wider than the fracture aperture to obtain the correct fracture volume and fracture transmissibility. This scaling is given by

$$S_f = \frac{a_r}{a_g}, \tag{3.6}$$

where S_f, a_r and a_g denote scaling factor, real fracture aperture, and aperture represented in the grid, respectively. For instance, where the fracture real aperture is $1mm$ (i.e. $0.001m$) and the width at which the aperture is represented in the grid is $0.1m$, the scaling factor, S_f is 0.01. Assuming an open fracture with 100% porosity ($\phi_f = 1$), the fracture porosity assigned to refined cells with fracture, ϕ_{fcell} is therefore multiplied by the scaling factor. That is, $\phi_{fcell} = 0.01 * 1$. From the parallel plate relationship, a $1mm$ fracture aperture corresponds to a fracture permeability of $83,333,333mD$ (i.e. $8.333x10^{-8}m^2$). When scaled to simulation grids size ($0.1m$) as illustrated above, the fracture permeability value represented in reservoir grid cell, k_{fcell} is $833,333.33mD$. For the unambiguous comparison of our simulation runs that consider different fracture permeabilitilies, and for comparison with published results, we further introduced the dimensionless fracture conductivity F_{CD} defined as

$$F_{CD} = \frac{k_f \cdot a}{k_m \cdot l_w}. \tag{3.7}$$

Where required for our investigations, the effects of wellbore (e.g. wellbore storage or skin) are modelled using the approach of Kamal and Co (1986), such that

$$C = V_w C_t, \tag{3.8}$$

and

$$k_s = \frac{k_m}{1 + S(\frac{r_s}{r_s - r_w})}, \tag{3.9}$$

where C is the wellbore storage coefficient (in RB/psi) and V_w and C_t are the wellbore volume (in ft^3) and total compressibility (in psi^{-1}), respectively. k_m, k_s, S, r_s and r_w are reservoir permeability (in mD), reduced permeability due to skin (in mD), skin factor, radius of region of reduced permeability due to skin (in ft), and wellbore radius (in ft), respectively.

3.2.4 *Well-test Analysis*

Once a numerical simulation has been performed, the resulting pressure transient is analysed using a standard well-test package. The analysis is based on the assumption that the changes in pressure in a reservoir resulting from the change in production rate reflect the geometric features and fluid properties of

the reservoir (Bourdet, 2002; Ahmed and McKinney, 2005). From the analysis, the pressure response and other known reservoir properties can be used to estimate unknown properties of the reservoir within the radius of investigation of the well. The unknown parameters may include, but are not limited to average permeability, skin, fracture length, reservoir heterogeneities, or reservoir boundaries. A diagram of an idealised pressure response, drawdown and build-up, is illustrated in Figure 3.4.

From the well-test drawdown in Figure 3.4, the reservoir performance can be measured by the productivity index $PI = (\frac{q}{p_0 - p_{wf}})$. For well-test analysis, the diffusivity equation for fluid flow is most often expressed in radial coordinates (Figure 3.5) as

$$\frac{\partial^2 p}{\partial r^2} + \frac{1}{r}\frac{\partial p}{\partial r} = \frac{1}{c_1}\frac{\phi \mu C_t}{k}\frac{\partial p}{\partial t}. \tag{3.10}$$

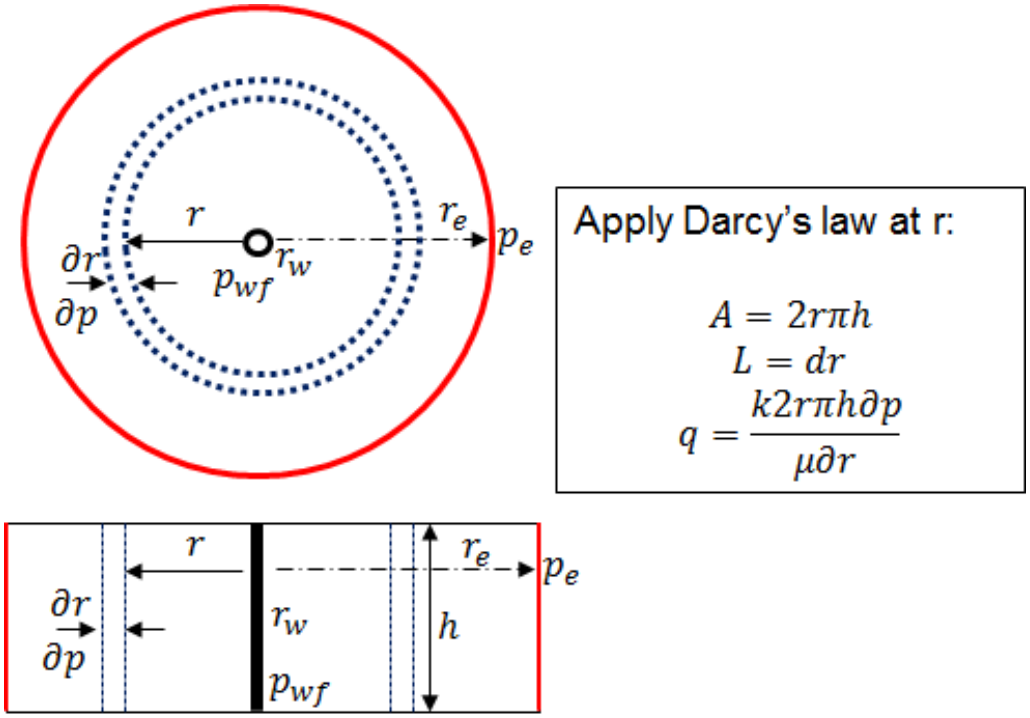

Figure 3.5: Radial flow and reservoir outer boundary. After Whittle (2017).

The diffusivity equation can be solved for different outer boundary conditions. The three most common conditions are

(i). *Transient State* (also called *Infinite Acting Reservoir Flow*) occurs because the reservoir appears infinite acting because the pressure disturbance has not reached the outer boundary. The transient state occurs within the radius of investigation r in Figure 3.5. The reservoir pressure declines non-uniformly throughout the reservoir and the rate at which the pressure

changes varies with time. This PhD work relates mainly to the analysis of this state during well-testing. For this reason, further details of the well-test analysis technique for this state, including the various flow regimes will be highlighted later in this section.

(ii). *Pseudo-Steady State* (*PSS*) occurs at late time when the reservoir is finite, i.e. the pressure front has the reached the reservoir boundary, and there is no pressure support, i.e. the model boundaries are no-flow boundaries (r_e and p_e in Figure 3.5). Thus, the pressure decreases at a constant rate with time throughout the reservoir. Examples for such reservoir boundaries are sealing faults and production from nearby wells.

(iii). *Steady State* occurs at late time when there is enough reservoir energy at the reservoir boundary such that a constant pressure boundary exists. The reservoir is considered finite and flow across the outer boundary (r_e and p_e in Figure 3.5) equals the production rate at the well. Hence, there is no pressure change throughout the reservoir. Examples for such reservoir boundaries include the support from an aquifer or the expansion of a gas cap.

Each of these boundary conditions give rise to very specific pressure transients that can be calculated from the analytical solutions of the diffusivity equation for the given boundary condition. In the following, the solutions to the transient state will be discussed as they are most pertinent for this study.

Solution to Infinite Acting Reservoir Flow

The solution of an infinite acting reservoir flow for pressure measured at the producing well is given as

$$p_D = \frac{1}{2}(c_3 \log t_D + 0.80907) + S. \tag{3.11}$$

where c_3 denotes unit conversion coefficient from ln to log and is given as 2.302585. S denotes skin factor, which account for the additional pressure drop when fluid flows into a producing well. From Equation 3.5 and 3.11, the pressure change at the well can be computed as

$$\Delta p = \frac{\Delta q \beta \mu}{2 c_2 k_m h}(c_3 \log \Delta t + c_3 \log \frac{c_1 k_m}{\phi \mu C_t r_w^2} + 0.80907) + 2S. \tag{3.12}$$

Well-test analysis is carried out by plotting the changes in pressure as a function of time on different plot types (e.g. semi-log, log-log and other specialised

plots). Of these plots, the log-log plot offers the most diagnostic insights and is hence used in this study. It allows the identification of different flow regimes. To generate the log-log plot, Equation 3.4 and 3.5 can be rewritten as

$$\log t_D = \log \frac{c_1 k_m \Delta t}{\phi \mu C_t r_w^2} = \log \Delta t + \log \frac{c_1 k_m}{\phi \mu C_t r_w^2}, \tag{3.13}$$

$$\log p_D = \log \frac{c_2 k_m h \Delta p}{q \beta \mu} = \log \Delta p + \log \frac{c_2 k_m h}{q \beta \mu}. \tag{3.14}$$

The diagnostic feature of the log-log plot is the pressure derivative $\Delta p^{'}$ curve through which distinct flow patterns corresponding to different geological features can be recognised. The calculation of the pressure derivative is given by

$$\Delta p' = \frac{d\Delta p}{d \ln \Delta t} = \Delta t \frac{d\Delta p}{d\Delta t}. \tag{3.15}$$

The conventional flow regimes using the derivatives and the corresponding derivative slopes are presented in Figure 3.6 and Table 3.2 respectively. The pressure derivative is used to correlate the pressure transient data to the known geological features in the geoenegineering workflow.

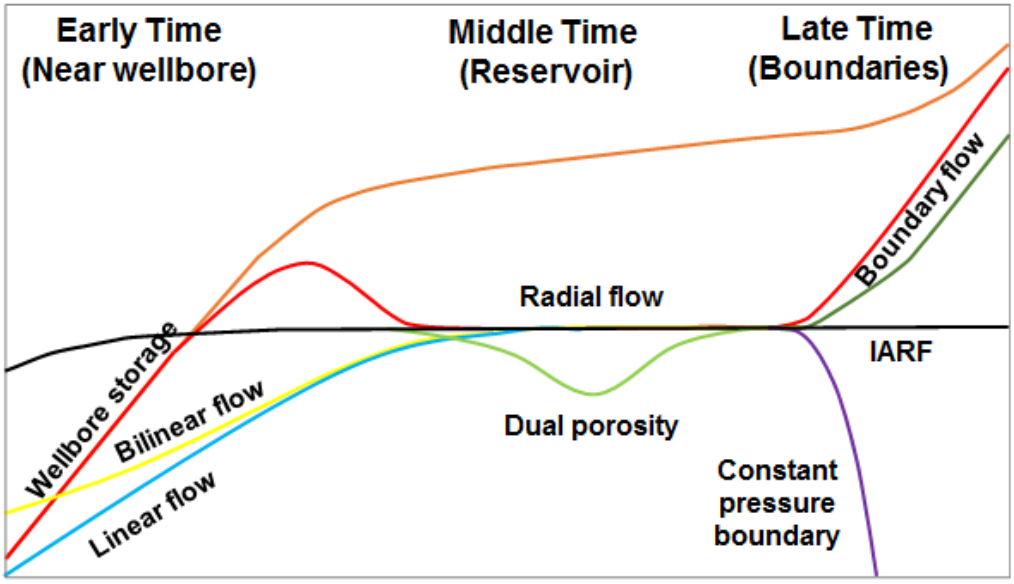

Figure 3.6: Log-log plot with conventional flow regimes. After Fekete.com (2015).

Flow Regime	$\Delta p'$
Wellbore storage or boundary-dominated (PSS)	1
Bilinear flow	1/4
Linear flow or channel	1/2
Spherical flow	-1/2
Radial or pseudo-radial flow	0

Table 3.2: Flow regime and slope of pressure derivative .

3.3 MODEL VALIDATION

A number of initial studies were conducted to validate the accuracy of the unstructured DFM simulations, and to make sure that the pressure transient response from the reservoir reflects the physical conditions and are not impacted by numerical artefacts. For this model validation, we ran simulations considering a matrix-only model (Table 3.3, Model 1 and Figure 3.7), a model with a single fracture (Table 3.3, Model 2) and a model with multiple intersecting ("multi-wing") fractures (Table 3.3, Model 3). In these models, the well is located centrally and symmetrically in the single fracture, and at a bifurcation point for multi-wing fractures, respectively (Figure 3.8a and Figure 3.9a). Analytical solutions exist for all these models such that simulation results can be compared to the exact solutions.

Model name	**Well Location**	**Model description and dimension**
Model 1: Matrix only	matrix	$200X200X1m$ homogeneous matrix
Model 2: Single fracture	fracture	$200X200X1m$ homogeneous matrix model with two-wing (single) fracture and F_{CD} of 1-500
Model 3: Multiple fracture intersection (multi-wing) fracture	fracture	$200X200X1m$ homogeneous matrix model with six-wing (multiple) fractures and asymmetric factor and F_{CD} of 10

Table 3.3: Simulation models to validate the DFM simulations.

The reservoir and fluid properties used for the sensitivity study are summarised in Table 3.4. For simplicity, all simulations assume single-phase laminar flow, no gravity effects, a homogenous and isotropic reservoir matrix with uniform thickness, fracture network with single porosity and permeability for a given simulation model. We also assume layer bound vertical fractures and hence represent the model with the third dimension as a single layer. Wells are

oriented vertically and fully penetrate the formation and produce at constant rate for any given simulation.

Reservoir initial pressure, p_0 (psi)	4351
Normalised rate, q (bbl/day)	6.29
Matrix porosity, ϕ_m $(fraction)$	0.3
Matrix permeability, k_m (mD)	10
Fracture porosity, ϕ_f $(fraction)$	1.0
Oil viscosity, μ_o (cp)	1.0
Oil density, ρ_o $(kg/m3)$	700
Oil formation volume factor, rb/stb	1.0
Total compressibility (psi^{-1})	$6.8948X10^{-6}$

Table 3.4: Reservoir model and fluid properties used in the validation study.

In all simulation models, a jacket of matrix cells with uniform properties is added to prevent flow in the fractures from interacting with the model boundary (Aljuboori et al., 2015; Egya et al., 2018c). Since the fracture cells are characterised with a high permeability, the pressure response in this medium can propagate very quickly to the model boundary even before the effect of exchange between fractures and the matrix has started. Therefore, it is necessary to prevent the late time boundary effect from interfering with the middle time pressure transient response in our simulations.

The first set of results is for the matrix-only model with a well located at the centre of the reservoir (Figure 3.7). Each of the graphs in Figure 3.7 shows the main flow regimes, i.e. early time wellbore storage (WBS) or afterflow (for a shut-in well) with slope $m = 1$, radial flow with $m = 0$, and late-time PSS flow with $m = 1$ indicating a closed boundary. During the WBS, the production at the surface is due to the expansion of the fluid column in the well (Bourdet, 2002). The total production at this time is from the well storage with negligible contribution from the reservoir. When the storage is depleting, the reservoir production starts and increases until the total surface production equals the reservoir contribution to the well. The period between the start of reservoir production at the sand face to the beginning of the total production from the reservoir marks the transition from the pure wellbore effect with $m = 1$ to radial flow with $m = 0$. During the radial flow, the reservoir flow-lines converge at the well in a radial geometry and the radius of the circular drainage area increases with time. Changes to this flow behaviour only occur with changes in reservoir properties or when pressure disturbance reaches the boundary. The reservoir starts to deplete when the pressure front reaches a closed boundary. During this time the reservoir pressure declines constantly with time throughout the reservoir. The pressure

changes during this period, called pseudo-steady state, for an homogeneous matrix with closed boundary is marked by another $m = 1$ slope.

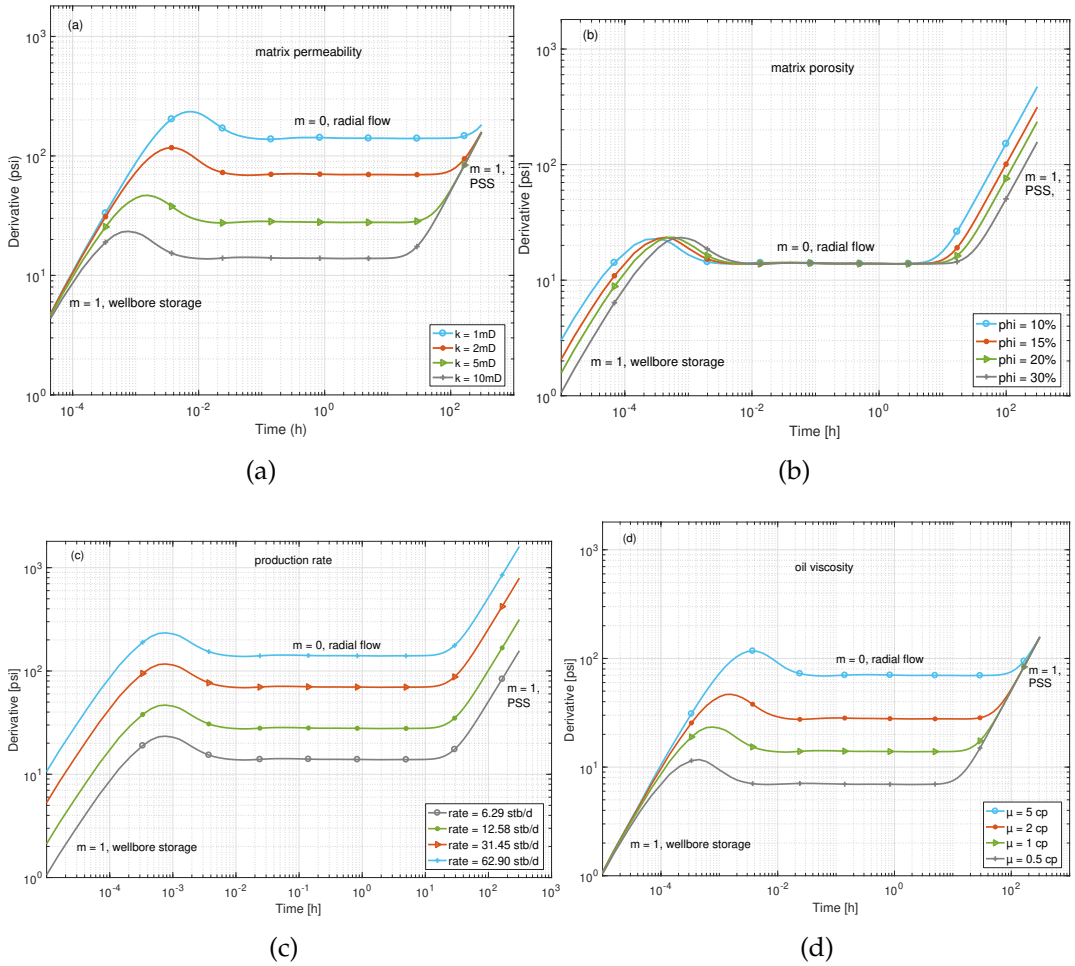

Figure 3.7: Simulation results for a matrix-only model, with normalised rate of 6.29 stb/-day, showing sensitivities to matrix permeability (a), matrix porosity (b), production rate (c), and oil viscosity (d).

The simulated pressure derivatives in Figure 3.7 capture the sensitivities to changes in reservoir parameters discussed in Houze et al. (2017). Figure 3.7a shows little variation in the form for pressure derivatives as a function of permeability. However, the pressure response at higher matrix permeabilities deviates from pure WBS at early times, indicating the reservoir's ability to react faster to production as expected. Changes in porosity (Figure 3.7b) do not show changes in the stabilization of the pressure derivative (i.e. during radial flow). Deviations are observed, however, during transition from pure WBS to radial flow, and from radial flow to PSS. Given the same reservoir size and properties, changes in time are proportional to the changes in porosity for the PSS influence to reach the well. Figure 3.7c shows that with changes in production rate, the derivative shifts vertically but the form of the pressure derivative remains the same. High flow rates produce proportionately higher pressure deviations from the initial pressure, shifting the derivative upwards. The effects of changes in viscosity on

pressure derivative are opposite to those described above for the changes in permeability (Figure 3.7a).

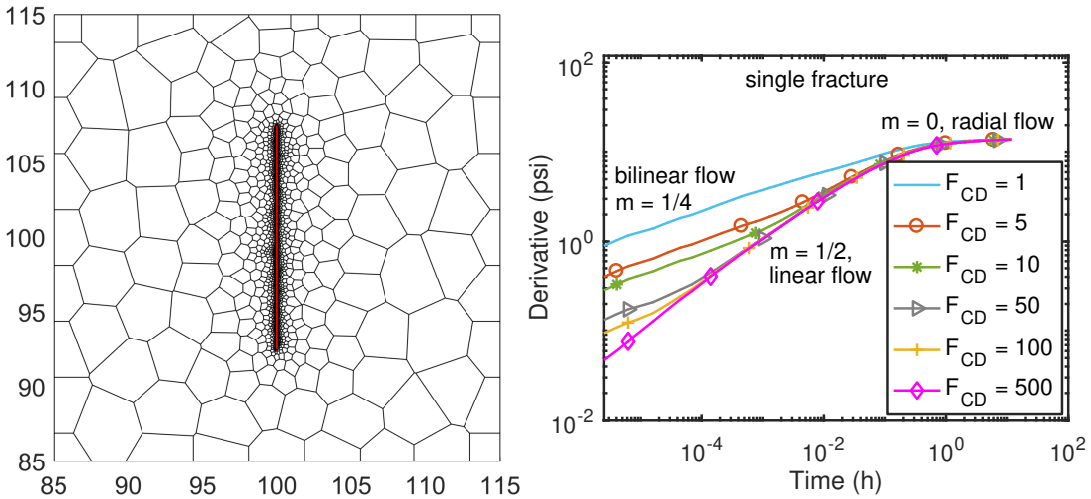

(a) (b)

Figure 3.8: Single fracture model showing the close-up of the unstructured PEBI grid with refinement around a single fracture in metres (a) and simulation results for variable fracture conductivities (F_{CD} of $4 - 4500$) (b). F_{CD} denotes the dimensionless fracture conductivity, as defined in Equation 3.7.

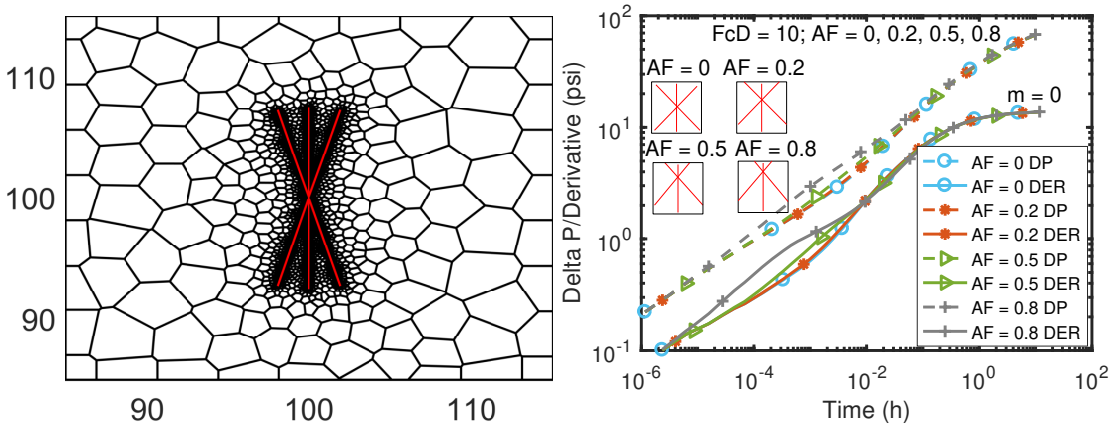

(a) (b)

Figure 3.9: Multiwing fractures model showing the close-up of the unstructured PEBI grid with refinement around the multiwing fractures (a) and simulation results for F_{CD} values of 10 and AF values of 0-0.8 (b). The dashed lines and solid lines show changes in pressure and the corresponding pressure derivatives, respectively. The asymmetry factor, AF, measures the well offset from the centre of the fracture.

Next, we perform a sensitivity analysis using a reservoir model with a single fracture such that our simulated pressure transients can be compared with existing analytical solutions. Results showing a close-up of the unstructured PEBI grid with refinement around a single fracture intersected by a well are depicted in Figure 3.8. From top to bottom in Figure 3.8b, the flow regimes identified with

changes in the conductivity include bilinear flow with $m = 1/4$, linear flow with $m = 1/2$, and pseudo-radial flow with $m = 0$. For low conductivity fractures, pressure gradient along the fracture length is not insignificant. For this reason series of linear flow emerge because of pressure drop along the fracture length as fluid flow towards the intersecting well. A second linear flow regime emerge as the reservoir from the surrounding matrix into the fracture extension before the flow within the fracture reaches the two ends of the fracture. During this period, the pressure response is referred to as the bilinear flow regime with a characteristic derivative slope of $m = 1/4$ (Cinco L. et al., 1978; Bourdet, 2002). When the fracture permeability if high, the pressure drop within the fracture does not occur. Thus, the early time is characterised with linear flow perpendicular to the fracture plane. This period of pressure transient is called linear flow regime and is characterised with the derivative slope of $m = 1/2$ (Gringarten et al., 1974; Bourdet, 2002). After this period, significant recharge from the reservoir area around the fracture ends also occurs leading to a radial geometric flow around the well. This later period is termed the pseudo-radial flow regimes characterised by the derivative slope of $m = 0$. Other descriptions of the pressure responses of single fracture models under different flow conditions are provided later in Chapters 4 and 5. In addition, Figure 3.9a shows a close-up of the unstructured PEBI grid with refinement around multi-wing fractures used to further validate our simulations. The results (Figure 3.9b) showing changes in pressure and the corresponding pressure derivatives for different values of asymmetry factors (AF) indicate similar responses to the analytical and semi-analytical solutions of Berumen et al. (2000) and Wanjing and Changfu (2014). AF measures the well offset from the centre of the fracture.

Reservoir Parameter	**Model Input**	**Analysis Estimate**
Matrix permeability (mD)	1	0.98
	2	1.99
	5	4.99
	10	9.90
Fracture X_f (metres)	7.5	7.46
	10	9.95
	15	14.94
	20	19.66

Table 3.5: Comparison between model input and estimated results from analysis.

Table 3.5 shows quantitative comparison of the reservoir properties input in the simulation models and the values of the same parameters estimated from the pressure transient analysis. All the above simulation results were also vali-

dated using the commercial software CMG IMEX for simple orthogonal fracture patterns. The validation models further provide references for the interpretation of the more complex fracture geometries simulated later.

3.4 JANDAIRA CARBONATE FORMATION FRACTURE PATTERNS

The geoengineering workflow is applied to an outcrop containing well-developed fracture patterns in carbonate lithologies (Figure 3.10). The outcrop is located in the Turonian-Campanian Jandaira formation, which crops out in large parts of the Potiguar basin in NE Brazil (Bertotti et al., 2017; de Graaf et al., 2017). The Jandaira formation is a sub-horizontal formation, dipping on average 3° towards the North, creating exposed pavements with dimensions exceeding several hundred meters. These exposures are ideal for multiscale fracture network characterisation. Using satellite imagery in combination with drone images and conventional outcrop measurements, more than 18,000 fractures have been mapped in pavements throughout the basin (Bisdom et al., 2017a).

Although layers with folds and faults are relatively rare, the Jandaira formation is intensely fractured. Based on crosscutting relations between vertical fractures and burial-related horizontal stylolites and the abundance of bed-perpendicular conjugate sets of fractures, most of the fractures are interpreted to have formed at shallow depths during a relatively early phase of burial (Bertotti et al., 2017). Outcrop and thin section analyses of fracture infill shows that fractures have shear and opening components, indicating that these are hybrid fractures (Ramsey and Chester, 2004; Bertotti et al., 2017). The main driving mechanism for fracturing was regional shortening, under a maximum horizontal stress oriented N-S to NE-SW (Bertotti et al., 2017; de Graaf et al., 2017). As a result, most fractures are oriented N-S and NW-SE, dipping perpendicular to bedding (Bisdom et al., 2017a).

The E-W striking fractures are barren features in the outcrops, but prior to exhumation these features were tectonic (i.e., bed-perpendicular) stylolites formed in the same N-S to NW-SE regional shortening phase as the fractures (Bertotti et al., 2017). Fractures from different orientation families are observed to be mutually crosscutting, providing further evidence for their simultaneous formation. The only hierarchy that is observed in some outcrops is related to fracture size, as smaller fractures terminate against larger fractures.

These burial-related fractures are present at high densities throughout the entire basin, even though there is only limited seismic-scale deformation. These patterns have furthermore been formed under relatively low stresses. Many carbonate reservoirs have a similar lack of seismic-scale deformation, where conventional methods such as curvature analysis do not indicate significant fracturing,

but the studies of the Jandaira formation show that high-density fracture patterns may still exist. For this type of fracture networks, there is significant value in having the ability to identify fracture flow from well-test data.

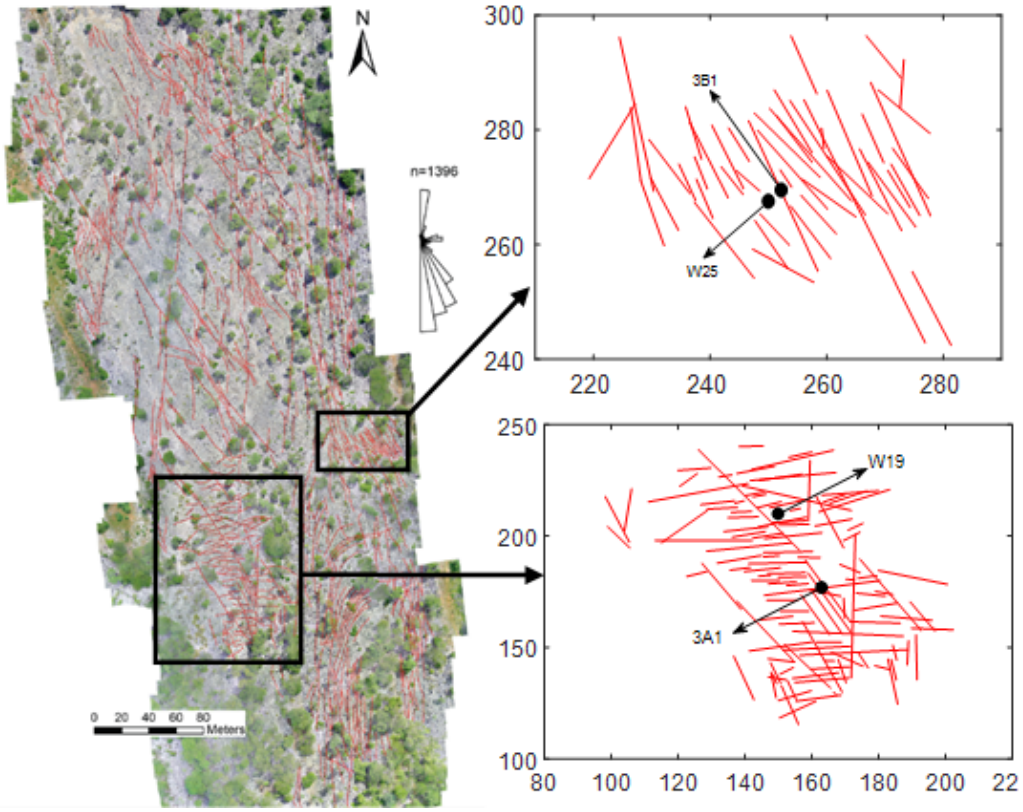

Figure 3.10: Aerial view of the fracture patterns in the Jandaira Formation, Brazil (left) (Bisdom et al., 2016). The marked inset boxes indicate how subset-model fractures are taken. The upper inset represents a disconnected fracture network and the lower inset is for connected fracture network.

Fractures from one of the Jandaira pavements are used in this study (Figure 3.10). This $400X175m$ pavement has been imaged using a drone, resulting in a georeferenced image from which nearly 2000 fractures were mapped using GIS software (Bisdom et al., 2017b). Fracture lengths in this pavement range from $0.68m$ to about $90m$ with apertures observed at the outcrop ranging from $< 0.1mm$ up to $10mm$ (Bisdom et al., 2016). Bertotti et al. (2014) noted that even though the orientation of the structures is preserved, fracture apertures observed in the outcrop are probably not representative of the subsurface conditions and hence we consider variable fracture apertures in Chapters 4. Like the Jandaira Formation, recent karstification has altered the fracture/joint properties at surface of the outcrop example shown in Figure 1.1. For this reason, subsurface model parameters are selected in this thesis - rather than being measured in the field - with the contrast between matrix and fracture permeability being the important consideration.

4

DUAL-POROSITY RESPONSES FOR FRACTURES WITH UNIFORM CONDUCTIVITY

4.1 INTRODUCTION

Geological reservoirs can be extensively fractured but the observed well-test signatures may not show a pressure transient response that is classically (or wrongly) considered to be representative of NFR: for example, the classical dual-porosity response (V-shape, see Chapter 1) that indicates two distinct pore systems (i.e. the mobile fractures and immobile matrix). Yet, the production behaviour may still be influenced by these fractures. On the other hand, even moderately and discretely fractured reservoirs can yield the dual-porosity V-shape under certain reservoir conditions.

This chapter uses the geological well-testing method introduced in Chapter 3 to explore the validity and limitations of the characteristic flow behaviour inherent to the dual-porosity model when interpreting well-test data from Type 2 and 3 NFR of Nelson's classification (Figure 1.2). To achieve this, the geoengineering workflow is applied to generate synthetic pressure transient data in both idealized fracture geometries and real fracture networks mapped in an outcrop of the Jandaira Formation (Figure 3.10). The chapter also presents key reservoir features that cause the classic V-shape pressure derivative (lookalike) response in NFRs. These include effects of fracture skin, a very tight matrix permeability and wells intersecting a minor, unconnected fracture close to a large fracture or fracture network. The findings apply to both connected and disconnected fracture networks.

4.2 SINGLE FRACTURE MODEL

Our simulation and interpretation of well-test signals in an NFR starts with a reservoir model containing a single natural fracture that intersects the well (Figure 3.8) as well as a single fracture located in the matrix at different distances to the well (Figure 4.1). Although such a model is unrealistic for a real reservoir

condition, it allows us to apply analytical solutions (Cinco-Ley and Samaniego-V., 1981; Bourdet, 2002; Kuchuk and Biryukov, 2015) and provides an important reference when interpreting pressure transient behaviour for complex cases.

These reference simulations show the well-studied flow regimes for different fracture conductivities and locations of the well with respect to the fracture. For example, for a well intersecting fracture with low fracture conductivity (up to F_{CD} = 100), the first flow regime observed in the pressure derivative is bilinear flow (Figure 3.8). As fracture conductivity increases to F_{CD} = 500 (Figure 3.8), the bilinear flow diminishes and linear flow emerges as the first flow regime before radial flow is attained (Gringarten et al., 1974, 1975; Cinco-Ley and Samaniego-V., 1981; Wong et al., 1986; Bourdet, 2002). This is not the case for the same reservoir and fracture properties where the well is located in the matrix (Figure 4.1). It is well-understood that a well located near a single fracture first shows the effect of wellbore storage followed by radial flow in the matrix (depending on the distance on the nearby fracture) and then a minimum ("dip") on the derivative reflecting the period of depletion from the fracture (Cinco-Ley, 1996; Abbaszadeh and Cinco-Ley, 1995).

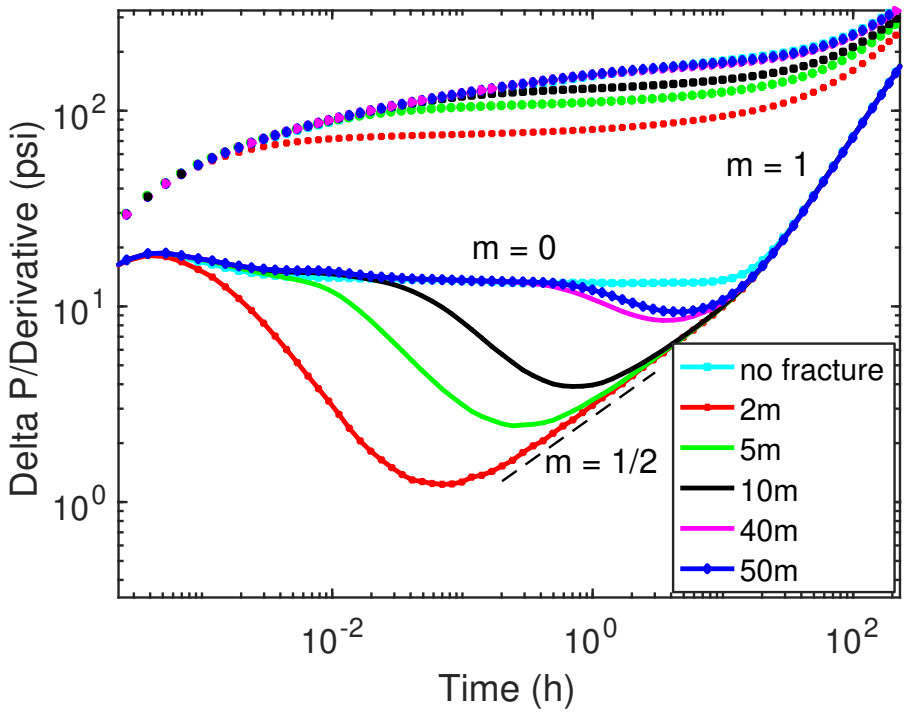

Figure 4.1: Simulated pressure response for a well located at different distances to an infinite conductivity single natural fracture with fracture half-length X_f = 15m. m indicates the slope of the pressure derivative. Note that m = 0 indicates radial flow or pseudo-radial flow, m = 1/2 indicates formation linear flow and m = 1 indicates pseudo-steady state boundary flow.

Field examples of pressure responses for a high permeability object in form of fractures, fault or karst some distance away from the well include heavily faulted carbonate reservoir in Gulf of Campeche (Abbaszadeh and Cinco-Ley,

1995), Nonintersecting fracture in the Arab D reservoir (Al-Thawad et al., 2001), Xinchang X2 gas field (Deng et al., 2018). Other simulation results of a well located in the matrix adjacent to fractures are presented later in Figures 4.2 to 4.6.

4.3 CONNECTED AND DISCONNECTED FRACTURE NETWORKS

4.3.1 *Synthetic Fracture Networks*

Model name	Well Location	Model description and dimension
Model 4a: Idealised connected fractures network	fracture	$4kmX4kmX1m$ homogeneous matrix model with idealised connected fracture network. F_{CD} of 0.1 to 10000.
Model 4b: Idealised connected fractures network	matrix	$4kmX4kmX1m$ homogeneous matrix model with idealised connected fracture network. F_{CD} of 0.1 to 10000.
Model 5a: Idealised disconnected fractures network	fracture	$4kmX4kmX1m$ homogeneous matrix model with idealised disconnected fracture network. F_{CD} of 0.1 to 1000.
Model 5b: Idealised disconnected fractures network	matrix	$4kmX4kmX1m$ homogeneous matrix model with idealised disconnected fracture network. F_{CD} of 0.1 to 1000.
Model 6a: Outcrop example of connected fractures network	fracture	$550mX550mX1m$ homogeneous matrix subset-model with realistic outcrop connected fracture patterns. F_{CD} of 0.1 to 10.
Model 6b: Outcrop example of connected fractures network	matrix	$550mX550mX1m$ homogeneous matrix subset-model with realistic outcrop connected fracture patterns. F_{CD} of 0.1 to 10.
Model 7a: Outcrop example of disconnected fractures network	fracture	$480mX450mX1m$ homogeneous matrix subset-model with realistic outcrop disconnected fracture patterns. F_{CD} of 0.1 to 10.
Model 7b: Outcrop example of disconnected fractures network	matrix	$480mX450mX1m$ homogeneous matrix subset-model with realistic outcrop disconnected fracture patterns. F_{CD} of 0.1 to 10.
Model 8: Idealised connected fractures network with small fractures	fracture	$4kmX4kmX1m$ homogeneous matrix model with idealised connected fracture network and (un)connected small fractures. F_{CD} of 1000.
Model 9: Idealised disconnected fractures network with small fractures	fracture	$4kmX4kmX1m$ homogeneous matrix model with idealised disconnected fracture network and (un)connected small fractures. F_{CD} of 1000.
Model 10: Idealised disconnected fractures network with increasing small fracture	fracture	$4kmX4kmX1m$ homogeneous matrix model with idealised disconnected fracture network and different lengths of unconnected small fracture. F_{CD} of 1000.

Table 4.1: Summary of simulation models with grid dimensions and well locations.

In order to assess the validity and limitations of the Warren and Root (1963) dual-porosity model in the interpretation of NFR, we first simulate a number of models containing an idealised and regular fracture network (Figure 4.2). We consider two different scenarios (Table 4.1, Model 4 and 5): A connected fracture model (Figure 4.2a) that consists of uniform rectangular parallelepipeds ($20mX20mX1m$) of matrix blocks that are separated by two sets of perfectly orthogonal fractures. Secondly, we consider a disconnected fracture model (Figure 4.2b) that has the same properties as the connected model except that it contains only a single set of parallel fractures. In each of these models, we consider both, a well intersecting fracture(s) (Table 4.1, Model 4a and 5a) and a well located in the matrix (Table 4.1, Model 4b and 5b). In all cases, the well is located in the centre of the model or slightly offset from the centre (Figure 4.2), if the well is not intersecting a fracture. We consider fracture conductivities from $60mD.m$ to

$6X10^6 mD.m$, which yield dimensionless fracture conductivities of 0.1 to 10000. Table 4.1 contains further descriptions of the simulation models used here.

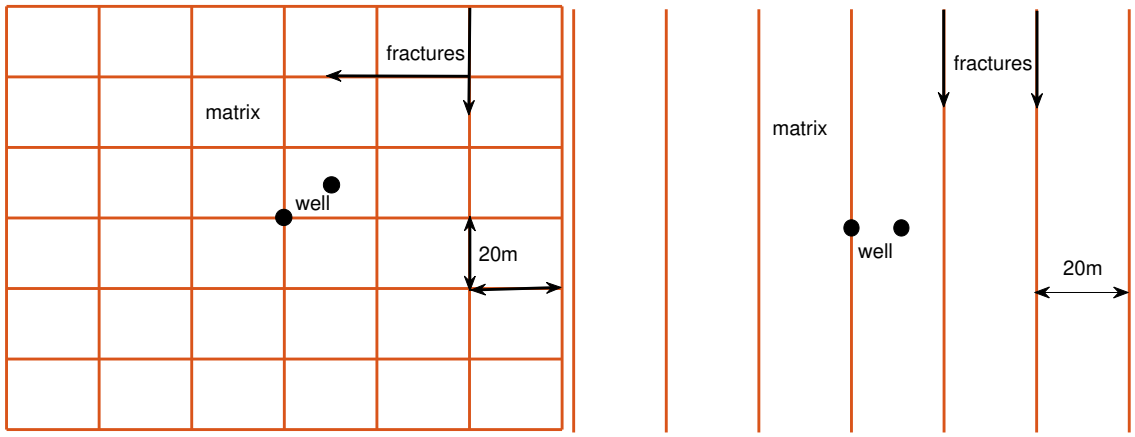

(a) Model 4 (b) Model 5

Figure 4.2: Idealised fracture network with a $60m$ half-length showing a connected fracture network with a well intersecting fractures or a well located in the matrix adjacent to fractures (a); and a disconnected fracture network with identical well configurations (b).

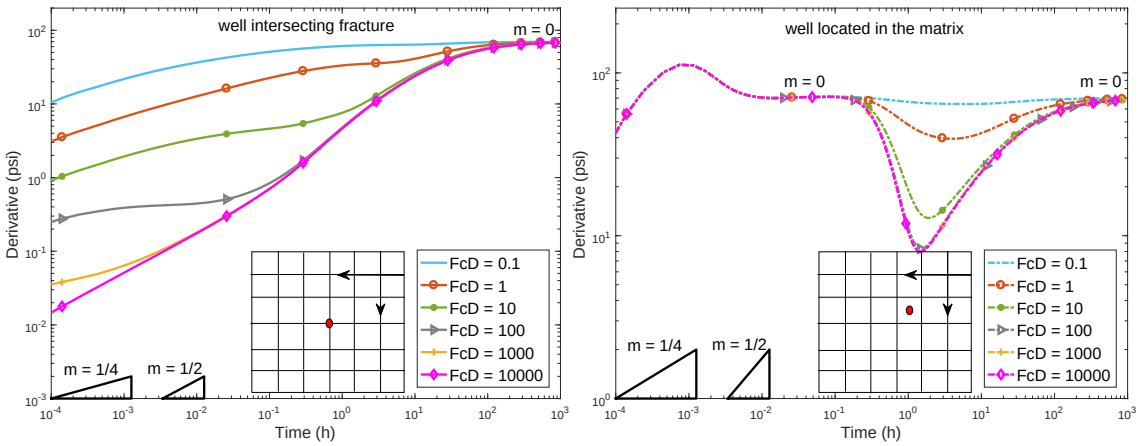

(a) (b)

Figure 4.3: Simulated pressure derivatives of an idealised connected fracture network that resembles the classical Warren and Root (1963) dual-porosity model in $2D$. Well intersecting fractures (a) and a well located in the matrix adjacent to fractures (b). m indicates the slope of the pressure derivative.

Figure 4.3 shows the resulting pressure derivatives for the connected fracture network. For the situation where a well intersects fractures (Figure 4.3a), the bilinear fracture flow regime ($m = 1/4$) is observed at early time in situations where the fracture conductivity is low ($F_{CD} = 0.1$ to 1). The bilinear flow occur due to flow in series within the fracture caused by pressure gradient as well as flow perpendicular to fracture planes. This regime then transitions through different periods until it reaches pseudo-radial flow when equilibrium between

matrix and fracture flow is reached. However, surprisingly as fracture conductivity increases ($F_{CD} > 10$), the typical V-shape (or "dual-porosity dip") signature cannot be observed. The presence of well-connected fractures only produces a slanted S-shaped derivative profile (Figure 4.3a). The earlier time prior to the system pseudo-radial flow indicate local linear flow into fractures from adjacent matrix and this flow is can be linked to connected, high conductivity natural fractures. Field examples where flow in NFR is observed to be associated with linear flow (rather than V-shape) followed by a transition to pseudo-radial flow include Ekofisk naturally fractured chalk field (Snow and Brownlee, 1989), giant Tengiz field in Kazakstan, slanted well intersecting a natural fracture in Ghawar field presented by Al-Thawad et al. (2001). The slanted S-shape pressure derivative for connected natural fracture networks is also similar to the apparent radial composite derivative fingerprint in Tarim Basin (Stewart, 2014).

In contrast, the typical V-shape can only be observed in models where the well is not intersecting any fractures (Figure 4.3b). Here, the pressure derivatives are characterised by two stabilisation periods where radial flow occurs separated by transition periods, which cause troughs in the derivative plots. Initially, until the first period of radial flow ($m = 0$) commences, the typical flow regimes are of a homogeneous reservoir with the well located in the matrix. Until this period, the depletion is only from the matrix without contribution from the fractures. This is followed by a transition period (V-shape) where the contribution from the fractures becomes significant and the matrix and fracture pressure reach equilibrium. Once the two media equilibrate, the second pseudo-radial flow ($m = 0$) is observed. For situations with very low fracture conductivity ($F_{CD} < 1$), the dual-porosity behaviour is apparent via a broader, U-shaped, drop in the derivative. If $F_{CD} > 10$, the V-shape is followed by a linear flow regime before the derivative increases rapidly as the stabilisation between the two systems is reached. The V-shape for a well located in the matrix, adjacent to fractures, can be associated to the effect of a high permeability object near a well as already discussed in Section 4.2.

Figure 4.4a shows the simulated pressure derivatives for the disconnected fracture network. For the case where the well is intersecting a fracture (Figure 4.4a), fractures with low conductivity ($F_{CD} < 100$), lead to a pressure derivative that indicates clear bilinear flow ($m = 1/4$) before a period of pseudo-radial flow emerges. With an increase in fracture conductivity ($F_{CD} = 500$) linear flow ($m = 1/2$) can be observed, followed by a bilinear flow regime and eventually pseudo-radial flow. From the slope of the linear flow regime, the fracture half-length can be estimated. In these cases, none of the pressure transients show a dual-porosity signature. However, if the well does not intersect any fractures (Figure 4.4b), the dual-porosity behaviour is in many ways similar to the con-

nected network shown in Figure 4.3b, independently of the fracture conductivity. Examples of NFR with pressure derivatives similar to the simulated pressure transients for a well intersecting a disconnected fracture network are fields with discretely fractured reservoir (Morton et al., 2012; Nogueira et al., 2013), Group 4 wells of Valhall Field presented by Rogers et al. (2007).

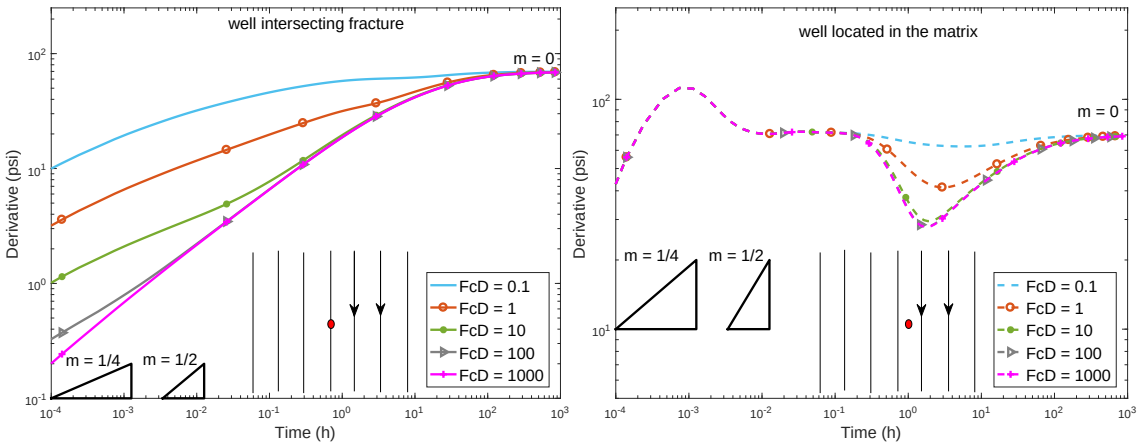

(a) (b)

Figure 4.4: Simulated pressure derivatives of an idealised disconnected fracture network with variable dimensionless fracture conductivities. Well intersecting fractures (a); and a well located in the matrix adjacent to fractures (b). The slope of the pressure derivative is indicated by m.

Results for both connected and disconnected fracture networks persented above, similar to (Wei et al., 1998; Morton et al., 2012; Kuchuk and Biryukov, 2012, 2014, 2015), counteract the pressure behaviour of Warren and Root dual-porosity model. Contrary to the claims of the dual-porosity model, the classical dual-porosity signature is not observed for a well intersecting fractures, i.e. the dual-porosity model conditions (iii) and (v) of Section 1.2. Furthermore, the lookalike V-shape was observed for a well near non-intersecting fractures - a condition that breaks the (Warren and Root, 1963) assumptions (ii) and (iv). Thus, the V-shape is not caused by dual-porosity systems as defined by Warren and Root (1963) because the assumptions of their model presented in Chapter 1 point out the paradox of what is observed in the results presented here. Since the appearance of the classical dual-porosity signature is based on the assumption that the flow in matrix is negligible, Middle East reservoirs (e.g. Ghawar Field, Saudi Arabia) with considerable matrix contribution to flow (Stewart, 2014) would not conform to the pressure response of the dual-porosity model. The pressure response for a well in the matrix as presented here is rather in agreement with the findings of (Abbaszadeh and Cinco-Ley, 1995; Cinco-Ley, 1996) for a reservoir with well in the matrix near a non-intersecting conductive fracture(s) or open faults.

4.3.2 *Realistic Outcrop Fracture Patterns*

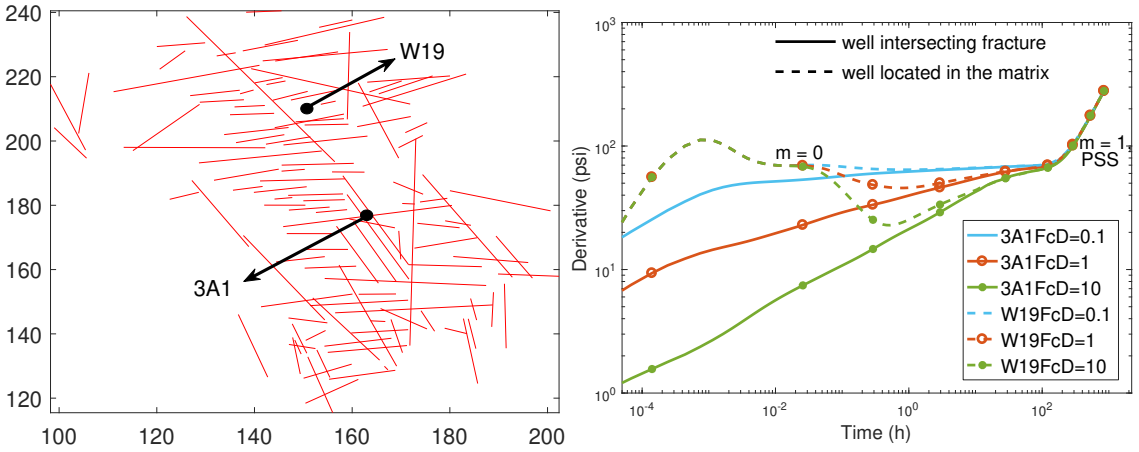

(a) (b)

Figure 4.5: Model of a connected fracture network located in the Jandaira Formation (Figure 3.10, lower inset). Fracture network with the locations of wells (the unit is in metres) (a) and simulated pressure derivatives (b). Solid lines represent simulations for a well intersecting fractures and dashed lines are for a well located in the matrix. The slope of the pressure derivative is indicated by m.

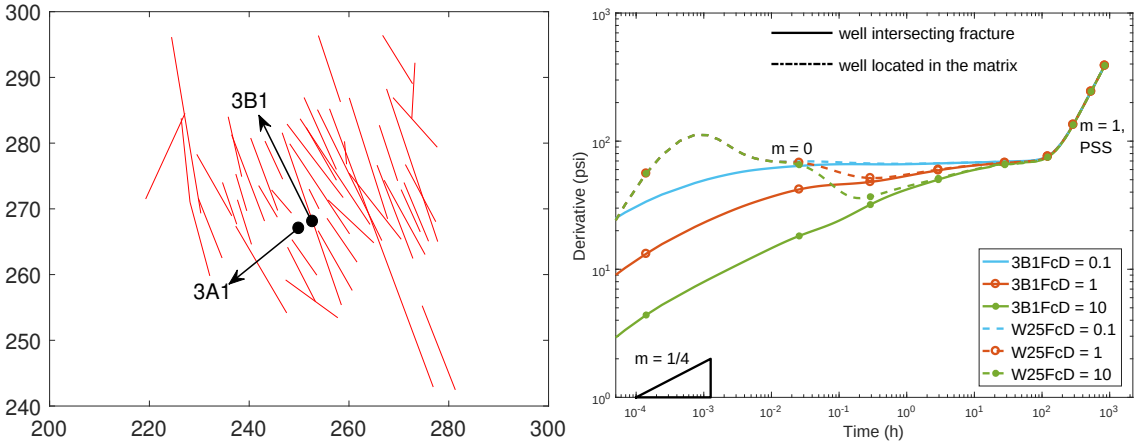

(a) (b)

Figure 4.6: Model of a disconnected fracture network located in the Jandaira Formation (Figure 3.10, upper inset). Fracture network with locations of wells (the unit is in metres) (a) and simulated pressure derivatives (b). Solid lines represent simulations for a well intersecting fractures and dashed lines are for a well located in the matrix.

With the insights gained from the simple orthogonal fracture geometries discussed above, we simulated the pressure transient behaviour for the natural fracture patterns observed in the Jandaira Formation (Figure 3.10). We identified locations with connected fracture patterns (Figure 3.10 lower inset. See further description in Table 4.1, Model 6a and b) and disconnected fracture patterns

(Figure 3.10 upper inset. See further description in Table 4.1, Model 7a and b) in the outcrop data and constructed models accordingly (Figure 4.5 and Figure 4.6). This allowed us to compare the pressure transient behaviour observed for the idealised fracture patterns to the transient behaviour in more realistic fracture patterns. As in the simulations depicted in Figure 4.3 and Figure 4.4, we ran simulations for wells intersecting a fracture and wells that are located in the matrix. Figure 4.5 and Figure 4.6 show that the pressure transients for the realistic, outcrop-based fracture networks are similar to those in the idealised fracture systems. Again, the dual-porosity signature is only apparent if the well is located in the matrix, not intersecting a fracture (as shown by the dashed lines in Figure 4.5b and Figure 4.6b).

A key observation is the counter-intuitive behaviour of the dual-porosity signal. It can only be observed if the well is located in the matrix, even in situations where the fractures are well connected. This is in direct contradiction to the underlying theory of the Warren and Root (1963) dual-porosity model. Previous studies (e.g., Cinco-Ley and Samaniego, 1977; Cinco-Ley et al., 1985; Gringarten, 1987; Bourdet, 2002) have discussed that the type of inter-porosity flow between the matrix and the fractures that is assumed in a computation impacts the presence or absence of the dual-porosity signature, depending upon if the well is intersected by fractures or not. The above studies classified dual-porosity solutions into restricted inter-porosity flow and unrestricted inter-porosity flow. The restricted inter-porosity flow solution relates the dual-porosity behaviour to the presence of a skin at the fracture surface (Cinco-Ley and Samaniego, 1977) and/or within fractures (Cinco-Ley and Samaniego-V., 1981), i.e., damage caused for example by presence of minerals, filter cake, or a polymer-invaded zone that restricts communication between the matrix and the fractures or within fractures. The presence of the inter-porosity skin causes the resulting pressure transient behaviour for a TIF model to show a dual-porosity V-shape similar to PSSIF (Valdes-perez et al., 2011). The unrestricted inter-porosity flow is the same as in the TIF model without taking any form of inter-porosity skin into account.

All the results presented so far relate to the unrestricted inter-porosity flow. This is because our model assumes simulation under TIF conditions and does not contain any inter-porosity skin that restricts flow within fractures or between matrix and fracture. No dual-porosity response is observed for a well intersecting fractures under TIF. To account for restricted inter-porosity flow (i.e., TIF with inter-porosity skin), we therefore have to modify the model and simulate a scenario where a well is intersecting fractures with fracture damage (skin). The

relationship between fracture skin and other reservoir properties is modelled after Cinco-Ley and Samaniego (1977), (see Figure 4.7) and defined as follows

$$s_f = \frac{\pi a_s}{2l_w}\left(\frac{k}{k_s} - 1\right). \tag{4.1}$$

where s_f, a_s and k_s denote fracture skin, width and permeability of skin zone respectively. Other parameters remain as previously defined. As before, we first explore the impact of fracture skin on the idealised connected and disconnected fracture networks before we proceed to model the more complex fracture geometries. The fracture skin was varied from 0 to 10 by assigning the corresponding value of the permeability of the skin zone.

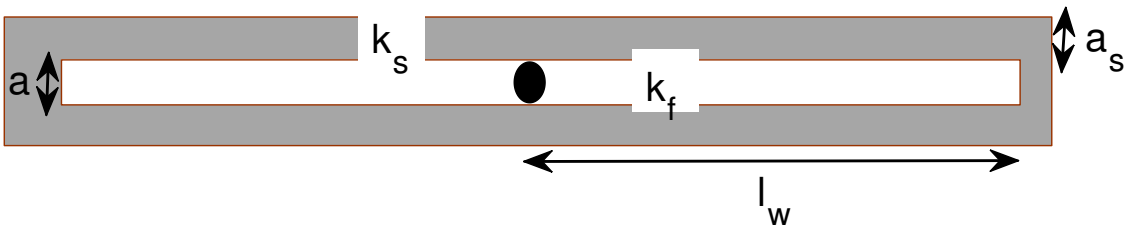

Figure 4.7: Diagram illustrating the fracture skin surrounding a single fracture penetrated by a well (black circle); the fracture has a half-length l_w. Where a, k_f, a_s and k_s denote the fracture aperture, fracture permeability, damage (skin) zone aperture and skin zone permeability, respectively.

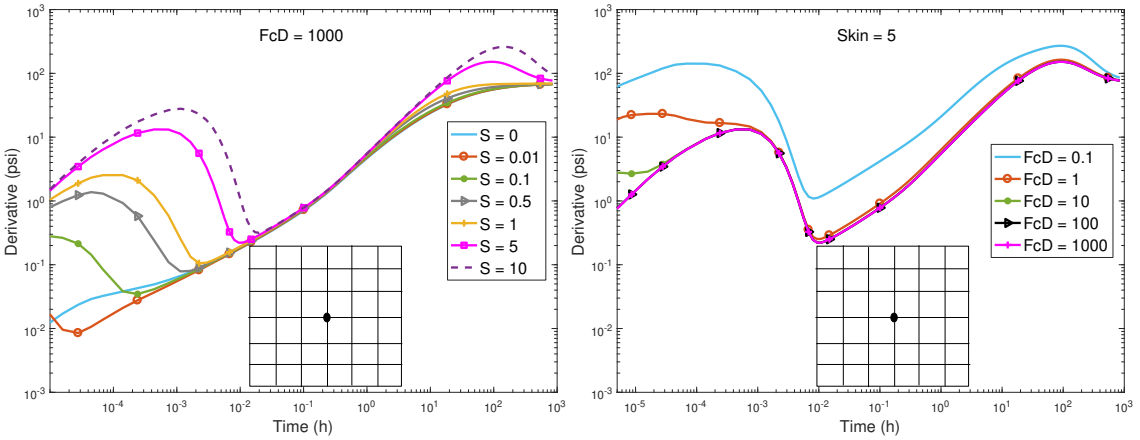

(a) (b)

Figure 4.8: Simulated pressure derivatives of a well intersecting fractures in an idealised connected fracture network with variable fracture skin and constant F_{CD} of 1000 (a) and constant skin of 5 with variable fracture conductivities (b).

Figure 4.8 and Figure 4.9 show the effect of fracture skin for the connected and disconnected fracture networks, respectively. A key observation is that higher positive fracture skin, i.e. more fracture damage, leads to more obvious dual-porosity responses. This behaviour is particularly prominent for high fracture

skin ($S \geq 5$) that locally restricts flow between fracture and matrix, although the permeability contrast between the fractures and matrix remains very low. It is clear that the dual-porosity signature is a result of the skin effect, i.e. the restricted inter-porosity flow, rather than an effect of the well located in the fractures. Under this flow condition, the initial depletion from a fractured reservoir with skin emanates only from the fracture system; the discharge from the surrounding matrix is choked because of the reduction in permeability between the fractures and the matrix. This condition could allow flow from the fractures to stabilise; the transition period then only follows after the flow from the matrix overcomes the barrier created by fracture skin.

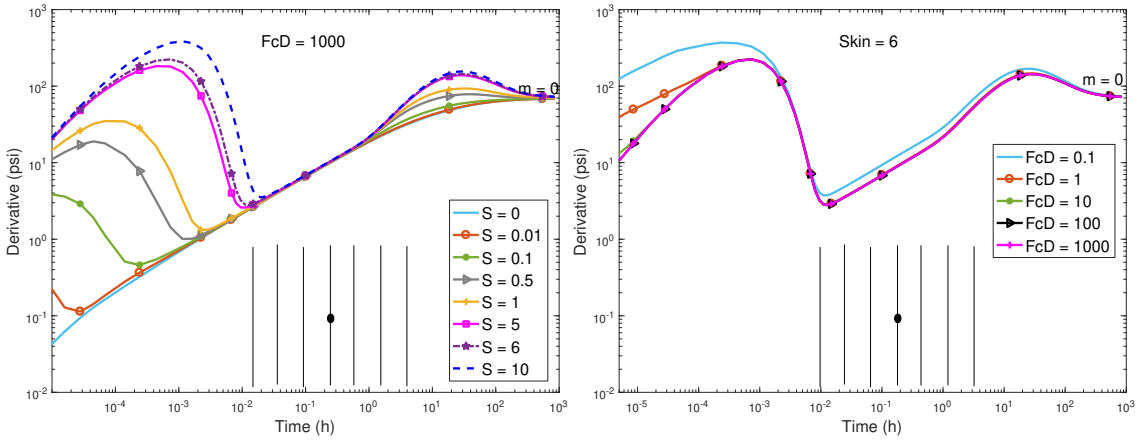

(a) (b)

Figure 4.9: Simulated pressure derivatives of a well intersecting fractures in an idealised disconnected fracture network with variable fracture skin and constant F_{CD} of 1000 (a) and constant skin of 5 with variable fracture conductivities (b).

4.4 EFFECT OF MATRIX PERMEABILITY AND BLOCK SIZE

The fact that restricted inter-porosity flow can cause a clear dual-porosity signature raises the question if unrestricted inter-porosity flow could also show a dual-porosity signature if the matrix permeability is reduced. To test this, we keep the fracture permeability constant and successively reduce the matrix permeability, rather than changing F_{CD} by keeping the matrix permeability constant and changing the fracture permeability. This still results in the same F_{CD} values, but there will be less flow in the matrix; this configuration is in agreement with one of the key assumption in the Warren and Root (1963) model, which only considers situations where flow within the matrix is negligibly small.

Figure 4.10 show the pressure transients for the idealised fracture networks with decreasing matrix permeability. In both, the connected network (Figure 4.10a) and disconnected network (Figure 4.10b), the dual-porosity signature becomes more prominent with decreasing matrix permeability. The reason for this

response is similar to the restricted inter-porosity flow (Figure 4.8 and Figure 4.9) in that the fluid exchange between fracture and matrix is reduced. However, since there is no fracture skin, the flow behaviour still falls into the category of unrestricted inter-porosity flow. There are two important observations. Firstly, the matrix permeability must be below $0.1mD$ (Figure 4.10) for the dual-porosity signature to be clearly visible, i.e. it is likely to occur more frequently in tight or unconventional reservoirs if there is no fracture damage. Secondly, the dual-porosity signature occurs at early time during our simulations and hence may not always be captured in the field data. Figure 4.11 show that even if the matrix block size increases from $20m$ (base case) to $160m$; the dual-porosity V-shape is only visible within the first second of the well test and hence would not be detectable in a real field. Larger matrix blocks (and increased fracture lengths) delay the onset of the dual-porosity signature relative to the base case because the fracture volume is increased and it takes slightly longer to deplete the fractures before the matrix recharge starts.

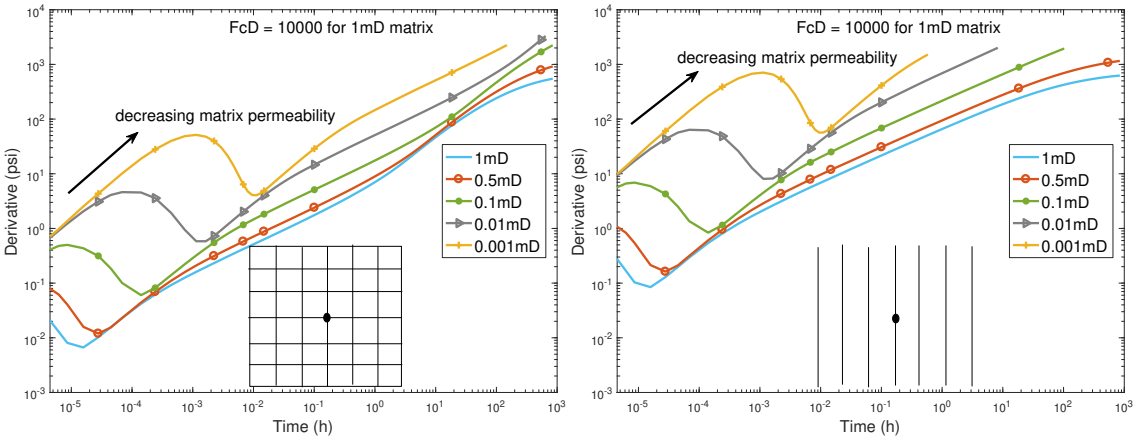

(a) (b)

Figure 4.10: Simulated pressure derivatives of a well intersecting fractures in idealised fracture networks with a matrix permeability ranging from 1 to $0.001mD$ for a connected fracture network (a) and disconnected fractures (b).

When applying the same changes in matrix permeability and matrix volume to the outcrop-based fracture patterns that are well connected (Figure 3.10 lower inset) and simulating a well intersecting fractures, the same pressure response in Figure 4.10a and Figure 4.11a is apparent in Figure 4.12a and Figure 4.12b, respectively. Here, we rescaled the entire model dimensions and adjusted the fracture properties to ensure that the fracture aperture remains unchanged, i.e. the increase in fracture volume is only due to the increased fracture length, not fracture width.

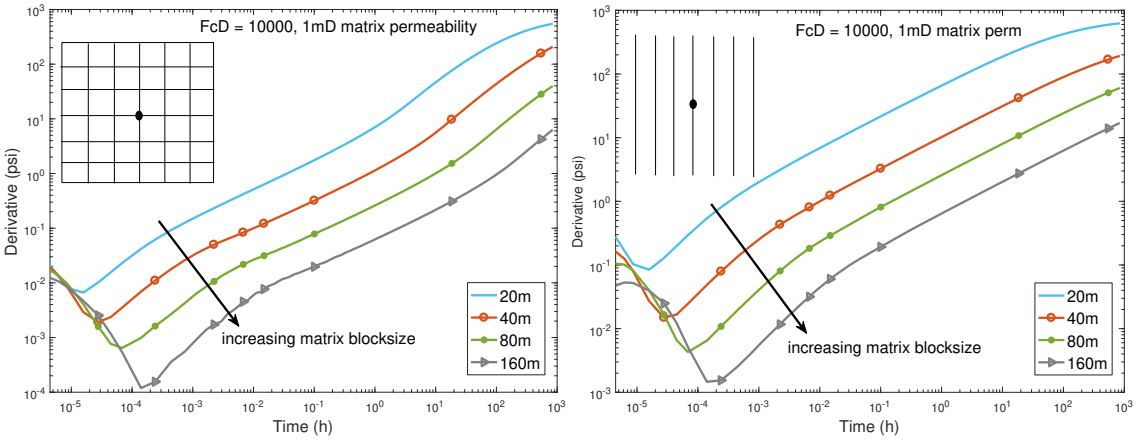

(a) (b)

Figure 4.11: Simulated pressure derivatives of a well intersecting fracture(s) in idealised fracture networks with increasing matrix block size from 20 to 160m at a constant matrix permeability of 1mD for a connected fracture network (a) and disconnected fractures (b).

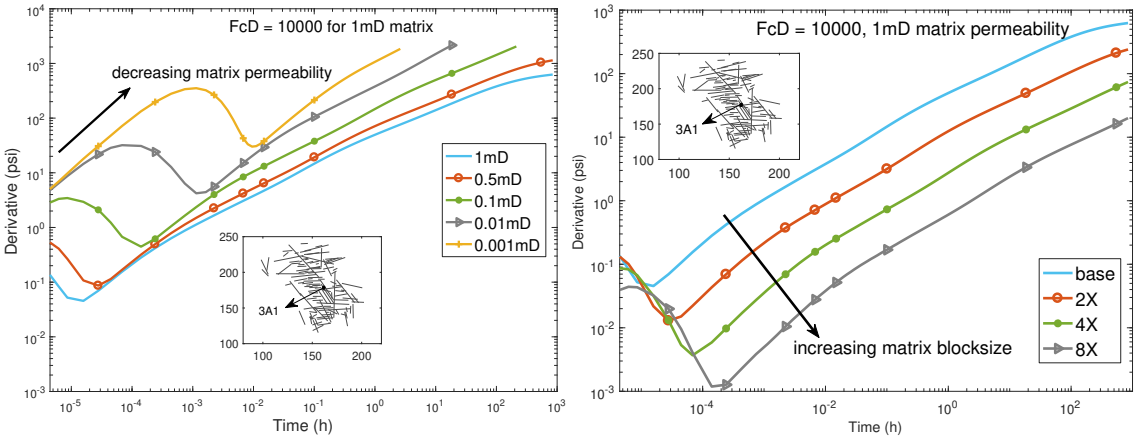

(a) (b)

Figure 4.12: Simulated pressure derivative of well intersecting fractures in an outcrop fracture pattern with decreasing matrix permeability ranging from 1 to 0.001mD (a) and increasing matrix block size up to a factor of 8 (b).

4.5 EFFECT OF FRACTURE NETWORK CONNECTIVITY AND SIZE

Another example is presented where the dual-porosity signature can be observed for unrestricted inter-porosity flow even if the matrix permeability is high. This scenario occurs if the well intersects a fracture but this fracture belongs to a small fracture network or is an unconnected fracture that is located in, but not connected to, larger fracture(s). In these cases, fluids are first produced from the smaller fracture (network), then from the rock matrix, and then from the larger network. This implies that the multi-scale nature that is common to many fracture networks (e.g., Odling, 1997) can be critical to the presence

of the dual-porosity signature. To investigate this phenomenon quantitatively, we run a number of test simulations for both connected (Figure 4.13a insets) and disconnected fracture (Figure 4.13b insets) networks and placed the well into an isolated fracture that is located close to, but not connected to, the larger fracture system. The fracture geometries differ from those shown previously in that they are even further idealised networks. Figure 4.13a and Figure 4.13b show the resulting pressure transients for the connected and disconnected network, respectively. In each case, we observed that where the smaller fracture is not connected to the nearby large fracture(s), the first flow regime is either bi-linear or linear flow, depending on the fracture conductivity. In the examples presented in these two figures with F_{CD} = 1000, the initial flow regime shows linear flow. Where the fracture is not surrounded by any other fracture, this initial flow regime changes to pseudo-radial flow, as illustrated in the single fracture case above (Figure 3.8). However, where our simulation models contain other fractures surrounding the smaller ones that intersect the well, the resulting flow behaviour is significantly different after the initial flow period (Figure 4.13). Here, after the smaller fractures are depleted, the larger fractures begin to deplete just as the transient response from the small intersected fracture tends towards pseudo-radial flow with the surrounding matrix flow. This second depletion of the larger, nearby fractures yields the dual-porosity V-shape observed here. After this dual-porosity behaviour ceases, the entire system then stabilises. However, the moment the smaller fracture is connected to any of the surrounding large fractures, the dual-behaviour signature disappears because the entire fracture network responds as one single network.

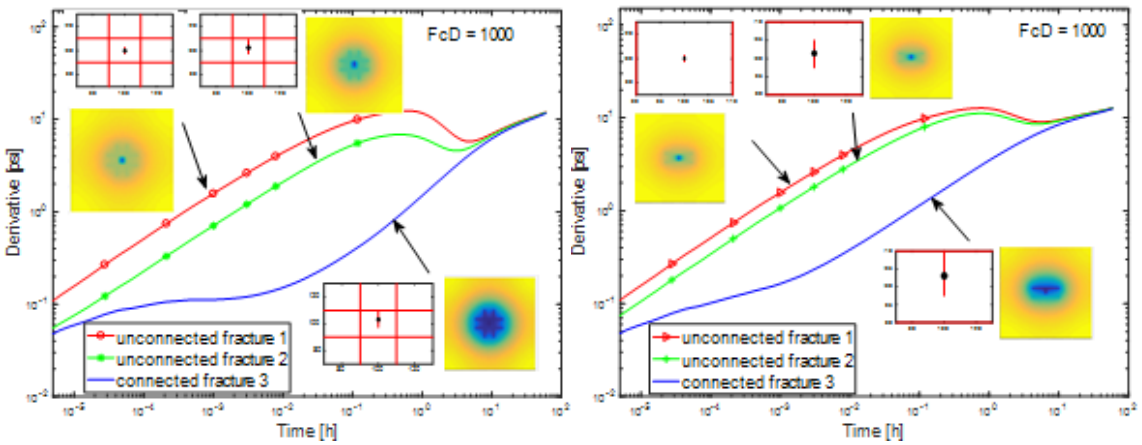

(a) (b)

Figure 4.13: Idealised models showing fracture geometry, simulated isobars around the well and pressure derivatives of smaller (un)connected fractures close to large fractures for a connected fracture network (a) and a disconnected fracture network (b).

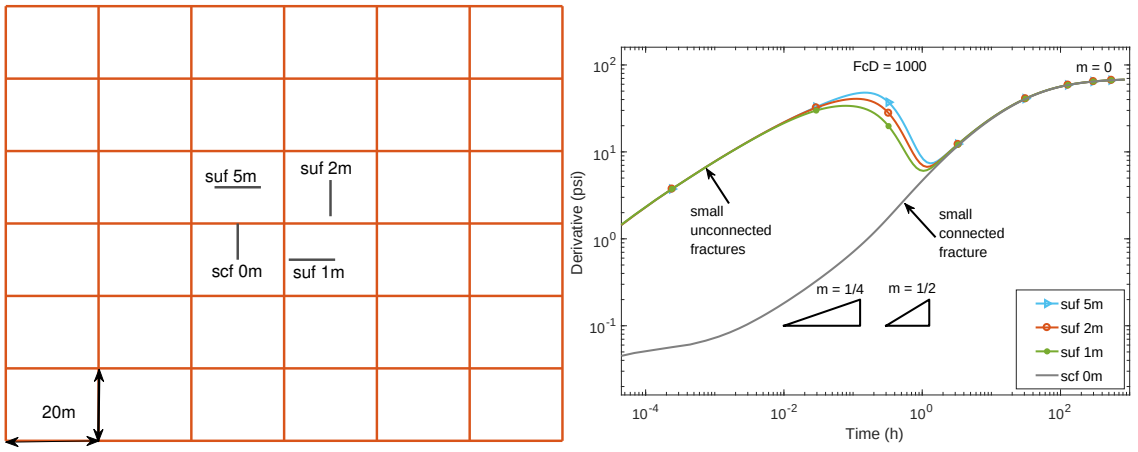

(a) (b)

Figure 4.14: A well intersecting smaller (un)connected fractures in an idealised connected fracture network. Fracture geometry with a 5, 2 and 1m separation distance between smaller fractures and the large fractures (a) and simulated pressure derivatives of the configurations shown (b).

The dependence of the dual-porosity signature on wells located in small-scale fractures that are disconnected from the larger sale fractures is independent of the fracture geometries. Figure 4.14b and Figure 4.15b show the pressure transients for the idealised connected fracture networks (Figure 4.14a: see further description in Table 4.1, Model 8) and disconnected fracture networks (Figure 4.15a: see further description in Table 4.1, Model 9). In the disconnected fracture network, smaller disconnected fractures have been added but are kept separated from the closest large fracture by distances of 5, 2, and 1m, respectively. Importantly, the orientation of the minor fractures does not impact the presence or absence of the dual-porosity signature; only the distance of separation between the fractures is important. This is expected for this case because the fracture geometry is rotationally symmetric. However the similar behaviour was observed for asymmetric case presented below. As noted above, the fracture half-length can be estimated from the linear flow regime. Here we estimate the fracture half-length of the small fracture from the early linear flow regime. When the small fracture is connected to the nearby large fractures, the flow behaviour is different. Figure 4.14b shows that simulated pressure transient for the small connected fracture is an S-shape, consistent with our results for connected fracture network presented in Figure 4.3a. In the disconnected fracture network (Figure 4.15b), the minor connected fracture results in a linear flow regime which then transitions to pseudo-radial flow, as already observed in the findings shown in Figure 4.4a. The half-length estimated from the linear flow regime in the disconnected fracture network corresponds to that of the combined lengths of the small and large fractures. This is in contrast to the situation where the small fracture is isolated and only the length of the small fracture can be estimated. Results presented in Figure 4.13 to Figure 4.15 confirm that a fractured reservoir with unrestricted

inter-porosity flow generates a dual-porosity signature if the well is intersecting a smaller fracture located close to a large fracture or fracture network.

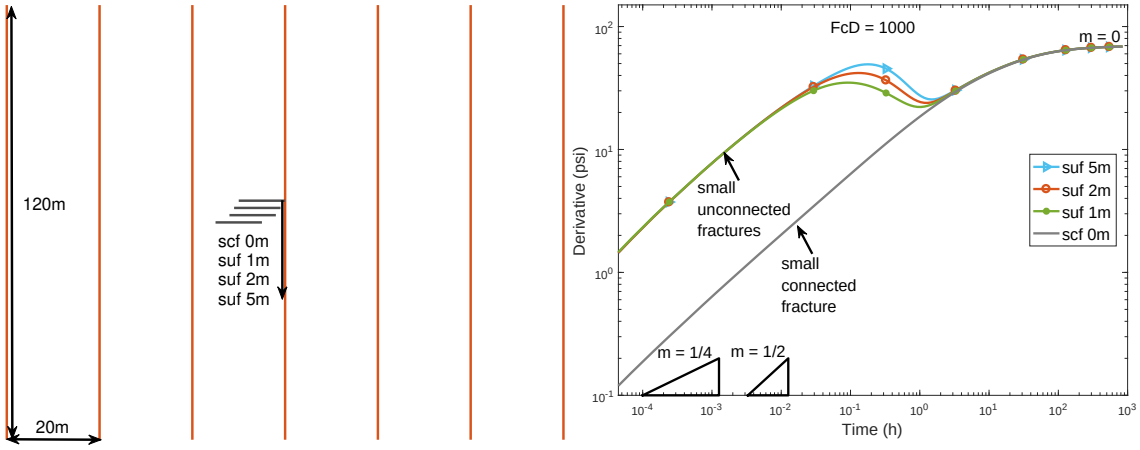

(a) (b)

Figure 4.15: A well intersecting smaller (un)connected fractures in an idealised disconnected fracture network. Fracture geometry with a 5, 2 and 1m separation distance between smaller fractures and the large fractures (a) and simulated pressure derivatives of the configurations shown (b).

However, not all small fractures that are disconnected from the larger fractures cause a clear dual-porosity behaviour (i.e., the V-shape profile of Warren and Root (1963). To quantify when the small, disconnected fractures cause a dual-porosity signature, we establish a simple relationship, the effective length ratio ELR, between the lengths of the small and large fracture(s). We define ELR as

$$ELR = \frac{l_{suf}}{L_{lf}}, \tag{4.2}$$

where l_{suf} and L_{lf} denotes length of the small unconnected fracture and length of nearby large fracture respectively.

Using this relationship, we run simulations on the idealised disconnected fracture networks, adding fractures with ELR ranging from 0.1 to 1.0 (Figure 4.16a; see further description in Table 4.1, Model 10). The resulting pressure transients (Figure 4.16b) show that the dual-porosity signature is more prominent when the length of the smaller fracture is small compared to the nearby larger fracture. As the value of ELR increases, the dual-porosity signature diminishes. Once ELR exceeds 0.5, the dual-porosity signature is absent. Furthermore, it can be observed from Figure 4.16b that the symmetry of the limbs of the dual-porosity V-shape is also a function of the ELR. Small values of ELR tend to yield a V-shape curve with first limbs (upper left to bottom right direction) that are more symmetrical to the second limbs (bottom left to upper right direction) while large ELR values

produce first limbs that are asymmetrical to the other limb. Flow regimes identified prior to the emergence of this first limb depend on the properties of the smaller fracture intersected by the well. The second limb of this shape relates to fracture conductivity and nature of fracture network connectivity.

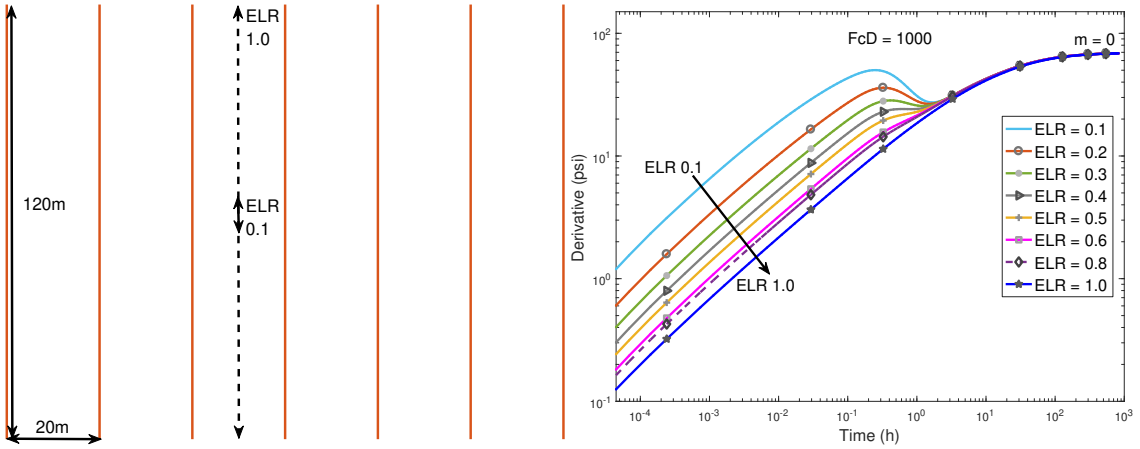

(a) (b)

Figure 4.16: A well intersecting smaller unconnected fracture in an idealised disconnected fracture network. Fracture geometry with an increasing length (*ELR* of 0.1-1) of a smaller fracture located close to large fractures (a) and simulated pressure derivatives of the configurations shown (b). *ELR* is the effective length ratio defined in Equation 4.2.

The impact of *ELR* on the dual-porosity behaviour is also apparent in the outcrop-based fracture patterns (shown in Figure 3.10 lower and upper insets). We identified unconnected (smaller) fractures with different lengths (Figure 4.17a and Figure 4.18a), calculated the corresponding *ELR*, and simulate the pressure transients (Figure 4.17b and Figure 4.18b) for cases where the well intersects these (smaller) fractures. In Figure 4.17b, the results show a clear dual-porosity signature for all cases except for case F5 where $ELR = 0.56$, i.e. above the cut-off value of 0.5. In addition, Figure 4.18b results do not show a clear dual-porosity signature for all cases except for case Ex1 where $ELR = 0.16$, i.e. below the cut-off value of 0.5.

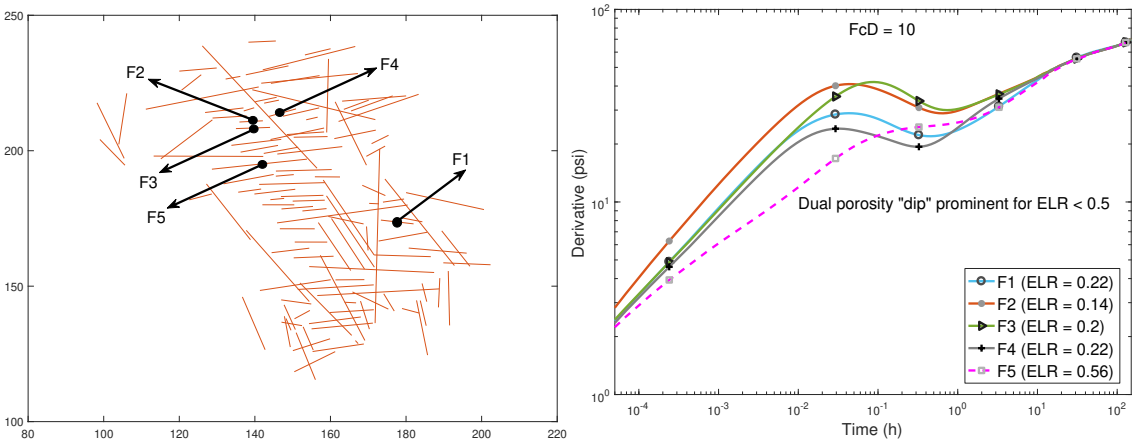

(a) (b)

Figure 4.17: A well intersecting smaller unconnected fractures located in the Jandaira Formation (Figure 3.10, lower inset). Fracture geometry with variable lengths of fractures and separation distances between smaller fractures and the large fractures (a) and simulated pressure derivatives of the configurations shown (b).

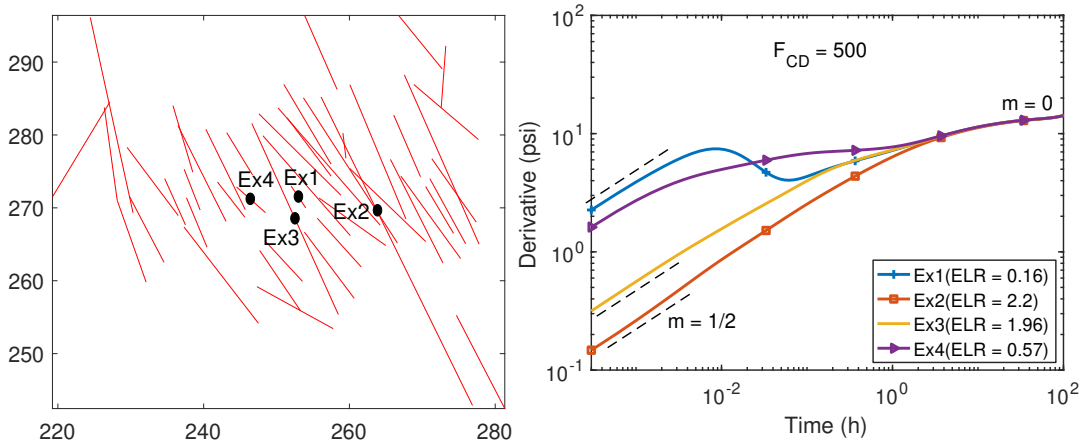

(a) (b)

Figure 4.18: A well intersecting smaller unconnected fractures located in the Jandaira Formation (Figure 3.10, upper inset). Fracture geometry with variable lengths of fractures and separation distances between fractures intersected by well and the nearby fracture(s) (a) and simulated pressure derivatives of the configurations shown (b).

4.6 CHAPTER 4 SUMMARY

This chapter applies the geoengineering workflow to generate synthetic pressure transient responses for various idealised fractures and realistic fracture networks with uniform conductivity. It also quantifies when and why the assumptions inherent to the dual-porosity model break down when interpreting well-test data from NFR. Furthermore, the chapter also demonstrates when dual-porosity

model pressure responses are valid and systematically present alternative interpretations to reservoir features that characterise this behaviour in NFR. Based on the numerical simulations and the results presented in this chapter, the following conclusions are drawn:

a. The lookalike dual-porosity model response is observed on well-test data from a NFR if a well is located in the reservoir matrix adjacent to, but not intersecting, a fracture;

b. For a well that intersects a fracture, the dual-porosity V-shape of the Warren and Root (1963) well-testing signature is observed in Type 2 and 3 of Nelson's (2001) classification due to the following situations:

   i. the effect of the fracture skin, similar to that in Cinco-Ley and Samaniego (1977);

   ii. the matrix permeability is very tight ($< 1mD$), similar to unconventional reservoirs (e.g. tight gas sands);

   iii. the well intersects a small unconnected fracture (or fracture network) located near a single large fracture or a large fracture network.

c. Reservoirs can be fractured even if the dual-porosity V-shape in the well-test data is absent.

Natural fractures have a significant effect on hydrocarbon recovery and reservoir productivity. Therefore, it is critical to identify fractures and assess the flow behaviour early on during a development to improve reservoir performance and optimize recovery. A reservoir characterisation that relies on the appearance of a dual-porosity V-shape on pressure derivatives reduces the chance of identifying and properly interpreting fractures from well-test data. If not properly characterized (or missed), fractures could cause production issues and result in a detrimental effect on hydrocarbon recovery as discussed in Chapter 2. This chapter results show a range in flow behaviour from a pressure transient analysis that could indicate the presence of fractures in a reservoir where the classic dual-porosity V-shape is absent. However, where the conventional dual-porosity signature is recognisable, it provided insight into the key geological features (including fracture skin, matrix permeability, fracture-network connectivity and size) that characterise this response. Our findings on wells intersecting smaller fractures give insight into the occurrence of fracture-network sizes and their connectivity in a field.

Identification and quantification of multiscale fractures is invaluable in assessing the role of different fracture sets during production. The influence of these fractures can be harnessed when planning IOR/EOR schemes to improve

recovery. We observed that the limbs of the dual-porosity V-shape can provide further diagnosis about the fracture-network conductivity and connectivity. Generally, a shallow symmetrical V-shape indicates low fracture conductivities, and a steep V-shape points to high fracture conductivities. For the high fracture conductivity cases, the second limb of the V-shape can differentiate a connected fracture network (with 1/2 slope) from a disconnected fracture network (with 1/4 slope). Where the dual-porosity V-shape results from the well intersecting a small-unconnected fracture located near a large fracture or fracture network, the symmetry of the first limb to the second is a function of the small fracture. The size ratio (ELR) as already described in Section 4.5 impact the symmetry of the V-shape in multiscale fracture network. Other factors include the distance and the differences in conductivity of the unconnected fracture to the large fracture network. Closer distance between the fractures are likely to yield symmetric V-shape than farther distance of separation between the small unconnected fracture and large fracture network. In addition, multiscale fractures with similar order of magnitude of conductivity are more likely to produce symmetric V-shape and those with multi-conductivity asymmetric derivative. However, many factors in the reservoir geology can affect these indicators and result in non-uniqueness issue common to well tests data. For this reason, these derivative fingerprint need to be integrated with other field data to decipher a given reservoir flow dynamics.

Furthermore, the V-shape pressure derivatives presented in this chapter are not related to the physical processes described in Warren and Root (1963) dual-porosity model. The dual-porosity model related the classical dual-porosity signature to mere exchange between matrix and fractures for well intersecting fractures. How the lookalike signature (V-shape) presented in this chapter can be linked to specific reservoir features dissimilar to the Warren and Root model. Thus, the values of ω and λ that can be estimated from the V-shape of the derivatives presented in this thesis do not quantitatively correspond to those derived from the dual-porosity model V-shape. In general, several studies have indicated that the Warren and Root dual-porosity parameters, ω and λ have no physical meaning (Stewart, 2014; Kuchuk and Biryukov, 2012).

5

DUAL-POROSITY RESPONSES FOR HETEROGENEOUS FRACTURE NETWORKS

5.1 INTRODUCTION

In Chapter 1 and 2 of this thesis, the Aguilera (1983) and Nelson (2001) fracture classification based on permeability and porosity, and their impact on fluid flow in geological reservoirs are presented. The range of influence of fractures on reservoir performance can be attributed to their spatial variations in fracture properties including fracture conductivity, which can span orders of magnitude. These fracture heterogeneities result in complex combined effects that impact fluid flow (Gilman, 2003; Agar et al., 2010; Zhou et al., 2014). Therefore the industry has adopted the view that "finding fractures is not enough" (Nelson, 2001); it is equally important to evaluate fractured reservoirs (or at least the fracture networks) in proportion to the reservoir problem being addressed in order to properly characterise and develop them.

Chapter 1 and 3 also described how Pressure Transient Analysis (PTA) of dynamic reservoir data collected during well-tests (Bourdet, 2002; Corbett, 2009; Corbett et al., 2012) is valuable to decipher flow behaviour in a fractured reservoir. Yet the pressure transients observed in the wells may not show the conventional well-test signatures or flow regimes for a given fracture property as demonstrated in Chapter 4. In this case, the effect of fractures on production would be misinterpreted or even completely missed. In addition to the observations on dual-porosity responses discussed in Chapter 1 and 4, other examples of pressure transient responses that are often misinterpreted is the location of wells within the fractures network and variations in fracture conductivity within and between fractures. The location of the producer and variation of conductivity within the fracture network control flow rates and influence the pressure responses. Generally, conventional well-test analysis assumes that the producer is located in symmetrical fracture networks and fractures are assumed to have uniform conductivity (Gringarten et al., 1974; Cinco-Ley and Samaniego-V., 1981; Bourdet, 2002; Restrepo and Tiab, 2009; Earlougher, 1977; Gonzalez-Chavez and Cinco-Ley, 2006). To account for spatially varying conductivity and different pro-

ducer locations in a fracture network in order to better characterise the impact of fractures on reservoir performance, this chapter investigates their effect on pressure transients in a range of fracture geometries from single to complex fracture networks (Figure 5.1).

As in Chapter 4, we integrated various reservoir data from fractured formations in a geoengineering workflow (Corbett et al., 2012; Egya et al., 2018c) with a Discrete Fracture Matrix (DFM) technique (Karimi-Fard et al., 2004; Geiger et al., 2009) that uses unstructured-PEBI grids to represent the fractures explicitly. The remaining sections of this chapter outlines how the methodology is applied in our investigation and the details of our results for single, multiple and complex fracture geometries. We close each sections of the simulation results analysis by highlighting the important features of non-uniformity of fracture conductivity and asymmetry location of producing well in fracture network.

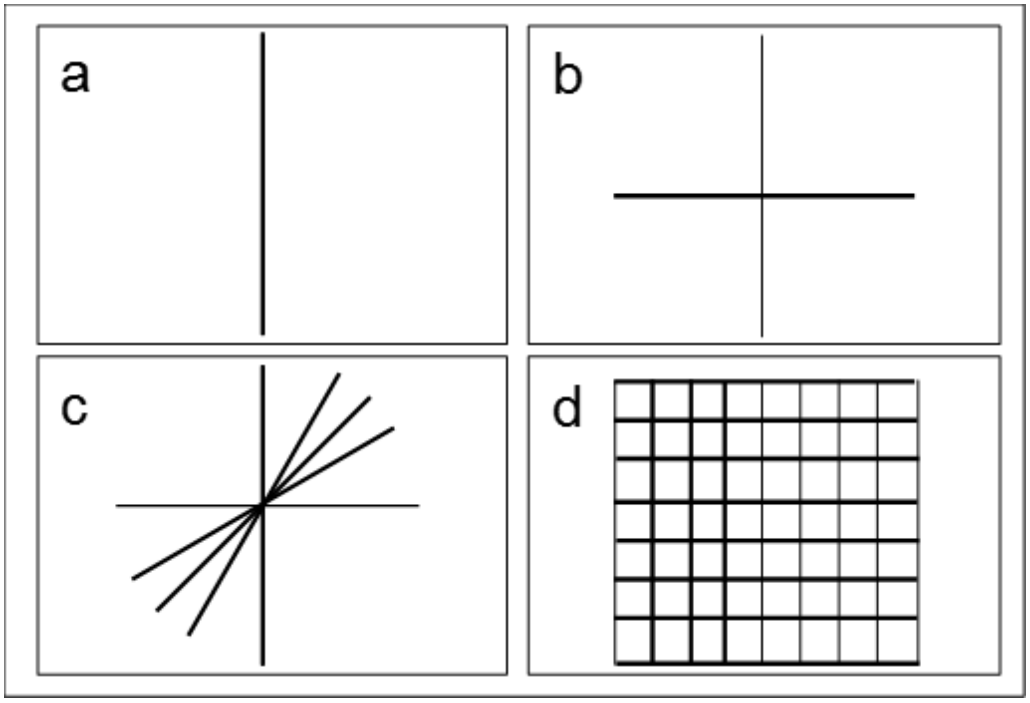

Figure 5.1: Fracture geometries considered in this study: Single fracture (a), two perpendicularly intersecting fractures (b), multiple intersecting fractures (c), and connected fracture network (d).

5.2 BASE CASE ANALYSIS

Figure 5.2 compares our simulation results for known pressure transients in simple fracture geometries. In this case, the well is located centrally in a square reservoir model and symmetrically within the fracture geometry. The dotted and solid lines on the plots indicate changes in pressure and derivative, respectively. The insets (red lines) illustrate fracture geometry that is simulated. The results

of the sensitivity analysis with the simple fracture geometries provide base cases for comparison when interpreting pressure transient behaviour for complex scenarios that we will be analysing later in this chapter.

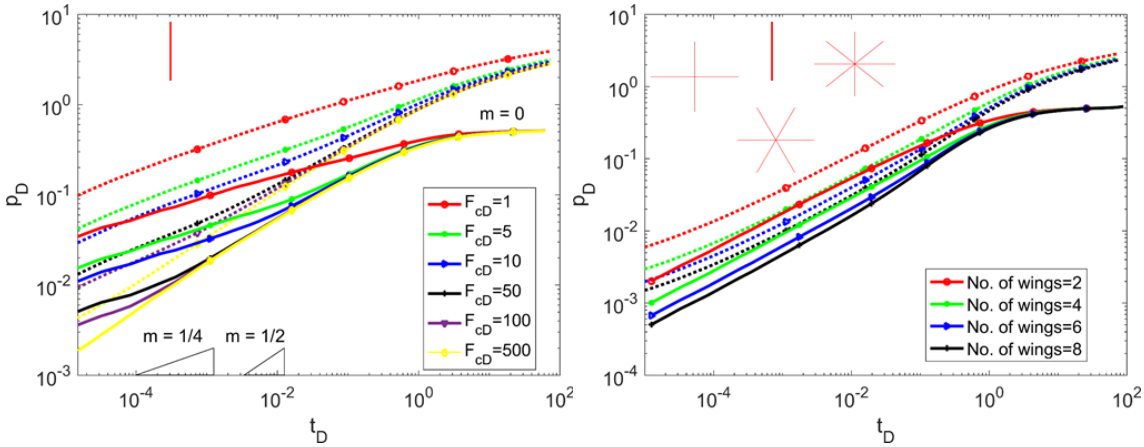

Figure 5.2: Fractured model showing pressure transients of a single, two-wing fracture, at different dimensionless fracture conductivities F_{CD} (a); recall that the slope m of 0, 1/4 and 1/2 represents pseudo-radial, bilinear and linear flow regimes respectively. Pressure transients for multiple intersecting, multi-wing fractures showing the effect of fracture numbers at F_{CD} = 500 (b). The insets (red lines) represent fracture geometry simulated.

Figure 5.2a shows the effect of changes in F_{CD} on the pressure transients for a single, two-wing fracture. From top to bottom, the flow regimes identified for changes in the conductivity include bilinear flow ($m = 1/4$), linear flow ($m = 1/2$) and radial flow ($m = 0$). The first flow regime for a well that intercepts a fracture characterising a low F_{CD} up to 100 is the bilinear flow. This corresponds to finite-conductivity fractures in which the emergence of bilinear flow results from drop in pressure within the producing fracture. As the fracture conductivity increases, the bilinear flow diminishes and a linear flow regime emerges as the first observed flow regime. The linear flow regime is followed by radial or pseudo-radial flow, which indicates high-conductivity fracture flow that is characteristic of infinite-conductivity fractures. In this case, pressure within the producing fractures is maintained during production. This behaviour is observed for infinite acting fractures with $F_{CD} \geq 300$ (Cinco-Ley and Samaniego-V., 1981). Figure 5.2b shows the effect of the number of fractures intersected by a producer at F_{CD} = 500 (similar to the model of Wanjing and Changfu (2014)). To create a reservoir model with symmetric fracture geometry and well location, the fracture wings are distributed evenly in each configuration (e.g. 1800, 900, 600, and 450 for two-wing, four-wing, six-wing and eight-wing geometry respectively).

The multiple intersecting (multi-wing) fracture half-length (l_{mwf}) estimated in the analysis is given by

$$l_{mwf} = \frac{1}{2} N_{fw} l_w \tag{5.1}$$

where N_{fw} and l_w denote the number of fracture wings and fracture half-length (radial distance from symmetrically located wellbore to the outer tip of a fracture intersected by the well), respectively.

Now that the behaviours for the base case are established, we will demonstrate when and how pressure transients deviate from this behaviour considering several cases of a single fracture, multi-wing fractures and connected fracture network. In each case, we investigate the effect of variation in fracture conductivities and well location on the transient pressure response. Details of our simulation results are presented below.

5.3 Effect of variation in fractures conductivity and well location

5.3.1 *Application to a single fracture*

Using a mean F_{CD}, we generated variable fracture conductivities along a single fracture length with deviations in F_{CD} of 0 to 75% (Figure 5.3). The variation in F_{CD} along the length of a single fracture and the corresponding histogram for a given deviation are shown in Figure 5.3a. Figure 5.3b shows the simulated pressure derivatives for a single fracture with non-uniform F_{CD}. The pressure transients in Figure 5.3b show that the variable conductivity (or aperture) within a fracture is recognisable in finite-conductive fractures (with F_{CD} of up to 10) but less obvious when F_{CD} reaches 100. In lower conductivity cases with $F_{CD} \leq 1$, the effect continued to influence the derivative until the transition to pseudo-radial flow regime. However, the derivative profile is not uniquely different from one with uniform conductivity. On the other hand, an infinite-conductive fracture (e.g. F_{CD} = 500) is not affected by heterogeneous fracture conductivity because there is no apparent pressure drop within the producing fracture.

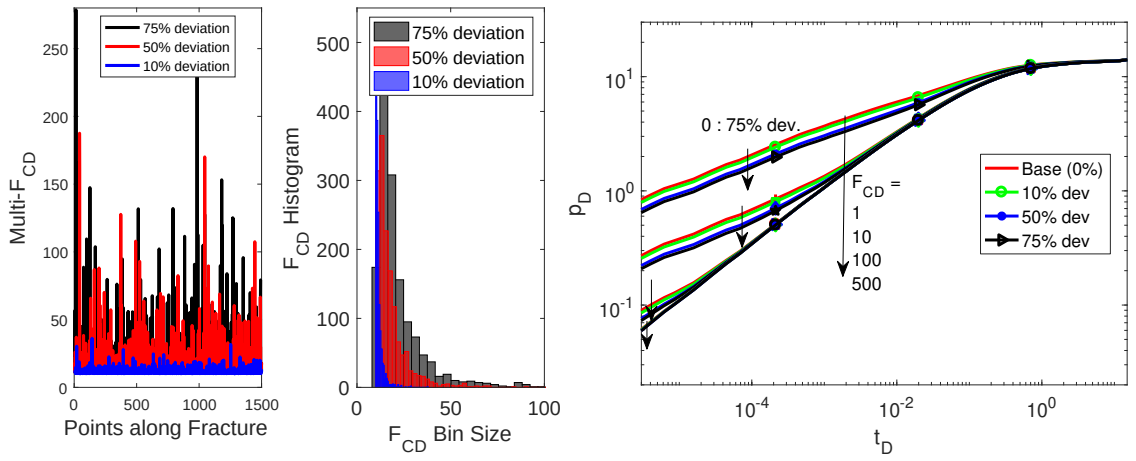

(a) (b)

Figure 5.3: Variation of dimensionless fracture conductivity F_{CD} within a single fracture, showing distribution of F_{CD} along the length of a single fracture and corresponding histogram for different deviations for the mean F_{CD} (a) and simulated pressure response for a single fracture with variable conductivity (b).

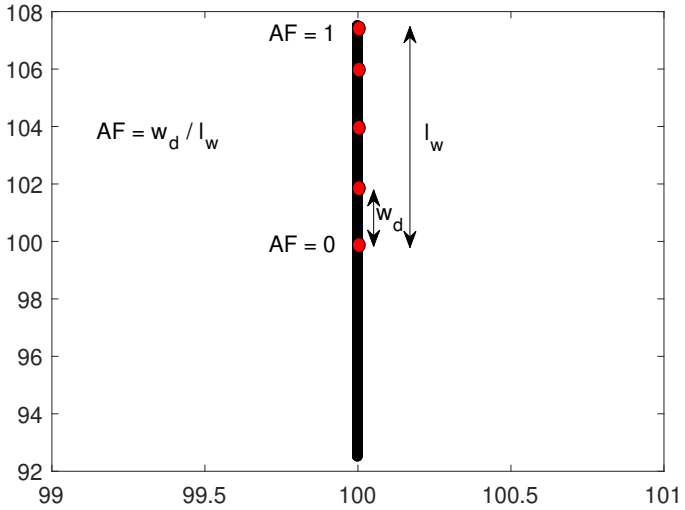

Figure 5.4: Fracture geometry showing the offset of a well from the centre of a single fracture. AF, w_d and l_w denote the well asymmetry factor, distance of well offset from the centre, and fracture half-length, respectively.

In the same way, the effect of the well location, i.e. if the well is located symmetrically or asymmetrically within the fracture, (Figure 5.4) is obvious in a finite-conductivity fracture (Figure 5.5). F_{CD} plots in Figure 5.5 are grouped in multiples of ten for presentation purposes. The asymmetry of the well location within the fracture is given by the asymmetry factor $AF = w_d/l_w$, where w_d denotes the distance of well offset from the centre. In Figure 5.5, the effect of AF becomes noticeable at early time, and continues to diminish, with the increase in fracture conductivity. However, as F_{CD} increases beyond the infinite-conductivity threshold ($F_{CD} \leq 300$), the effect of AF is hardly recognisable in the pressure derivatives.

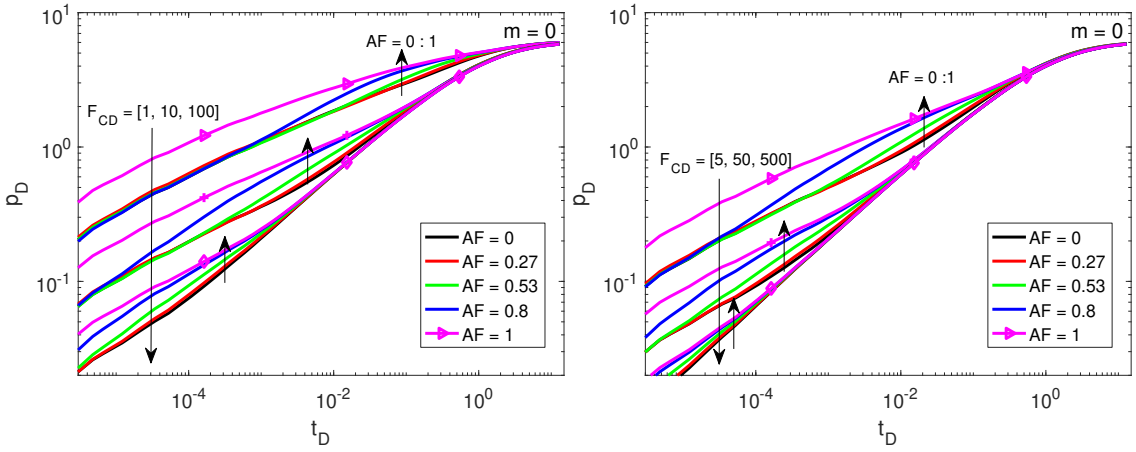

(a) (b)

Figure 5.5: Simulated pressure derivatives showing effect of asymmetry factor (AF) for a single fracture with F_{CD} = [1, 10, 100] (a); and F_{CD} = [5, 50, 500] (b).

Another technique for evaluating AF in fractured reservoirs was reported in literature (e.g., Berumen et al., 2000). Their study demonstrates that the relative position of a producer with respect to the fracture geometry influences pressure transients and should be considered for fracture characterization. However, their proposed evaluation technique is not currently accessible in a standard well-testing analysis software package

5.3.2 *Application to Multiple Intersecting (Multi-wing) Fractures*

For single and multi-wing fractures as shown in Figure 5.2, the appearance of the four conventional flow regimes, fracture linear flow, bilinear flow, formation linear flow, and infinite acting pseudo-radial flow, depends on the fracture conductivity. For infinite fracture conductivity ($F_{CD} \geq 300$), the effect of depletion at fracture tip is felt by the well before matrix recharge starts. Thus the estimated fracture half-length l_w (Equation 5.1) during the early-time fracture linear flow regime and formation linear flow is the same (Cinco-Ley and Samaniego-V., 1981; Ahmed and McKinney, 2005). In this case, the bilinear flow regime is not observed in-between the two linear regimes. For finite-conductivity fractures ($F_{CD} < 300$), the early-time fracture linear flow duration is very short and l_w is unrealistically small because the depletion within the producing fracture is yet to reach the fracture tips before matrix recharge into the fracture become significant. Thus, for finite-conductivity fractures l_w in Equation 5.1 can be replaced by the fracture conductivity $(k \cdot a)_f$ and l_{mwf} for multi-wing fracture conductivities by $(k \cdot a)_{mwf}$. However, Equation 5.1 only applies to the case of Well Y of Figure 5.6a and Figure 5.6b, i.e. the well that is located symmetrically at the intersection of fractures with uniform conductivity.

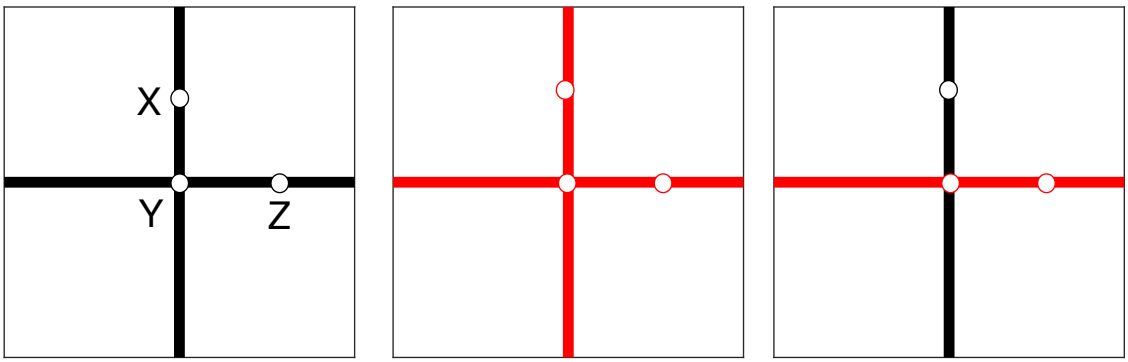

Figure 5.6: Multi-wing fracture geometry showing location of a well that intersects fracture(s) in a fracture geometry with finite-conductivity fractures (a), infinite-conductivity fractures (b), and finite- and infinite-conductivity fractures (c).

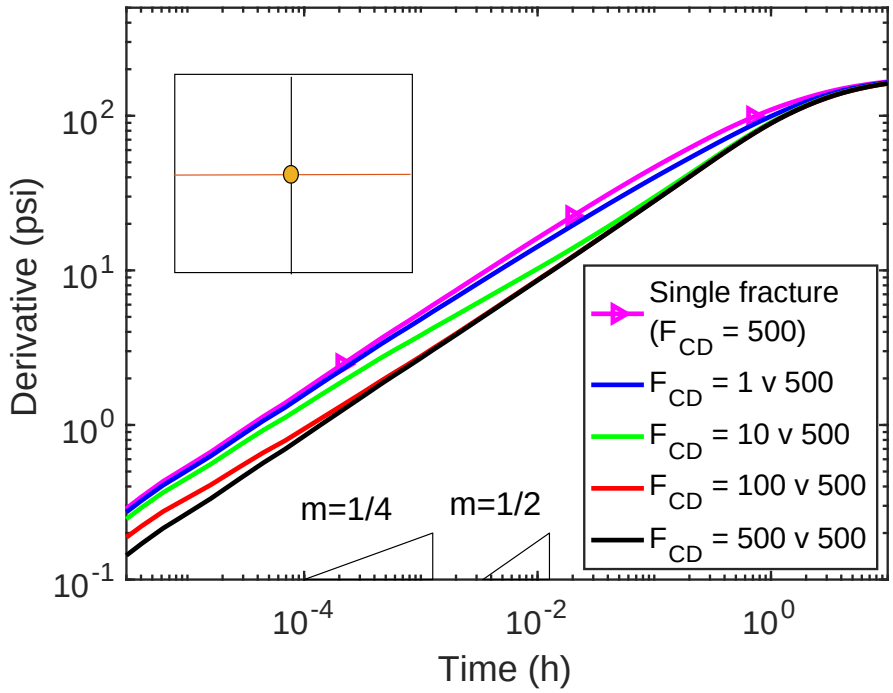

Figure 5.7: Simulated pressure response for infinite conductivity fracture intersecting with variable finite-conductivity fracture.

If the intersecting fractures have different fracture conductivities, as in Figure 5.6c, the pressure behaviour of the wells is different. Consider Well Y in Figure 5.6c. Where the F_{CD} contrast between two intersecting fractures is high (e.g., F_{CD} of 1 and 500), the actual value of l_w as detected from pressure transient analysis is close to the value of l_w of the fracture with F_{CD} = 500. For a finite-conductivity fracture with $10 \leq F_{CD} < 300$ that intersects an infinite-conductivity fracture with F_{CD} = 500, two distinct values of l_w can be detected from fracture linear flow and formation linear flow regimes, respectively. The fracture linear flow gives l_w of the infinite-conductivity fracture plus l_w of the pressure depletion distance along the finite-conductivity fracture before the start of matrix recharge. Formation linear flow gives l_w of the infinite-conductivity fracture plus l_w of the

depletion distance in the finite-conductivity fracture before the pseudo-radial flow in the infinite-conductivity fracture dominates flow behaviour. Consider the fracture geometry and the simulated pressure response shown in Figure 5.7. Assuming that the estimated l_w for a single fracture with F_{CD} = 500 is given in ratio as 1, adding the second fracture with F_{CD} = [1, 10, 100, 500], From the analysis of the geometry shown in Figure 5.7 during fracture linear flow, the estimated l_w = [1.07, 1.20, 1.53, 2.0] respectively. The result shows that only half of the l_w of the finite-conductivity fracture can be calculated during the fracture linear flow regime for the finite-conductivity fracture with F_{CD} of up to 100. On the other hand, for the same fracture geometry and F_{CD} during the formation linear flow, the estimated l_w = [1.19, 1.79, 1.94, 2.0] respectively. In addition, Figure 5.7 indicates that where two linear flow regimes are recognisable, the transition period between the flow regimes become shorter as the conductivity of the finite-conductivity fracture increases. Consequently, the pressure derivative would be characterised by longer formation linear flow and a shorter transition period between the later linear flow regime and the earlier pseudo-radial flow regime.

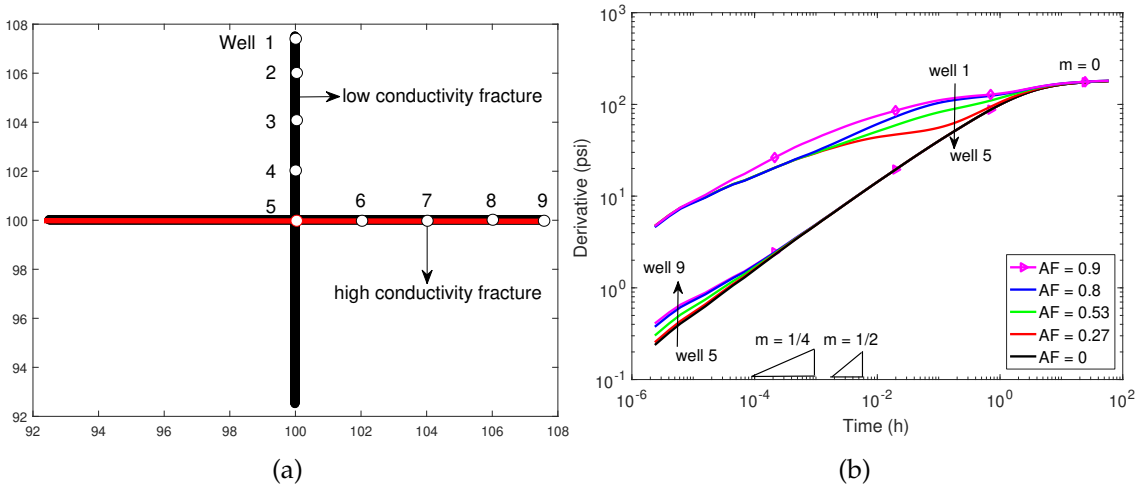

(a) (b)

Figure 5.8: Effect of fracture asymmetry factor AF and variable fracture conductivity in two intersecting fracture for fracture geometries where the well is offset from the centre of the fracture along finite- and infinite-conductivity fractures (a) and simulated pressure transients for these configuration (b).

Furthermore, to investigate the effect of variation in fracture conductivity and well location in a multi-wing fracture geometry, we consider two perpendicular intersecting fractures with finite and infinite conductivity (Figure 5.8). In this case, we do not vary the conductivity within the intersecting fractures but only between them. Where the conductivity is varied, the combined effect of the variable conductivity in the two intersecting fractures is similar to that shown in Figure 5.3 for a single fracture. If the conductivity is uniform for both fractures and the well is located at the intersection (e.g. Well 5 in Figure 5.8), the resulting fracture conductivity or half-length is twice that for a single (two-wing) fracture

(see Equation 5.1). Figure 5.8 also shows that the early-time flow behaviour of a well is strongly influenced by the fracture that it intersects rather than the entire fracture network. Wells 1 to 4 intersect a finite-conductive fracture (F_{CD} = 1) and the effect of AF on the pressure derivative described above applies (Figure 5.4 and Figure 5.5); the pressure transient is observed to deviate from the initial response only at late time (see Well 4 in Figure 5.8). The deviation indicates when the influence of the nearby infinite-conductivity fracture (F_{CD} = 500) reaches the producer and the changes in pressure response is due to the difference in conductivities between the two intersecting fractures. Wells 6 to 9 show only small changes from the base case of Well 5 where the well is located directly at the fracture intersection. This is because the flow behaviour of the infinite-conductivity fracture is least affected by the effect of AF.

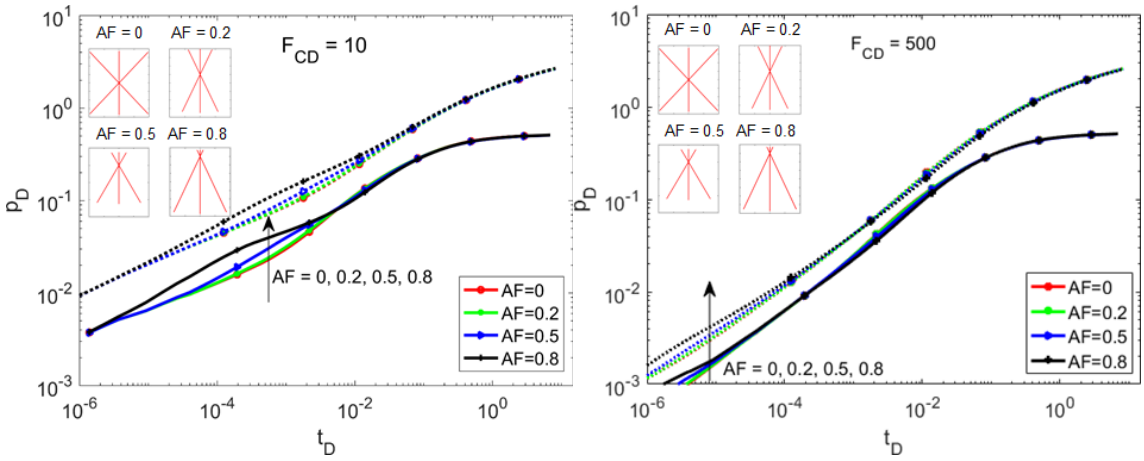

(a) (b)

Figure 5.9: Effect of AF and variable conductivity in multiple intersecting fractures. Simulated pressure for fracture geometry showing offset of a well from the centre of the fracture along finite-conductivity fractures (a) and infinite-conductivity fractures (b). The insets (red lines) represent the fracture geometry simulated.

In addition to investigating well changes in pressure transient due to changes in producer's location in a symmetric fracture geometry, we also analysed the effect for fractures intersecting each other asymmetrically at offsets along the length of a centrally located fracture. The intersection locations coincide with the well asymmetric locations corresponding to earlier described AF (see insets of Figure 5.9). In these configurations, fracture half-lengths remain the same and AF applies as previously defined. Only the intersection location is changed, corresponding to AF. Figure 5.9 shows that the effect of AF is recognisable for finite-conductivity fractures (F_{CD} = 10). As reported by Berumen et al. (2000) and Wanjing and Changfu (2014), there is an inflection point in time (t_D = 0.007) below which high AF values correspond to large pressure change and above which the opposite applies. However, this is not obvious when the same fracture geometries are simulated with infinite-conductivity (F_{CD} = 500). In this case, the

inflection point occurs earlier (t_D = 0.0002) and the period corresponding to the higher AF and pressure changes appears to exist outside the time where the pressure transient data was recorded

Importantly, we observed from the pressure transients of Wells 1 to 4 (Figure 5.8) that the pressure transient behaviour of a well that intersects a finite-conductivity fracture that is intersecting a nearby infinite-conductivity fracture shows a slanted S-shaped derivative. This derivative profile is similar to that of a well intersecting a connected fracture network with uniform fracture conductivity (Egya et al., 2018c) as depicted in Figure 5.10. The curvature and time of the transition from the dominant effect of a finite-conductivity fracture flow to that of an infinite-conductivity fracture flow depends on the conductivity and distance of the finite-conductivity fracture (intersected by the well) to the nearby connected infinite-conductivity fracture. Where this type of pressure derivatives is observed in well test data, further evaluation is needed to decipher the fracture system that may accounts for this response as it could either be due to a well that intersects a connected fracture network with uniform fracture conductivity or a well that intersects a finite-conductivity fracture that is intersecting a nearby infinite-conductivity fracture. In the case of the results shown in Figure 5.10a for two intersecting fractures with different conductivities, the pressure derivatives converged at linear flow with $m = 1/2$ and remain on this regime until the transition to a pseudo-radial flow regime. In contrast, the pressure derivatives for a connected fracture network only converged at linear flow regime for a very short period for $F_{CD} \geq 10$ and deviate from this flow regime prior to the transition (Figure 5.10b) to pseudo-radial flow.

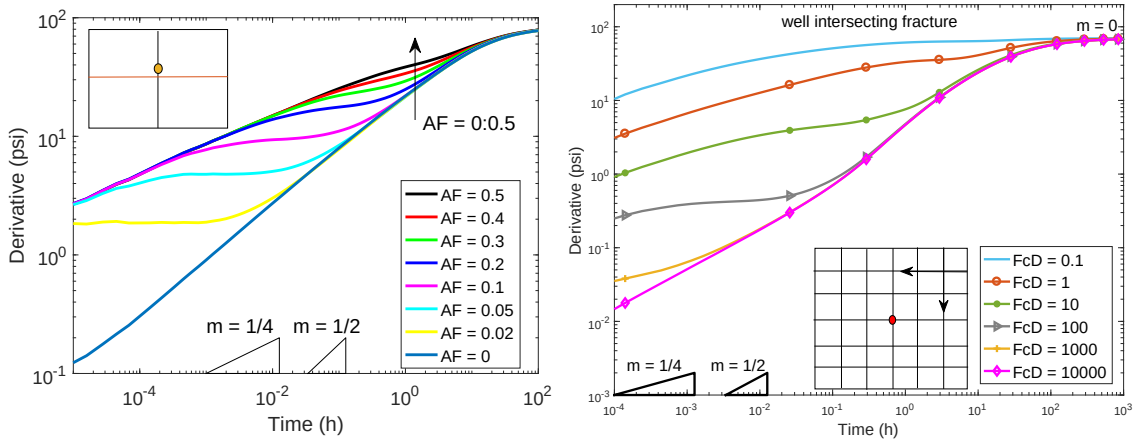

(a) (b)

Figure 5.10: Comparison of effect of AF in two intersecting fractures with connected fracture network. Simulated pressure response showing a well that is intersecting a finite-conductivity fracture that intersects an infinite-conductivity fracture (a) and pressure responses for a connected fracture network with uniform fracture conductivity (b). The insets represent the simulated fracture geometry.

5.3.3 *Effect of averaging of fracture conductivity*

Sun et al. (2016) investigated the effect of non-uniform fracture aperture, under different closure stresses, on oil production rate and cumulative oil production from Eagle Ford Outcrops maps. They compared the results of the simulations with non-uniform aperture with those of uniform fracture apertures computed with commonly used averaging techniques, such as arithmetic, geometric, and harmonic averaging. Their study shows that non-uniform fracture aperture might have an effect on oil production performance in a way that is unlikely to be captured using a single uniform aperture value. In this thesis, the effect of averaging fracture aperture (and conductivity) on the simulated pressure derivatives is investigated. Using some of the mean fracture apertures of 138, 370, and 1000 microns reported by Sun et al. (2016), 4000 fracture aperture values that varied along a $40m$ long fracture are generated. Figure 5.11 shows the variation of the fracture aperture along the fracture length and a histogram of the fracture aperture distributions for different standard deviations.

Next, we applied different techniques to average the non-uniform fracture apertures shown in Figure 5.11. Then the pressure response for both, the single averaged fracture aperture and for the actual fracture aperture distributions is simulated. Figure 5.12 shows that none of the averaging methods could reproduce the same pressure transients that are observed for cases where the fracture aperture varies along the fracture. Only for high fracture apertures of $1000\mu m$, the pressure transients are identical for any given averaging technique and the actual fracture aperture distribution because a fracture with such high average aperture behaves as infinite acting. This observation is consistent with earlier result for other cases of variable fracture conductivities and well locations discussed in earlier in Section 5.3.1 and 5.3.2. It can be observed in Figure 5.12b and c that the simulated pressure derivative for the harmonic average is much closer to those with variable fracture conductivity compare to others. This is because flow in finite-conductivity fractures occurs in series due to pressure drop along the fracture. This behaviour in low varying permeability medium is better captured by harmonic averaging of permeability.

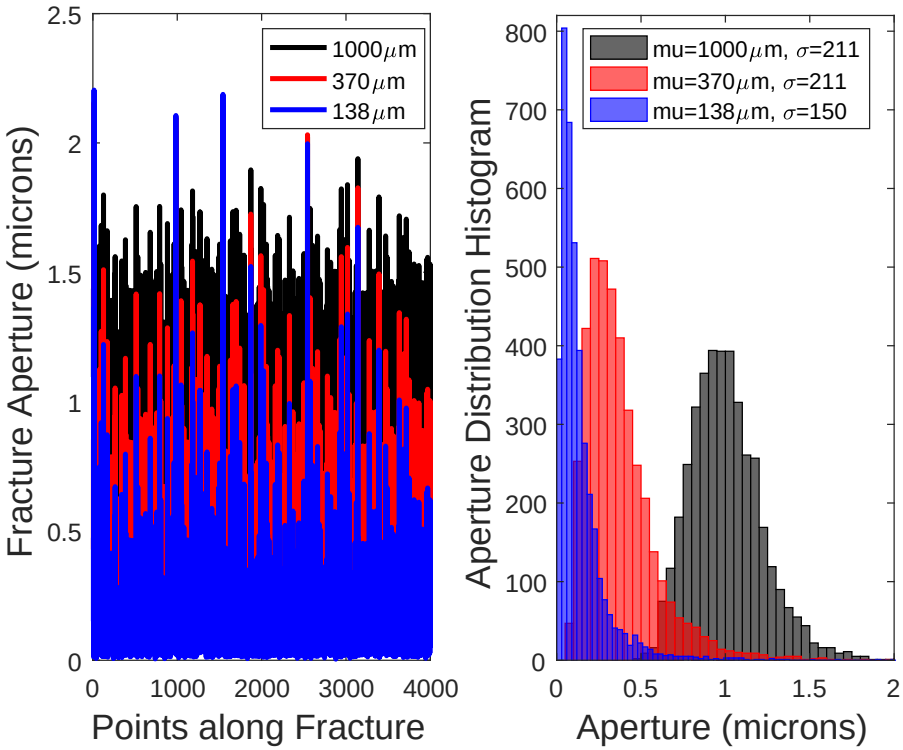

Figure 5.11: Distribution of fracture aperture values showing non-uniform fracture apertures along a $40m$ long fracture (a) and histogram of the fracture aperture distributions for different standard deviations σ (b).

The averaging techniques were also applied to two intersecting fractures, one with finite conductivity of $F_{CD} = [1, 10, 100]$ and one with an infinite conductivity of $F_{CD} = 500$. The simulated pressure responses are shown in Figure 5.13. Again, the results show that none of the averaging methods captured the pressure transient behaviours that are observed when the conductivity of the two intersecting fractures is different. However, the differences in the pressure responses become less when the contrast in conductivity between the intersecting fractures decreases, for example in the case of F_{CD} of 100 and 500. The simulated pressure responses for connected and disconnected fracture networks with different conductivity produce similar pressure behaviour to those of single and multiple intersecting fractures (see Figure 5.11 to 5.13). As demonstrated in Figure 5.11 to 5.13, the reservoir performance for finite-conductivity fractures calculated by using uniform and non-uniform fracture aperture does not show convergence. However, the use of the averaged value of fracture aperture (or conductivity) that yield closer result to the non-uniform case to quickly estimate production performance for a given reservoir conditions may provide more reliable results (Sun et al., 2016).

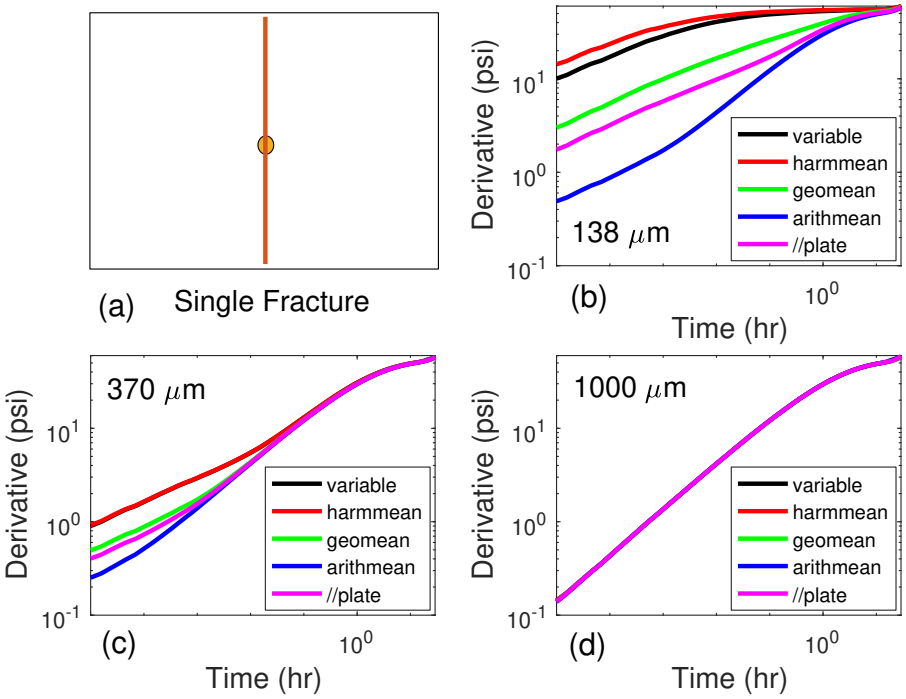

Figure 5.12: Simulated pressure derivatives for uniform and non-uniform fracture apertures in a single fracture. Fracture geometry (a) and simulation results for a mean fracture aperture of 138μm (b), 370μm (c), and 1000μm (d).

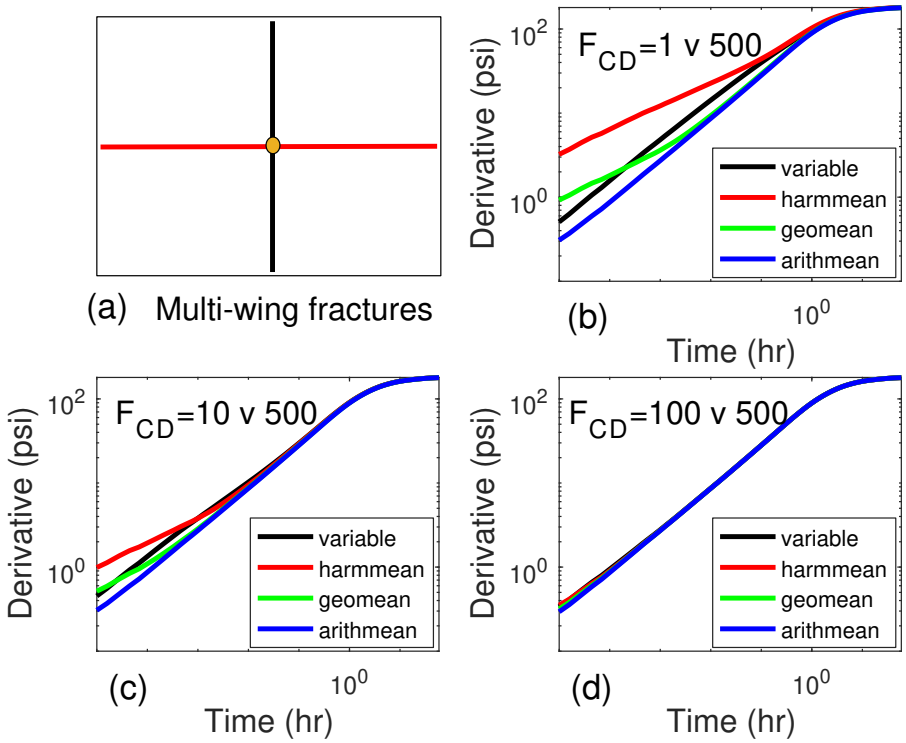

Figure 5.13: Simulated pressure derivatives for uniform and non-uniform intersecting fracture. Multi-wing fracture geometry (a) and simulation results for fracture conductivities F_{CD} of 1 and 500 (b), 10 and 500 (c), and 100 and 500 (d).

5.3.4 *Application to a Connected Fracture Network*

Finally, we extend our investigation to a large, regular fracture network. The effect of AF in the fracture network with uniform conductivity has a similar impact on the pressure transient as observed for the single- and multiple-fracture geometries above (Section 5.3.1 and 5.3.2. The similarity is that the effect of AF is obvious for finite-conductivity fractures and almost undetectable for infinite-conductivity fractures. Other cases of fracture networks with multi-conductivity fractures (Figure 5.14) where the well intersects either a finite-conductivity fracture (Well X) or infinite-conductivity fracture (Well Z) fracture, or both (Well Y) are considered. First, the case where an infinite-conductivity fracture set with fractures running parallel to each other and perpendicular to a finite-conductivity fracture set in the same reservoir model is investigated. Then the case where a small number of infinite-conductivity fractures crosscut and link infinite-conductivity fractures together (Figure 5.15) is also analysed.

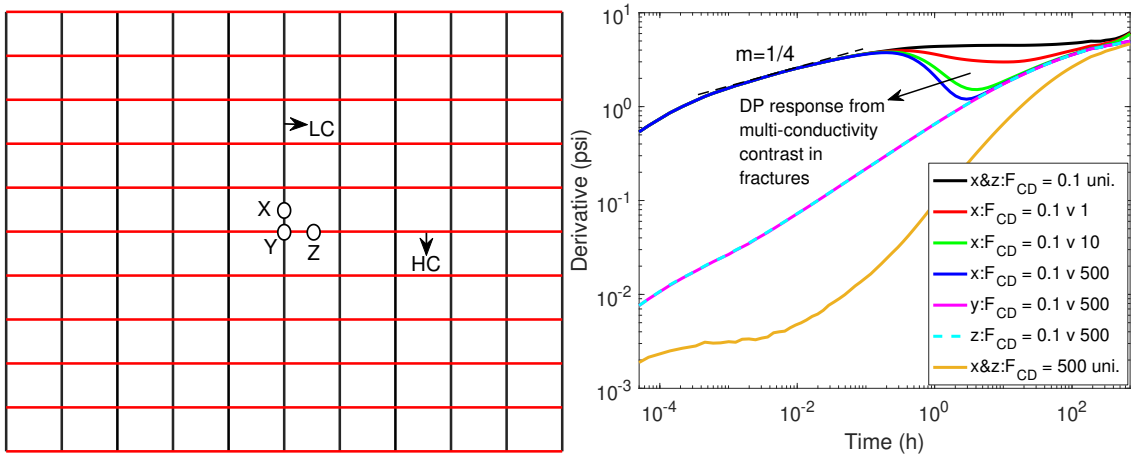

(a) (b)

Figure 5.14: Effect of multi-conductivity in fracture network. The fracture network comprising of finite- and infinite-conductivity fractures (a) and simulated pressure derivatives (b). LC and HC denote low-conductivity and high-conductivity respectively. DP denotes dual-porosity

Figure 5.14a presents a fracture network with finite- and infinite-conductivity fractures fracture running perpendicular to each other with Well X, Y or Z intersecting the finite-conductivity fracture, both the finite- and infinite-conductivity fractures, and the infinite-conductivity fractures, respectively. Figure 5.14b shows the simulated pressure derivatives, including cases where the fracture network is assumed to have uniform conductivity (F_{CD} = 0.1 and F_{CD} = 500). For uniform fracture conductivities in Figure 5.14b, the pressure transient responses are similar to those shown in Figure 5.10b above. For a multi-conductivity fracture network, the derivative is can be noticeably different from that of a uniform con-

ductivity fracture network. We observed that the results for Well Z are similar to that of Well Y. However, for Well X and with increasing conductivity contrast between the finite- and infinite-conductivity fractures, we observed an emergence of a dual-porosity V-shape in the pressure derivative (Figure 5.14b). This classic dual-porosity shape is absent if the fracture network is of uniform conductivity, the well intersects infinite-conductivity fractures (Well Z) or the well is located at the intercept of finite- and infinite-conductivity fractures (Well Y).

Furthermore, we consider the case where a number of infinite-conductivity fractures crosscut and connect infinite-conductivity fracture sets together (Figure 5.15). Figure 5.15 also shows that connection between the infinite-conductivity fractures magnifies the dual-porosity response in the pressure derivative. This means that the well productivity is enhanced and production is better supported when the infinite-conductivity fractures are linked together by other infinite-conductivity fractures. The effect of multi-conductivity in fracture networks, thus, provides another insight into the reservoir geology that account for the appearance or absent of a dual-porosity response in the pressure derivatives. Other findings on dual-porosity well test responses for both connected and discrete fracture networks with uniform fracture conductivities are detailed in Chapter 4.

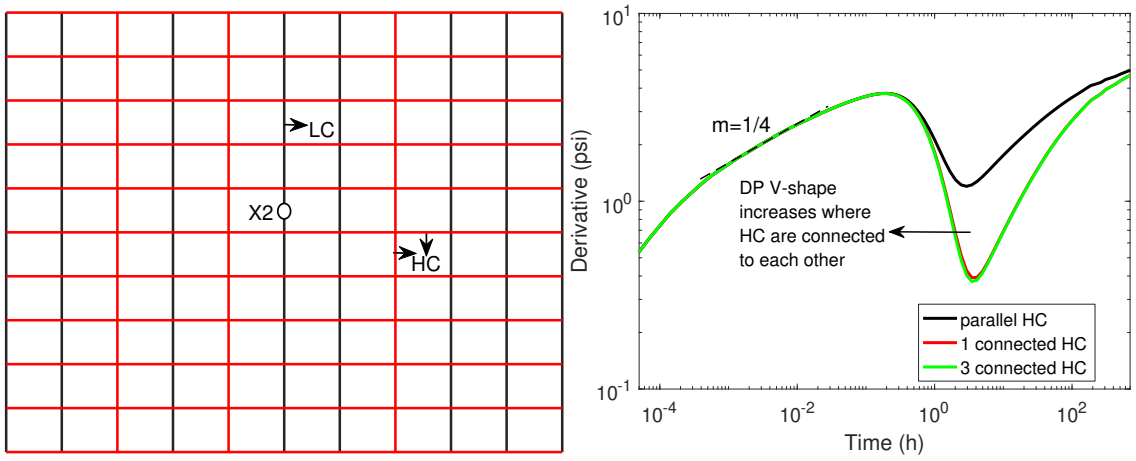

(a) (b)

Figure 5.15: Effect of connected infinite-conductivity fractures in multi-conductivity fracture network. The fracture network comprising of finite-conductivity fractures and connected infinite-conductivity fractures (a), and the simulated pressure derivatives with parallel and crosscutting infinite-conductivity fractures (b).

Similar pressure responses to Figure 5.15 would be observed if the finite-conductivity fracture is connected to an open fault instead of another fracture network with very high permeability. A case for a well intersecting a finite-conductivity fracture near an infinite-conductive fault in Ghawar Field is presented by Al-Thawad et al. (2001). In addition the finite-conductivity fractures

modeled in this chapter can also be related to the concept of bulk permeability of a fracture network (k_{fb}) described by Stewart (2014). The bulk permeability is much larger than matrix permeability estimated from core plug as it relates to the effective permeability of both the matrix and the fractures in a fractured reservoir. Thus a well with bulk permeability (i.e. that intersects smaller fractures that enhance matrix permeability) near an open fault or infinite conductivity fracture network will probably yield similar pressure response to the one presented in Figure 5.15. However, this thesis favours the concept of a well intersecting a finite-conductivity that is connected to infinite-conductivity fractures since all fractures are explicitly modelled so bulk permeability concept does not apply. Examples of where the above pressure response can be observed in the field include an NFR with multi-conductivity fractures with the well intersecting finite-conductivity fractures, and a well intersecting fractures in a fracture corridor near an open fault.

5.4 CHAPTER SUMMARY

Our results show that both, non-uniformity in fracture conductivity and the producer's location in relation to the centre of a fracture geometry are recognisable if the producer intersects a finite-conductivity fracture. Examples include, but are not limited to, the following:

i. These effects diminish with increasing fracture conductivity and may be undetectable in infinite-conductivity fractures.

ii. We observed that the flow behaviour of the producer in two (or multiple) intersecting fractures with different conductivities is influenced at early times by the fracture that it intersects; it only deviates at later time when the effect of other fractures with infinite-conductivity begin to impact production.

iii. The simulated pressure behaviour for uniform and non-uniform fracture aperture and conductivity can be significantly different, particularly for finite-conductivity fractures. None of the averaging techniques adequately captures the pressure responses for the variable fracture conductivities.

iv. The behaviour of two intersecting fractures with different conductivities where the producer asymmetrically intersects a finite-conductivity fracture can be similar to that of a producer intersecting a fracture in a connected fracture network with uniform fracture conductivity.

v. A producer intersecting a finite-conductivity fracture in a NFR that comprises both finite- and infinite-conductivity fractures yield a dual-porosity

response that may otherwise be absent if the fracture network is assumed to have uniform conductivity.

Overall, this chapter provides novel reference solutions for pressure transient signatures for different fracture conductivities and locations of the producer in fracture networks. It further expands on the results discussed in Chapter 4. Details of the findings of this chapter and the results obtained in the previous chapter will be applied to investigate the pressure data from a Drill Stem Test (DST) in an offshore oil field presented in Chapter 6.

6

CALIBRATION OF DUAL-POROSITY SYSTEMS

6.1 INTRODUCTION

A fundamental challenge in characterising NFR related to the calibration of static and dynamic models to build confidence in the ability of simulation models to estimate hydrocarbon volumes and forecast future production behaviour. Chapter 2 of this thesis highlights the fact that fractures add to the simulation and calibration difficulties because their geology and dynamic flow behaviour are complex and poorly understood. The problem is multi-disciplinary and requires integration of many sources of data for input into and conditioning of the simulation models (Swaby and Rawnsley, 1996) to reduce uncertainties inherent to history-matching and forecasting of production. Hence, the characterisation methods described in Chapter 2 are inadequate to properly evaluate the effect of fracture if used in isolation. Thus, a well-calibrated NFR model is required for realistic prediction of reservoir responses under different production circumstances. The main objective of this chapter is to apply our geological well-testing workflow to calibrate the fracture systems in a newly discovered fractured offshore carbonate reservoir. Using the geoengineering workflow introduced in Chapter 3 and the theoretical insights developed in Chapters 4 and 5, we now apply this knowledge to a real field and investigate how fractures and matrix properties could account for dual-porosity responses identified in the field's well-test data.

6.2 HYPOTHESIS FOR MULTIPLE-POROSITY PRESSURE TRANSIENTS

In Chapters 4 to 5, it was established that some features which trigger the dual-porosity response in well-tests are observed early in the pressure transient or occur near the wellbore (e.g. fracture skin and tight matrix permeability), while others may be observed later or distal to a well (e.g. a well intersecting a low conductivity fracture connected to high conductivity fracture network or open fault). These features may coexist in NFR and influence the pressure transient behaviour of a production well. If early-time and late-time features occur in a

NFR and both impact production at different times with a distinct transition period between them, it is possible to identify more than one dual-porosity V-shape (multiple-porosity, e.g. W-shape). However, where the observable transition between the features' influence on the well is not recognisable or marred, the multiple-porosity response merge to produce a single dual-porosity signal. The latter is also the case where two or more early-time or later-time features exist side-by-side. The above interpretations of the diagnostic fracture flow properties form the basis of our analysis of the real field production test that is presented later in this chapter. To recap the key observations from Chapters 4 and 5, the dual-porosity model response is observed on well-test data from a NFR if a well is:

i. Located in the reservoir matrix adjacent to, but not intersecting, a fracture;

ii. Intersecting a fracture with fracture skin;

iii. Intersecting a fracture surrounded by tight matrix permeability typically below $1mD$.

iv. Intersecting a small unconnected fracture located close to large fractures or fracture network and the ratio between the small unconnected and large fractures is below 0.5;

v. Intersecting a low conductivity fracture connected to high conductivity fracture network or an open fault.

The remaining part of this chapter outlines how the geoengineering workflow is applied to the investigation of the real field data. In addition, we briefly reviewed previous studies on interpreting NFR pressure transient data with multiple-porosity response. First, the background of the drill stem test (DST) data is presented. Next, equiprobable multiple deterministic concepts (Bentley, 2015; Bentley et al., 2017) that all can reproduce the DST data using the geoengineering workflow are explored. Using additional information from the field data (e.g. core analysis, log data and seismic information), these geological concepts are ranked to ensure that the simulation model for the geoengineering workflow remains consistent with the known reservoir data. Subsequently, we calibrated the simulation model with the most plausible concept using the field's pressure data. This provides a better understanding of the main reservoir flow systems. Based on our key findings, we present an alternative and realistic concept on why this particular fractured carbonate reservoir exhibits multiple-porosity response observed in the DST data.

Field X is a fractured offshore carbonate reservoir. An appraisal well in Field X encountered both oil and gas column in layered carbonate and clastic formations. There was insufficient data to characterise the reservoir quality in detail prior to the production test. However, some basic core analysis, log data and seismic data were available. This information suggests that the reservoir is fractured and matrix properties abruptly change in both vertical and lateral directions of the appraisal well. Based on reservoir quality, two rock types, R1 and R2, with a fault or eroded basement in-between were defined. R1 represent the rock type with low matrix permeability ($0.1mD$) while R2 is the rock type with high matrix permeability (100 to $1000mD$). Table 6.1 provides summary of the reservoir and fluid properties of Field X. The appraisal well encountered both oil in the lower carbonate formation (R1) and gas in the upper clastic formation (R2) of the well intervals. Furthermore, examination of the seismic data around the appraisal well indicates that the top of the targeted interval, R1 is probably inclined at around 10° from the top interval, $R2$. This suggests that even though R2 contains the gas column above the perforated interval, it may host movable oil at a lateral distance from the well location.

Oil viscosity (cp)	0.535	
Formation volume factor ($Rbbl/Stbbl$)	1.362	
Total compressibility (psi^{-1})	$1.3789e^{-5}$	
Rock types	$R1$	$R2$
Porosity	$0.01 - 0.12$	0.12
Permeability (mD)	0.1	$100 - 1000$
Perforated interval (ft)	32.8	
Well radius (ft)	0.354	

Table 6.1: Reservoir and fluid properties for Field X.

The DST was performed in the appraisal well, targeting a $10m$ interval of the R1 (Figure 6.1). The resulting transient pressure response (Figure 6.2) can be interpreted at first sight as a triple-porosity (W-shape) response according to (Bourdet, 2002).

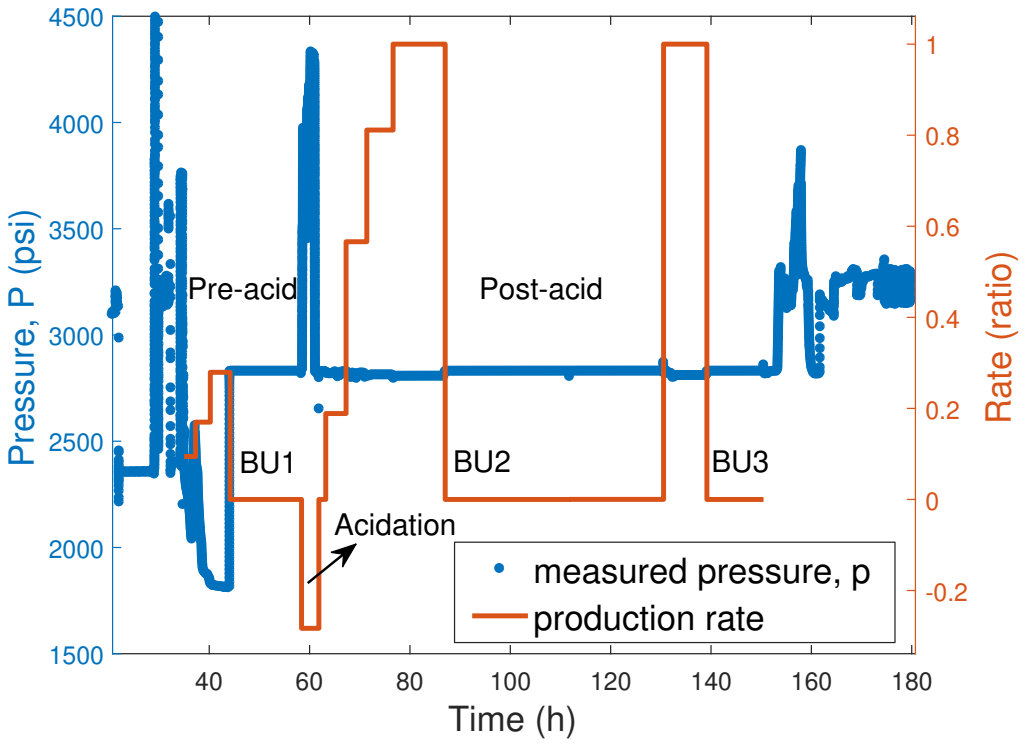

Figure 6.1: Measured pressure and production data from the Drill Stem Test carried out in the appraisal well of Field X. BU denotes build-up.

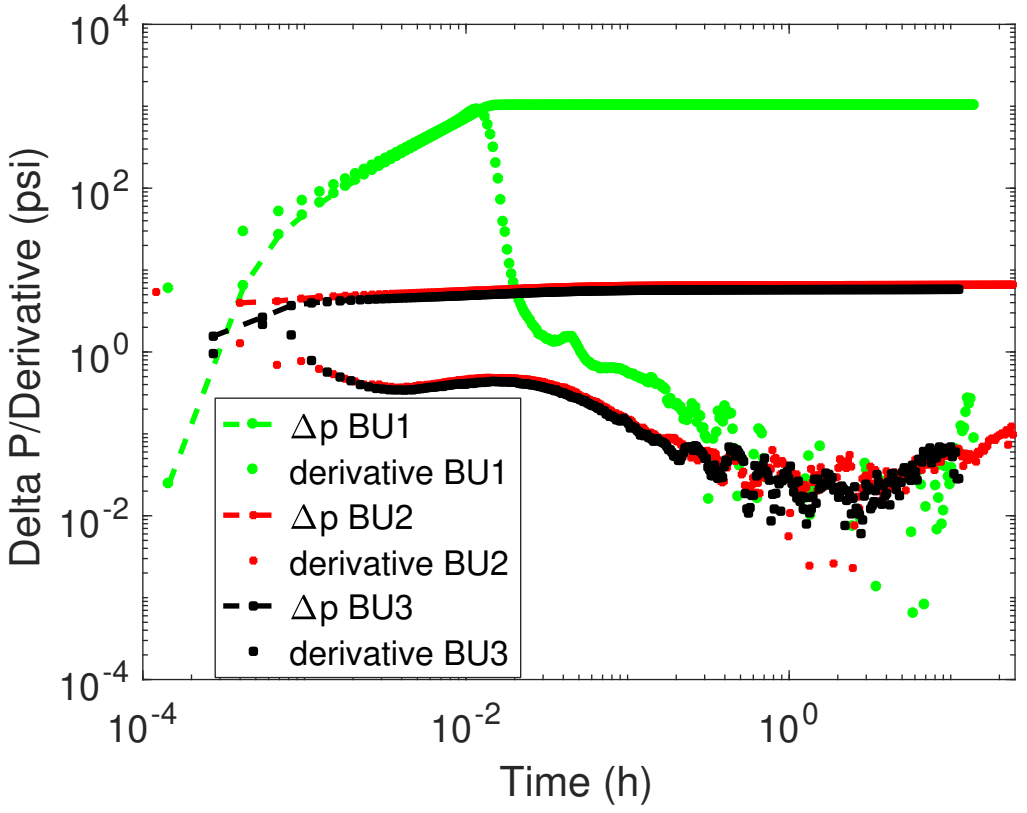

Figure 6.2: Log-log plot of the measured pressure data and their derivatives. An acid treatment was performed after BU1, but before BU2 and BU3.

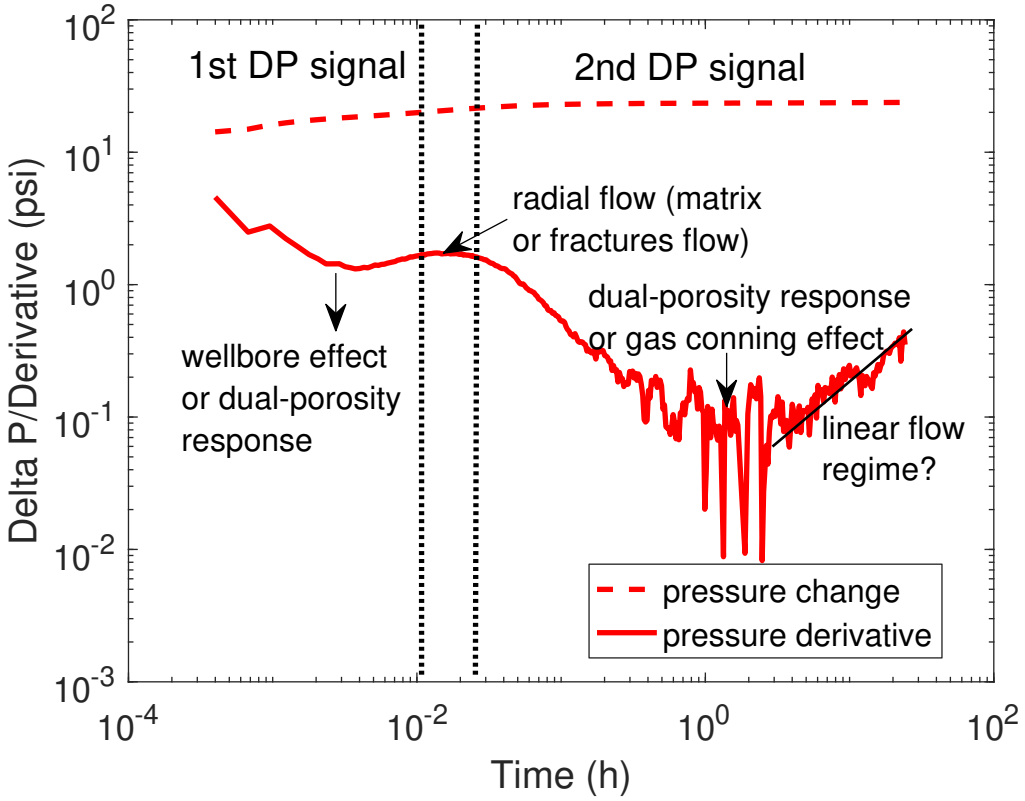

Figure 6.3: Overview of DST data and the initial interpretation for Field X.

Initially, the carbonate interval was tested at low oil rates, see the production profile before build-up 1 (BU1) in Figure 6.1. An acid injection job successfully removed the significant skin observed in Figure 6.1 and Figure 6.2; the post-acid test produced significantly higher flow rates at much lower drawdown in the two following flow periods, see the production profiles before build-ups 2 and 3 in Figure 6.1). These three build-ups were compared to the production test sequence for analysis and interpretation (Figure 6.2). Two of these build-ups (BU2 and BU3) were conducted after acid treatment and exhibit similar trends while the other (BU1) was conducted before the acid stimulation and is considerably different at early time. The longest build-up phase, BU3 (Figure 6.3), was chosen as the reference pressure transient profile for interpretation and analysis because it provide more test data. However, BU1 would also be evaluated for insights and consistency of our interpretation.

In the original interpretation of post-acid build-ups (BU2 and BU3) provided by the operator (Figure 6.3), the first dual porosity V-shape in the pressure derivative was ascribed to the exchange between fractures and matrix (i.e. a dual porosity system), while the second dual porosity signal was attributed to the overlaying gas cap. While accepting this as a plausible inference (Warren, 1993), the purpose of this investigation is to explore another possibility, without considering the gas effect. Thus the result presented here can only be considered an one plausible interpretation as the potential impact of gas coning into the well

or gas production through the fracture network is discounted. The investigation employed the findings from Chapters 4 and 5 that clearly show which reservoir and fracture features that cause the dual-porosity signature. Considering that the field DST profile resembles an asymmetric triple-porosity response (W-shape) associated with complex fractures and matrix interaction in a reservoir system, we review existing studies on multi-porosity responses from NFR.

6.4 PREVIOUS STUDIES ON MULTIPLE-POROSITY SYSTEMS

Clossman (1975) extended the Warren and Root (1963) dual-porosity model to model a fractured reservoir with two distinct matrix systems as a triple-porosity model. This model's assumptions were similar to Warren and Root's (1963) model, including uniform matrix block size and shape. However, unlike the dual-porosity model, the matrix comprised two rock types with distinct petrophysical properties ("good" and "poor"). Cinco-Ley et al. (1985) and Belani and Jalali (1988) related the multi-porosity response to the effect of multiple matrix block sizes and their distribution within an NFR. As a result, they modelled the fractured reservoirs considering variable matrix block sizes of uniform petrophysical properties to investigate the pressure transients under both PSSIF and TIF conditions. Motivated by observations in real field well-tests behaviour, Abdassah and Ershaghi (1986) developed a triple-porosity model to represent NFRs whose pressure transients defy adequate explanation by the dual-porosity models. They supposed that the anomalous changes in flow regime during matrix-dominated flow of the transition period may be a result of matrix blocks exhibiting distinctly different petrophysical properties. Consequently, their triple-porosity models comprise a fracture network with homogenous properties interacting with two groups of matrix blocks under transient inter-porosity flow conditions. Similar to Cinco-Ley et al. (1985), the authors observed that the pressure transients of a triple-porosity system with transient inter-porosity flow resemble the classic dual-porosity model behaviour. Furthermore, they concluded that the multi-porosity system may not be distinguishable from the dual-porosity model behaviour when viewed on the log-log plot but may be visible on the semi-log plot. Later publications (e.g., Bourdet, 2002; Corbett et al., 2012) stated that the triple-porosity W-shape is generally attributed to fractured carbonate reservoirs (Chen, 1989) when simulated under pseudo-steady state inter-porosity flow. However, this pressure behaviour is often not observed when fractured reservoirs are simulated with transient inter-porosity flow simulation conditions. For this reason, the later publications stated that triple-porosity response is perhaps unlikely to be identified in well test data from NFR producing under TIF, even for highly heterogeneous and fractured carbonate reservoirs. This is related to

the fact that realistic flow exchange between fractures and matrix always occur in a transient state (Gringarten, 1984; Wei et al., 1998; Kuchuk and Biryukov, 2014). Corbett et al.'s (2012) study aimed to investigate under which conditions the triple-porosity W-shape response can occur in fractured carbonates reservoirs and to determine the key reservoir parameters that control this behaviour. They observed that even for the specifically designed and well-defined triple-porosity systems, only a number of cases reproduced the classical dual-porosity V-shape and no simulations showed the triple-porosity W-shape.

Al-Ghamdi and Ershaghi (1996), on the other hand, developed a different concept for the triple-porosity model. Their models consist of two fracture systems (macro fractures and micro fractures) with one matrix type. This is directly opposite to the alternative concept that consists of one fracture system and two matrix types. Figure 6.4 illustrates the two types of triple-porosity systems reported in the literature. The first type comprised one fracture set with two matrix block sizes. Figure 6.5 shows the theoretical well-test response for this type of reservoirs producing under PSSIF response. The second type consist of two fracture sets with uniform matrix blocks.

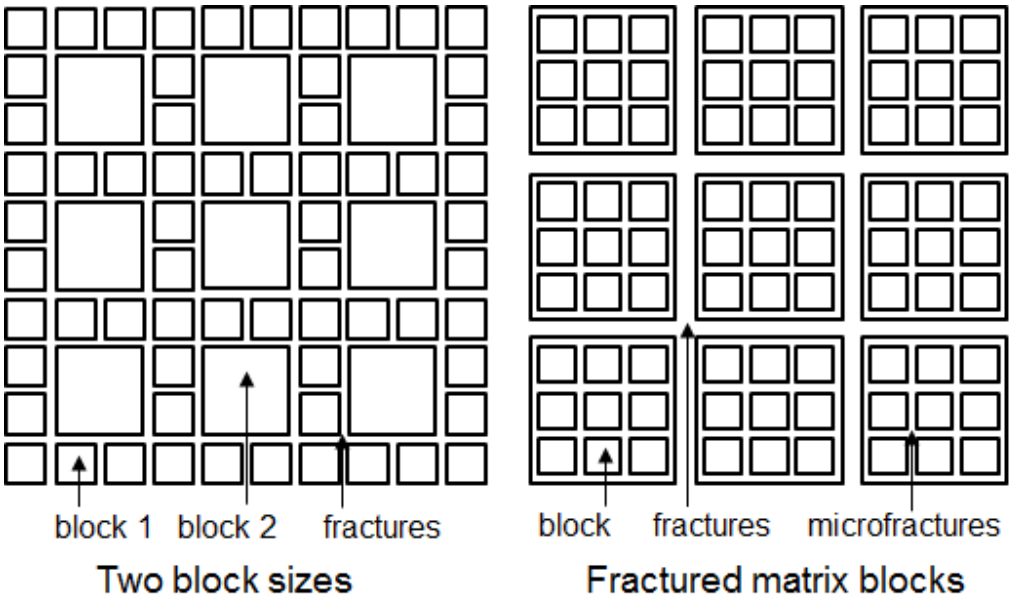

Figure 6.4: Two types of triple porosity systems showing one fracture set with two matrix block sizes (a) and two fracture sets with a uniform matrix blocks (b). After Bourdet (2002).

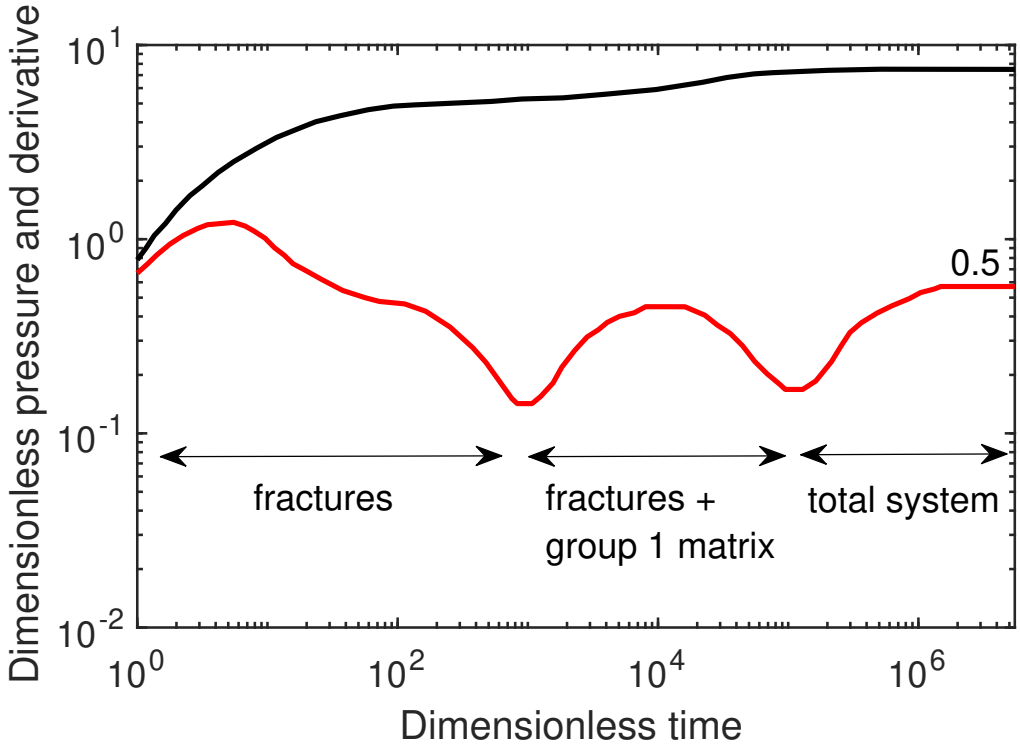

Figure 6.5: A theoretical triple porosity well-test response for the reservoir type shown in Figure 6.4a with pseudo steady state inter-porosity flow. The black line represents pressure and red line the pressure derivative. The matrix "Group 1" corresponds to the small size matrix blocks. After Bourdet (2002).

6.5 NUMERICAL SIMULATIONS AND RESULTS

6.5.1 *Equiprobable geological concepts*

We employed the findings from Chapters 4 and 5 to investigate under which conditions the key reservoir features that are known to generate the classical dual-porosity response could also result in a multi-porosity response. This would allow for the calibration of the reservoir model with DST data and provide insight into Field X fractures and matrix flow systems. Using this prior knowledge, we designed five equiprobable geological scenarios (Figure 6.6) that could potentially produce a pressure transient response that is similar to that of Field X, i.e. indicates a multi-porosity behaviour (Figure 6.3). Apart from the first scenario, all the geological concepts consider a tight matrix permeability ($< 1mD$) around the well location. This is consistent with matrix permeability calculated from core analysis for R1 described earlier. The reservoir simulation model has $200X200X10m$ block consisting of connected fractures with $20X20X10m$ matrix blocks separating individual fractures. Scenarios are also considered where small, (un)connected fracture that are $7.5m$ long are present. A brief description of the scenarios presented in the Figure 6.6 is given below.

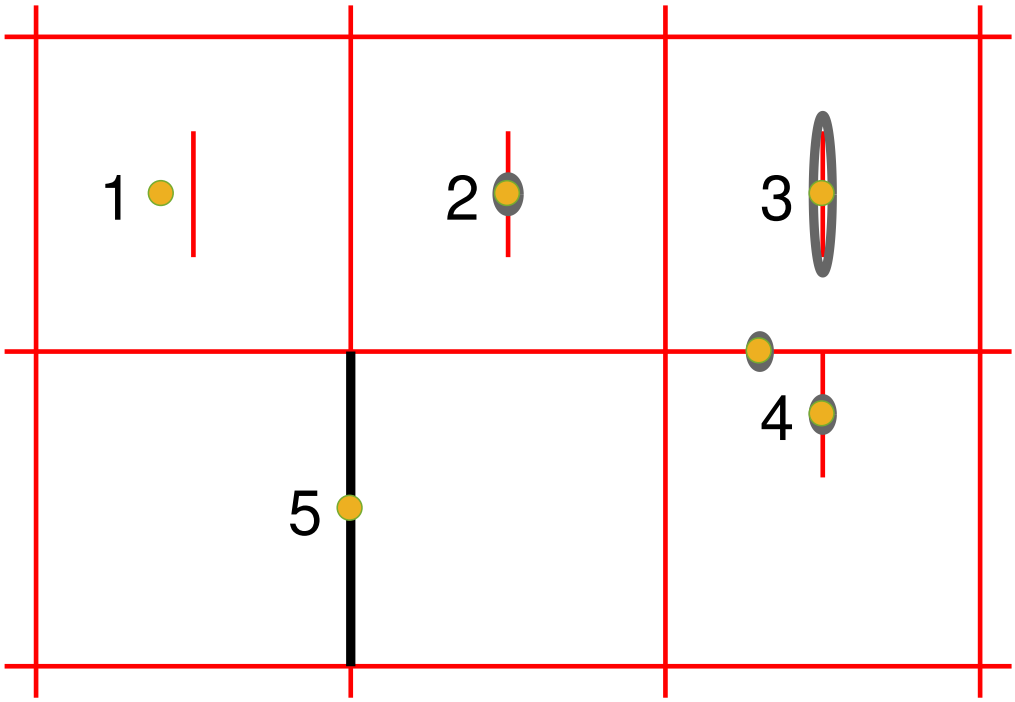

Figure 6.6: Five equiprobable geological scenarios that could potentially generate pressure transients that are similar to those observed in Field X (Figure 6.3). The illustration zooms in on well locations. The connected fracture system is contained in a $200X200X10m$ reservoir block with $20X20X10m$ matrix blocks separating individual fractures.

Scenario 1: In this scenario, the well is located in the matrix adjacent to a small, unconnected fracture near a larger fracture network. Two matrix cases - high ($10mD$) and low ($1mD$) are considered. The simulated pressure response for this scenario is shown in Figure 6.7. In this case, the pressure response is controlled by the matrix properties until the pressure front that reaches the well is perturbed by the nearby small fracture. The conductivity contrast between the matrix and the small fracture leads to the occurrence of the first dual-porosity signal (Cinco-Ley et al., 1976; Abbaszadeh and Cinco-Ley, 1995). The figure also shows that the dual-porosity response can be observed for both, high ($10mD$) and low ($1mD$) matrix permeability cases. The second dual-porosity signal occurs because of pressure depletion from the small, unconnected fracture, the matrix properties, and the nearby large fracture network (see Chapter 4 for details). The second dual-porosity response is observed for different distances (e.g. $1m$ and $5m$) of separation between the small, isolated fracture and the surrounding fracture network.

Scenario 2: In this scenario, a well with completion skin intersects a small, unconnected fracture. The simulated pressure response for this concept is shown in Figure 6.8. The first dual-porosity signal results from the skin effect in the well. The second dual-porosity signal is due to same processes described above for Scenario 1.

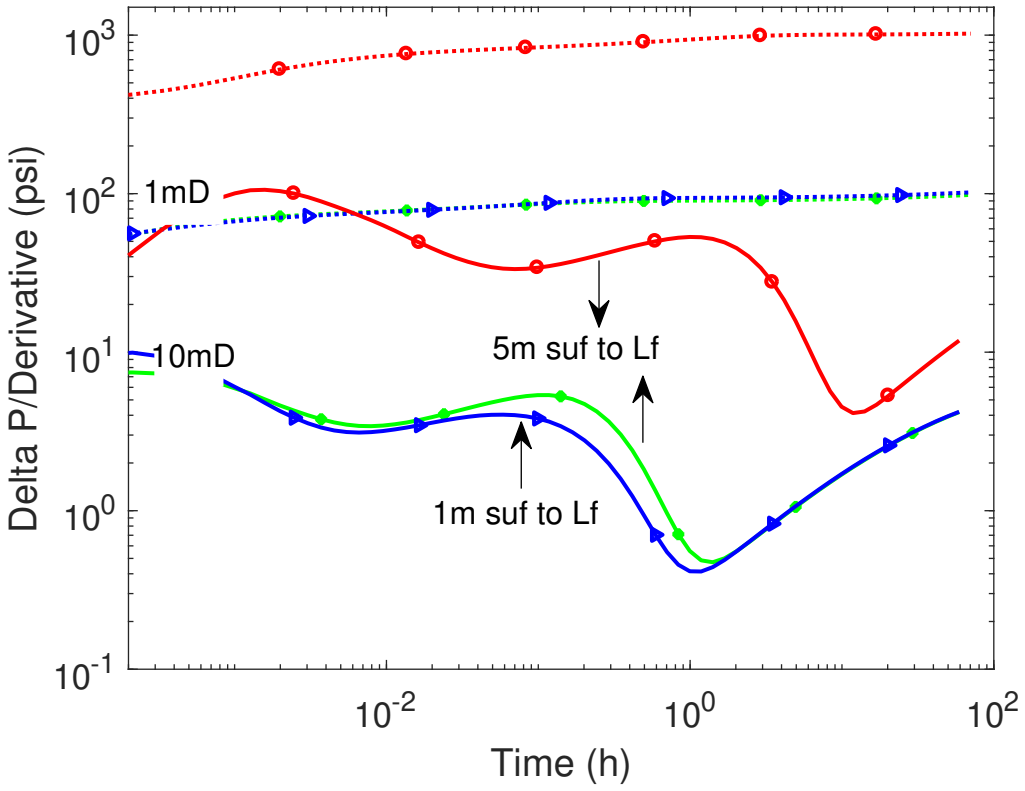

Figure 6.7: Simulated pressure response for Scenario 1. The dotted and solid lines represent changes in pressure and the corresponding pressure derivatives, respectively. $1m$ and $5m$ denote the distance between the small, unconnected fracture (suf) and the nearby, larger fracture network (Lf).

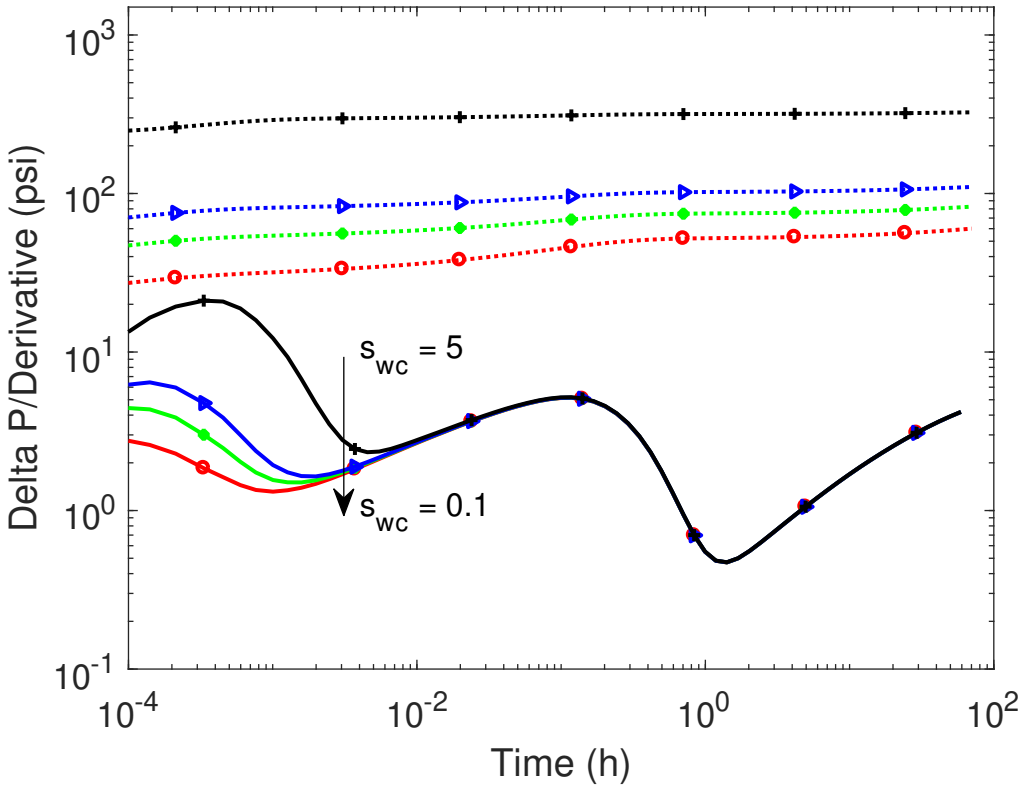

Figure 6.8: Simulated pressure response for Scenario 2. S_{wc} denotes the well completion skin.

Scenario 3: In this scenario, a well intersects a small, unconnected fracture with fracture skin. The simulated pressure response for this scenario is shown in Figure 6.9. The first dual-porosity signal is caused by the fracture skin (detailed in Chapter 4). The second dual-porosity signal is due to same processes described above for Scenario 1.

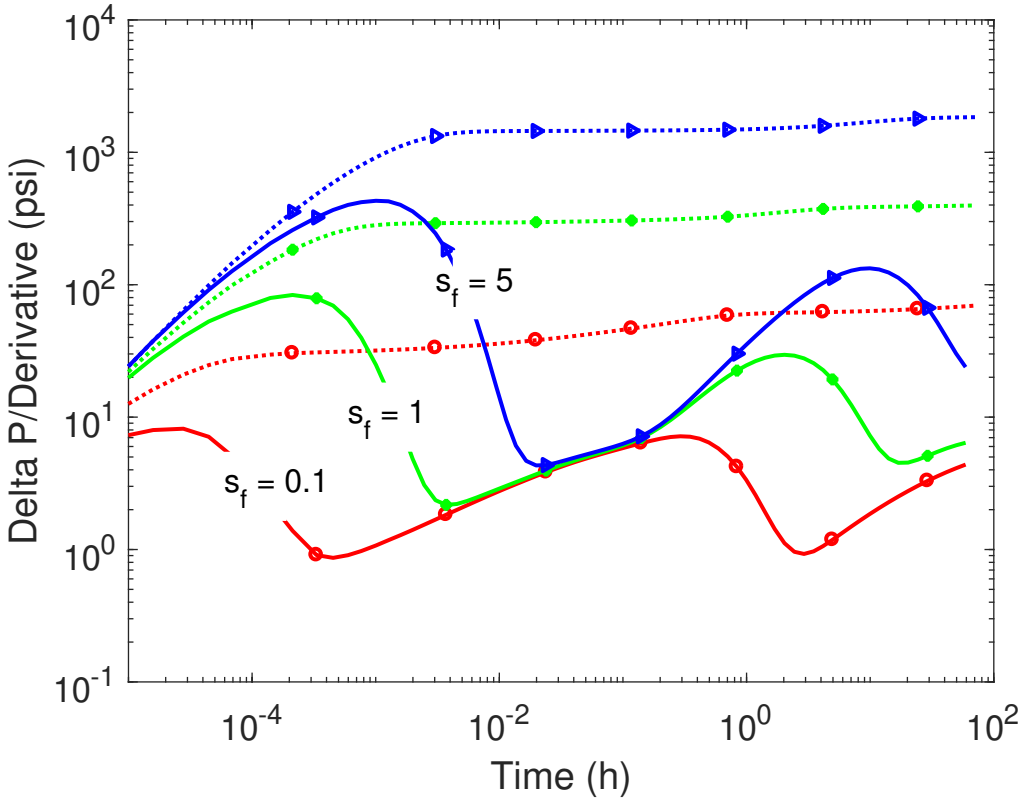

Figure 6.9: Simulated pressure response for Scenario 3. S_f denotes the fracture skin.

Scenario 4: In this scenario, a well with completion skin intersects a connected fracture network. The simulated pressure response for this scenario is shown in Figure 6.10. The first dual-porosity signal (Figure 6.10) is caused by the well skin (S_{wc} of 0.1 to 5). The second dual-porosity signal results only from the contrast between the matrix and the overall fracture network since all the fractures in the simulation model are connected. See details for the case of a well intersecting fractures surrounded by low matrix permeability in Chapter 4.

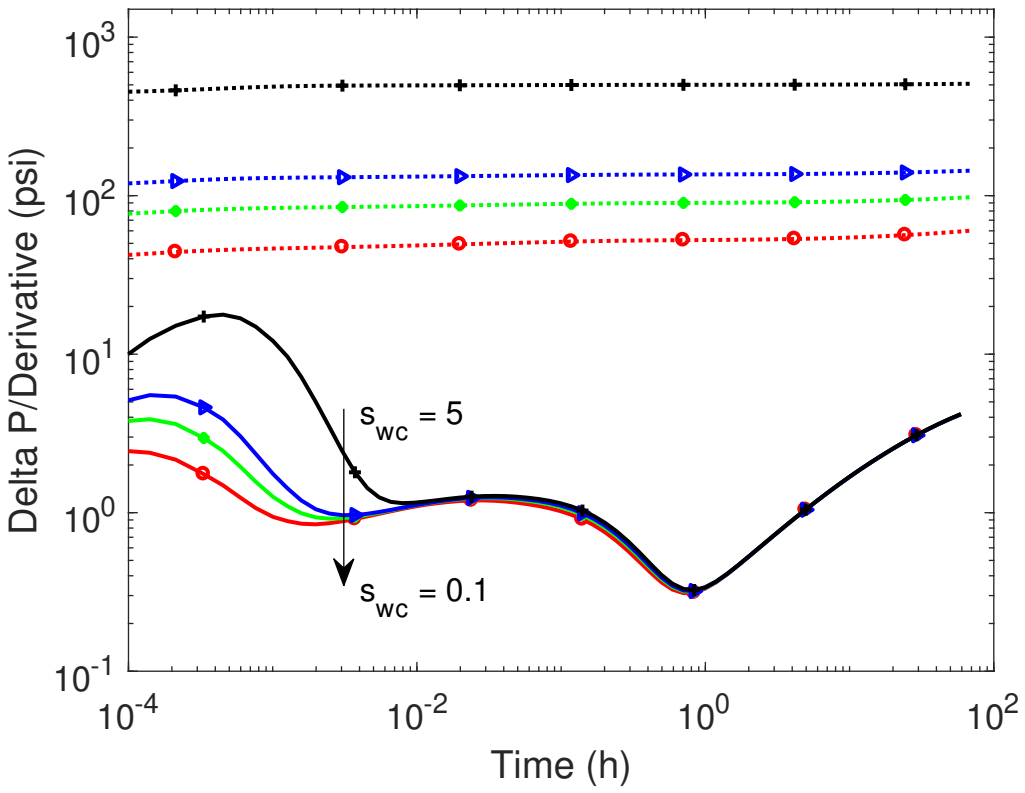

Figure 6.10: Simulated pressure response for Scenario 4. S_{wc} denotes well completion skin.

Scenario 5: In this scenario, a well intersects a finite-conductivity fracture that is connected to an infinite-conductivity fracture network. The simulated pressure response is shown in Figure 6.11. The figure also shows sensitivity to matrix permeability. The first dual-porosity signal results from the contrast between the finite-conductivity fracture and the surrounding matrix. The simulated pressure response for the case of a well intersecting fractures surrounded by low matrix permeability is discussed in Chapter 4. The second signal is due to conductivity contrast between finite- and infinite-conductivity fractures (discussed in Chapter 5). A finite-conductivity fracture near an open and high conductive fault can effectively reproduced the observed pressure response. Al-Thawad et al. (2001) presented similar pressure transient for a well intersecting a finite-conductivity fracture near an infinite-conductive fault in Ghawar Field Saudi Arabia. However, the use of infinite-conductivity fractures here is favoured in view of other field data as the possible fault near the tested well can better be described as an unconformity, which could be a fault or an eroded basement). Thus, a well intersecting a finite-conductivity fracture that is connected to infinite-conductivity fractures is considered more appropriate in this case.

The investigation of the different concepts presented indicates that the multiple dual-porosity response observed in well test data can result from different geological scenarios. This underlines the lack of uniqueness issues with well test data and the need to complement this data with other sources. Next, we elimi-

nate the geological scenarios that are not consistent with other information and data for Field X to ensure that the final model scenario is in agreement with the general geological understanding of Field X.

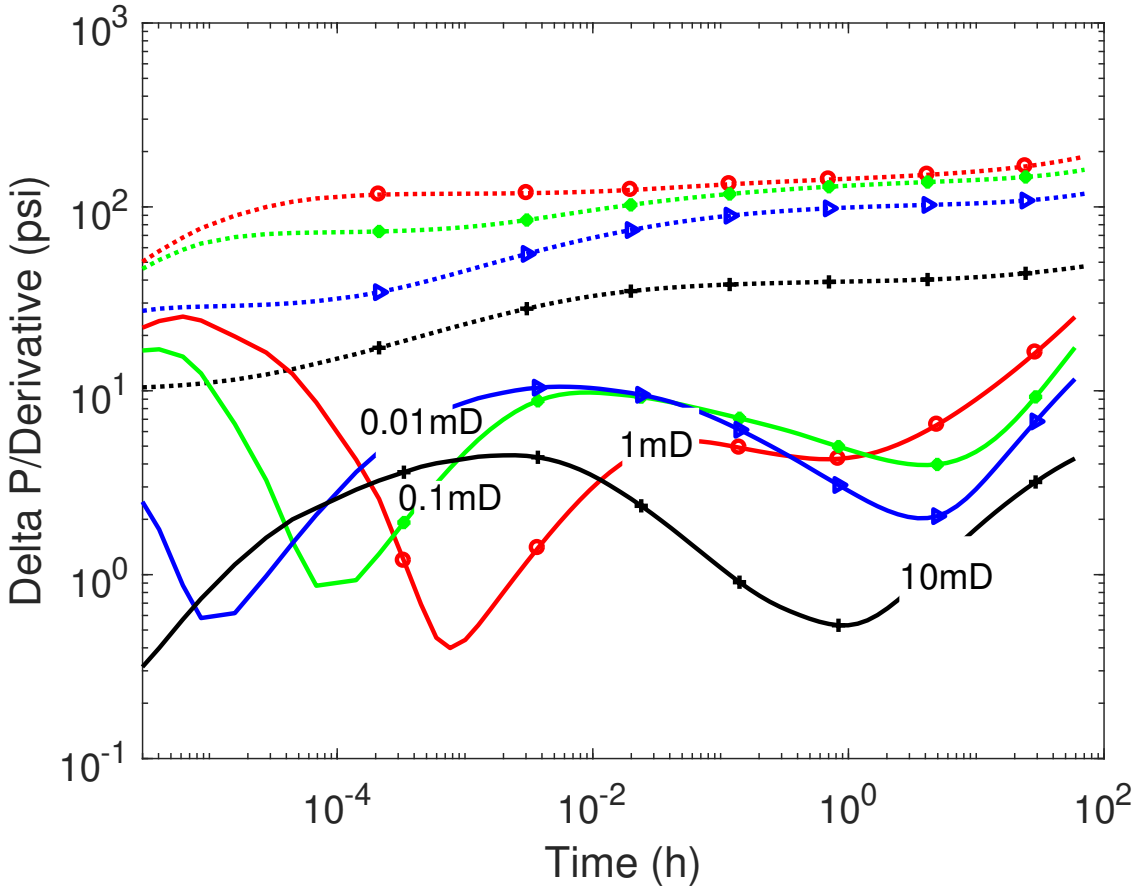

Figure 6.11: Simulated pressure response for Scenario 5 with a well intersecting a finite-conductivity fracture and for different matrix permeabilities.

6.5.2 *Determination of the most plausible geological scenario*

Examination of core and image logs shows that the appraisal well intersects fractures that are oriented sub-vertically. This observation rules out Scenario 1, where it is assumed that the well is located in the matrix adjacent to, but not intersecting any, fractures. The radial flow regime after the first dual-porosity signal (Figure 6.3) also indicates an unrealistically high matrix permeability compared to the core samples permeabilities, further suggesting that this scenario can be ruled out.

The impact of well completion skin (see Scenarios 2 and 4), observed in BU1 (Figure 6.2) after the well workover was also ruled. BU2 and BU3 show that the acid treatment during the workover removed any skin effect caused by the well. Furthermore, a fracture skin effect (Scenario 3) was ruled out for similar reasons as the skin caused by the well because BU2 and BU3 conducted after well workover do not show any effect of skin. Moreover, there are no data to

support that fracture skin existed before the well workover. To this end, we hence consider Scenario 5 as the most plausible geological scenario for Field X (Figure 6.6). Thus, further detailed investigation considers only this particular scenario.

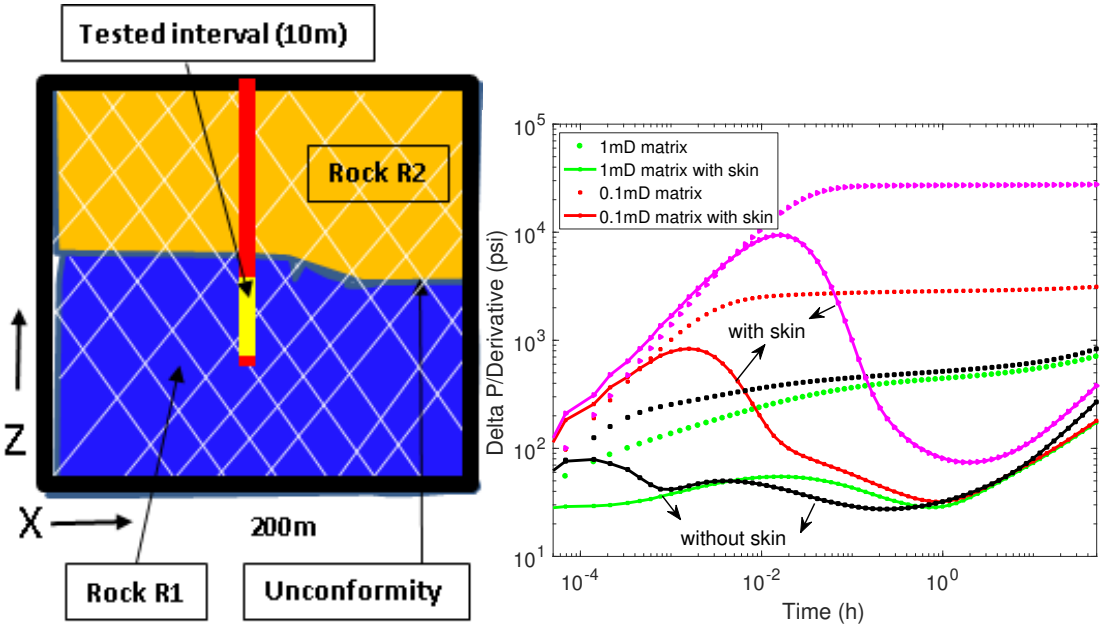

(a) (b)

Figure 6.12: Conceptual geological model showing the well that is testing an interval where rock-type R1 is present and fractures are abundant (a), and simulated pressure derivatives showing effect of matrix permeability and well completion skin (b).

To further test the validity of Scenario 5, we ran a number of sensitivity considering a range of matrix permeability values that have been estimated from the Field X's basic core data. We simulated several models using data for rock type R1, which is present in the interval that was tested during the DST (Figure 6.13a). R1 has $0.1mD$ matrix permeability and the permeability ranges for R2 is from 100 to $1000mD$ in the core. We hence assumed constant and uniform matrix permeabilities including those for R2. We observe that only models with matrix permeability below $1mD$ yield a dual-porosity signal at early time (Figure 6.12b). Figure 6.12b also shows results of sensitivity analysis considering cases where completion skin is present in the well for comparison with BU1 conducted before the well workover. If skin is assumed to be present, the simulated pressure responses are similar to the observed pressure response prior to the acid treatment (Figure 6.2, BU1). Thus, our simulation model can reproduce the DST responses observed before and after the acid treatment. This provides further confidence that the selected Scenario 5 is most plausible for the available Field X's data.

Next, we tested the case where the well produces from two reservoir intervals, i.e. from R1 and R2 (Figure 6.13). This allows us to evaluate the impact of the upper interval, which contains gas and where R2 is located, on the pressure

response. Fractures in this model cut across both layers and only bound by the reservoir model thickness. Thus, flow can occur across the two rock types at the interface between R1 and R2 and/or through the fracture network. However, none of these models reproduced the dual-porosity signature observed at early time in the well test. This is probably because of R2 has a high permeability that dominates flow and reduces the fracture-matrix permeability contrast.

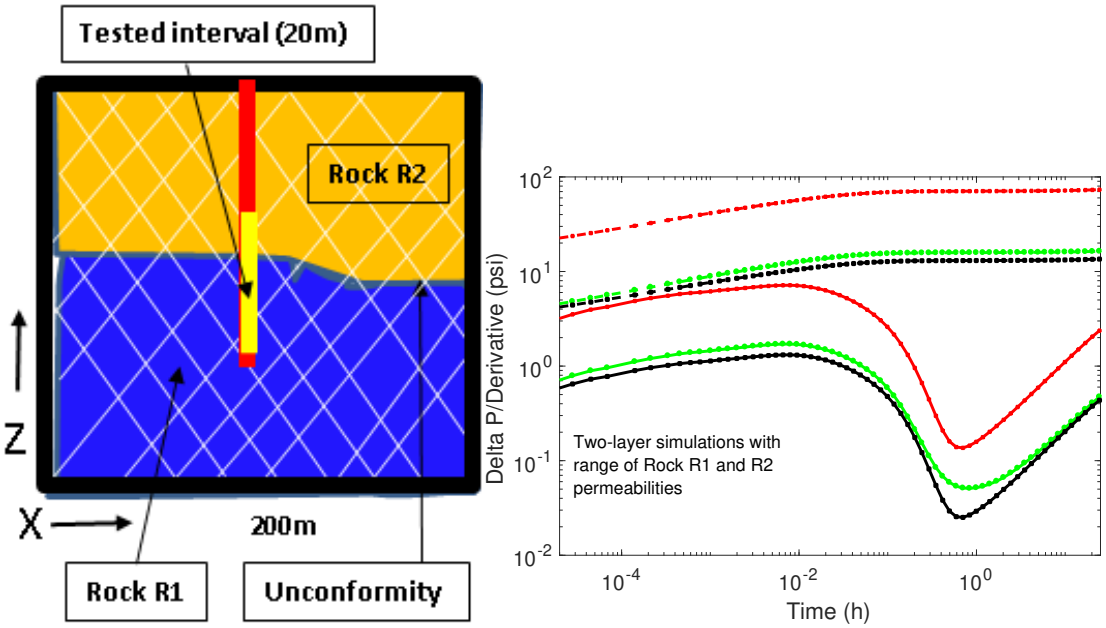

Figure 6.13: Conceptual geological model with both R1 and R2 tested intervals (a) and the simulated pressure response (b).

All simulated cases (with only R1 or with both R1 and R2 present) reproduced the second dual-porosity response (Figure 6.12 and Figure 6.13) if fractures with different conductivities are considered and if the well intersects the fractures with finite conductivity (see Figure 6.15 for the fracture network configuration). These results support the hypothesis that only R1 is contributing to flow in the vicinity of the well.

In Figure 6.14, Set 1 and Set 2 represent finite- and infinite-conductivity fractures respectively. The simulations results where the presence of the two fractures sets are located in a single rock-type R1 combine two processes (Figure 6.14 and Figure 6.15) that independently can create a dual-porosity response, namely (i) a well intersecting a fracture surrounded by tight matrix permeability of less than $1mD$ (discussed in Chapter 4), and (ii) a well intersecting finite-conducting fractures (Set 1) connected to infinite-conductivity fractures (Set 2) (discussed in Chapter 5) or an open fault. The dual-porosity signature due to (i) is usually observed at early time (Figure 6.15, see Wells 1 and 2 with $< 1mD$ matrix permeability) during the well test while (ii) occurs later in time (Figure 6.15, see Well 3

with $> 10mD$ high permeability and fractures with different conductivities). In both cases, the well intersects fracture(s).

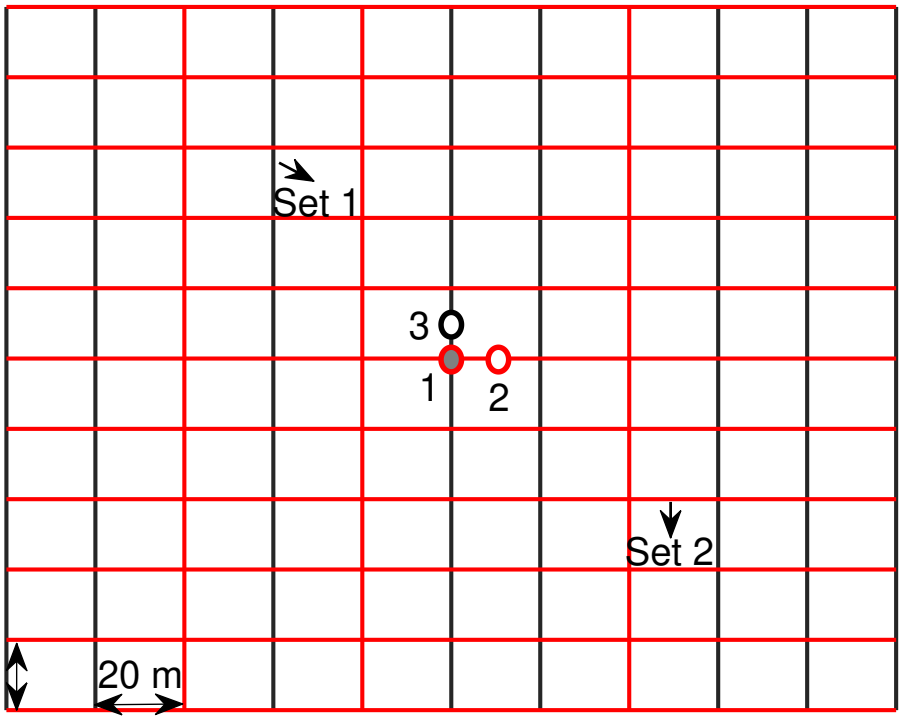

Figure 6.14: Scenario 5 showing the fracture geometry with a well intersecting both finite-conducting (Set 1) and infinite-conductivity (Set 2) fractures (Well 1), only Set 2 fracture (Well 2) and only Set 1 fracture (Well 3).

We hypothesise that the coexistence of these two factors in an NFR could, under certain conditions, result in a multi-porosity response during a well test (Figure 6.15, Well 3 with $< 1mD$ and fractures with different conductivity). As a result, we infer that the dual-porosity response observed at early time in the DST data could represent the exchange between the finite-conductivity fracture set and the surrounding low-permeability ($0.1mD$) rock-type R1 (discussed in Chapter 4). The second dual-porosity signature may result from the exchange between the finite- and infinite-conductivity fracture sets (discussed in Chapter 5). If the matrix permeability surrounding the well is high (Figure 6.15, Well 3 with $> 10mD$ matrix permeability and fractures with different conductivity) or the fractures properties are assumed to be uniform (Figure 6.15, Well 3 with $< 1mD$ matrix permeability and fractures with uniform conductivity), only the dual-porosity effect related to one of the above causative factor would be observed. Furthermore, if the matrix permeability is high and the fracture network is assumed to be uniform, the dual-porosity signature is not observed (Figure 6.15, Well 3 with $> 10mD$ matrix permeability and fractures with uniform conductivity).

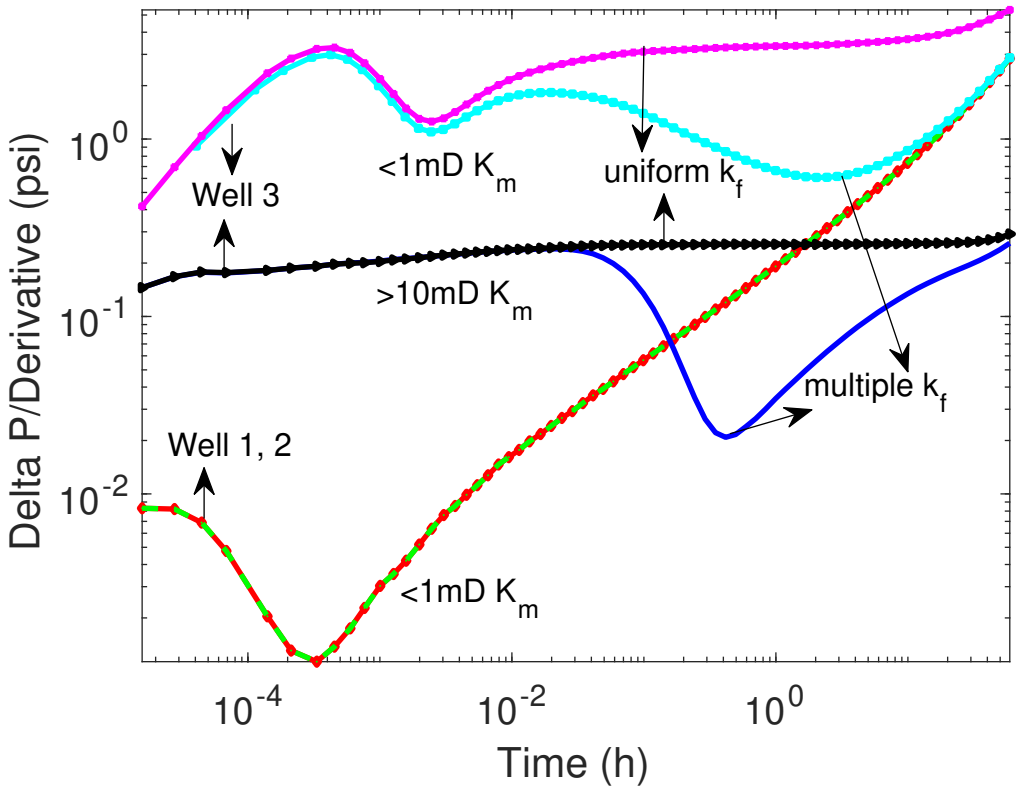

Figure 6.15: Simulated pressure responses of the model configuration and well locations depicted in Figure 6.15. k_m denotes the matrix permeability. uniform k_f and multiple k_f denote fractures with uniform and different conductivity, respectively.

6.6 CALIBRATION OF THE RESERVOIR MODEL

Now that we are able to reproduce the observed pressure transient qualitatively using the model Scenario 5, we performed further sensitivity studies to calibrate the model parameters until a good, quantitative agreement between the simulated and observed DST response could be achieved. Since we have obtained an estimated value of the matrix permeability for R1 from the core data and this value agrees with the DST response during the initial sensitivity analysis (Figure 6.12), we decided to keep this parameter constant for the rest of the analysis. Therefore, to calibrate the model, only the fracture properties and wellbore parameters are changed. To provide a visual aid for the calibration of the simulation model, we overlaid the simulated pressure response with the observed DST data on a log-log plot (Figure 6.16) and marked the limits between the two dual-porosity signatures on the measured data. Our goal at this stage is to reproduce the magnitude of the dual-porosity V-shapes (starting with the first signature) and the stabilisation limits between the signatures identified from the measured data.

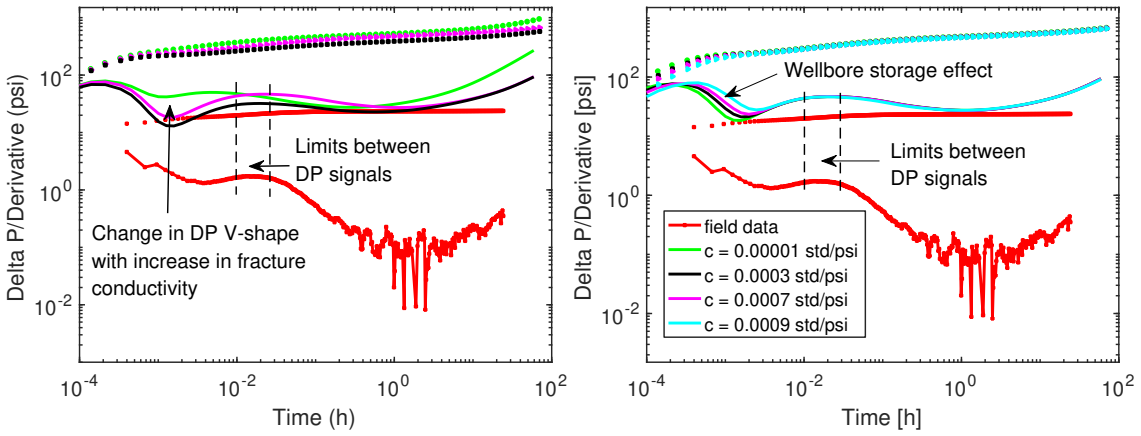

Figure 6.16: Simulated pressure response showing sensitivity to fracture aperture and conductivity of the finite-conductivity fracture set, which is intersected by the producer (a) and the sensitivity to the wellbore storage (b).

We observed that the main factors affecting the pressure response at early time are wellbore storage, matrix permeability, and the properties of the finite-conductivity fracture set that is intersected by the well. The contrast between the matrix permeability and the permeability of the fracture intersected by the well is observed to be the most important factor impacting the depth and extent of the first dual-porosity signature V-shaped. Accounting for all of the above-mentioned factors in our simulation model, we were able to simulate pressure transients that reflect the observed pressure response relative to elapsed time for the first dual-porosity signature (Figure 6.16b).

However, the simulated pressure drop is high ($>$ 1 and $>$ 2 orders of magnitude for the first and second dual-porosity V-shape respectively) compared to the observed one (Figure 6.16). We hence tested different fractures properties, including lateral extent and volume of the fracture network. Figure 6.17 shows how changes in fracture half-length x_f impact the simulated pressure derivative response. Note that an increase in x_f also increases the fracture volume and fracture conductivity. Figure 6.17 shows that any further increase in fracture volume or in the lateral extent of the fractures shifts the second dual-porosity response to later times, which is not observed in the DST pressure response. However, simulations where we assume that x_f is $200m$, twice as large compared to the initial reservoir model where x_f is $100m$ appeared to improve the simulated pressure response relative to the DST data. Hence all subsequent simulation work with $x_f = 200m$.

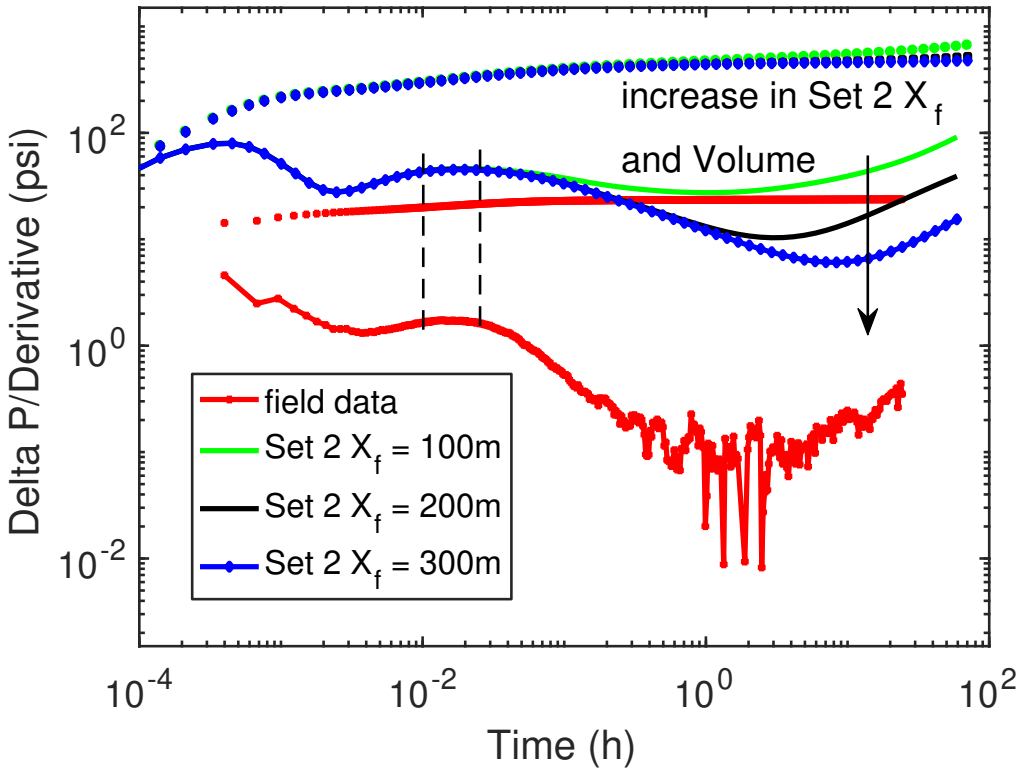

Figure 6.17: Simulated pressure response showing the sensitivity to the fracture half-length X_f.

Since the simulated pressure drop is still high (> 1 and about 2 orders of magnitude for the first and second dual-porosity V-shape respectively) compared to the observed one, we now test parameters that can help to increase well productivity index while honouring the matrix permeability and fluid properties in Field X. The parameters include the degree of crosscutting of fractures with infinite conductivity that connect the infinite-conductivity fractures together and the distance of the fractures with infinite conductivity to the producer. Figure 6.18 shows that a significant change in pressure response emerges if two fractures with infinite conductivity crosscut and connects the other fractures with infinite conductivity to each other. However, only slight additional changes in pressure derivatives can be observed if the number of the fractures with infinite conductivity that are connecting the other infinite-conductivity fractures in the reservoir model is further increased to ten. The distance of the producer to the infinite-conductivity fractures was also observed to impact the simulated pressure response. A short separation distance between fractures and the well yields higher production rates and a smaller decrease in bottom-hole pressure; a larger separation distance has the opposite effect. Thus, changing the degree of interconnection between fractures with infinite conductivity and the distance of these fractures to the producer further reduce the contrast between the pressure drop in the simulation model using Scenario 5 and the DST data (Figure 6.18). However, this simulation model containing rock-type R1 and the two fracture

sets did not produce pressure response that agrees with the observed pressure response.

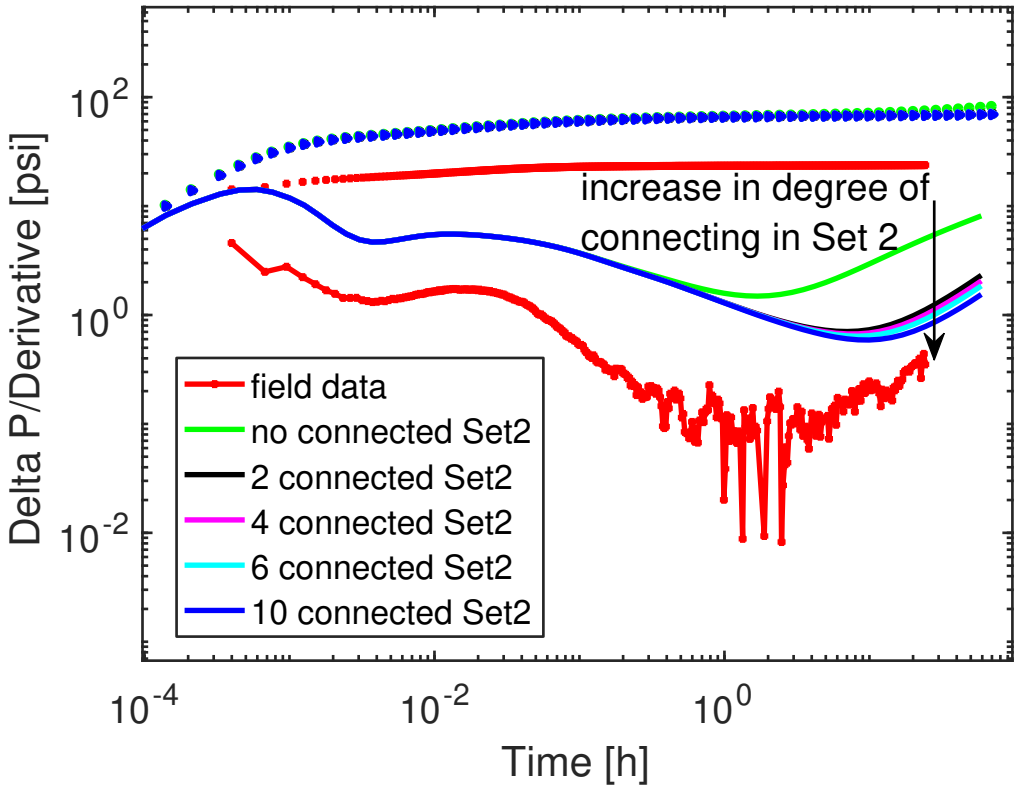

Figure 6.18: Simulated pressure response showing the sensitivity to the degree of fracture connectivity in the infinite-conductivity fracture set (Set 2) using Scenario 5 model.

Next, we investigated the possibility if rock-type R2 can contribute to reservoir flow even if there is no immediate production from R2 in the near-wellbore area because R2 was not perforated in the DST. As noted before, seismic data indicates that top of R1 is inclined by around 10° from *R*2 and separated by an unconformity (fault or eroded basement). Hence the gas cap present in R2 in the vicinity of the appraisal well is likely absent away from the well and, therefore, oil may be produced from R2 at some distance away from the well, flowing through the fractured interval containing R1 towards the well during the DST. To test this hypothesis, we added an interval containing the properties of rock-type R2 at a lateral distance from the well (Figure 6.19a). However, due to the limitation of the simulation grid to model inclined layers in vertical direction, the simulation model (Figure 6.19b) only account for the lateral distance of the *R*2 from the well. In addition, the orientation of the unconformity may not be undulating resulting to uneven (more or less) distances between *R*2 and the well. While the geometry and size of the interval containing R2 are uncertain in principle, simulation results show that these uncertainties have little impact on the pressure response compared to the distance at which the matrix properties change from R1 to R2 away from the producer, already accounted for in

the simulation. We therefore performed a sensitivity analysis to analyse how the pressure response varies as a function of the distance at which the rock-types change from R1 to R2 laterally away from the well. The results in Figure 6.20a shows that the match between the simulated and observed pressure responses can be greatly improved when rock-type with R2 properties is added to the Scenario 5 model as described above. The high matrix permeability of R2 provided further pressure support to the producing fractures and reduced the pressure drop in the well. In addition, we were able to further tune the distance between the producer and the infinite-conductivity fracture set, which helped us to obtain a good match between the simulated pressure response and the DST data. We observed that the simulated production rates and the pressure responses depend on the location of the producer compared to the infinite-conductivity fracture set and rock-type R2. Based on these simulation results, we converged to the final reservoir model which now contains two sets of fractures (Set 1 and Set 2) and the two rock-types (R1 and R2). Figure 6.20b compares the simulated pressure transients for the different variations for Scenario 5 with the observed pressure data. Clearly, a model where both fracture sets and both rock-types are present, but R1 transitions into R2 away from the well, gives the best match. Al-Thawad and Jamiolahmady (2014) presented an example from Ghawar field where a well intersect a fracture in an asymmetric reservoir with sandstone and carbonate rock properties.

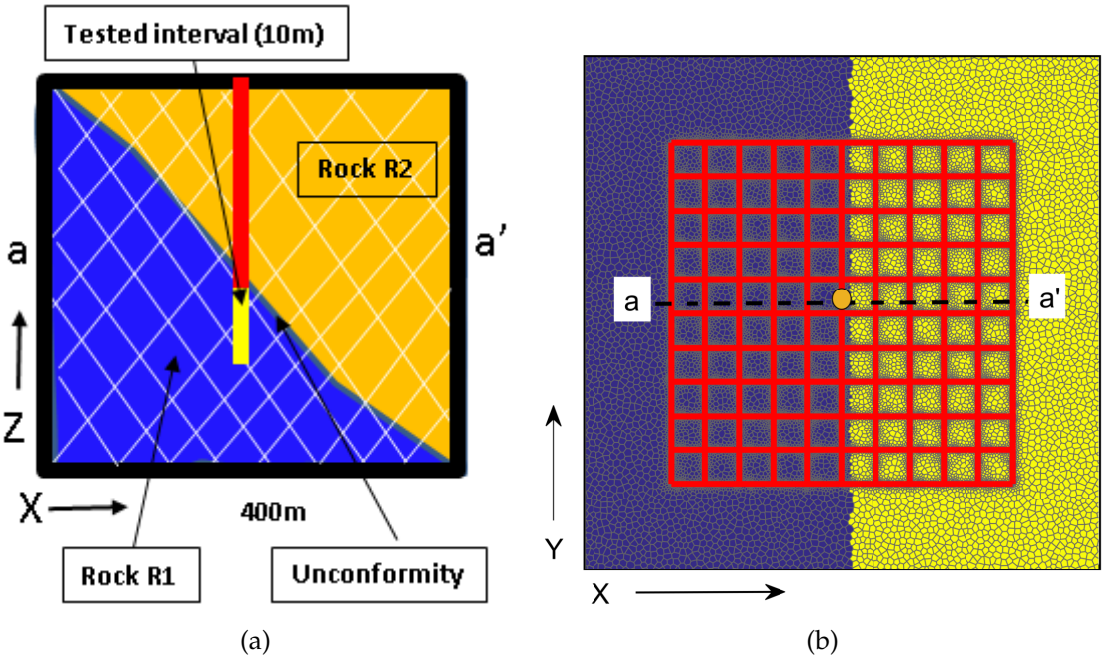

Figure 6.19: Final simulation model showing the cross section of the conceptual geological model (a) and the map view of the simulation model corresponding to the top of DST tested interval (b). The blue and yellow sections represent rock-types R1 and R2 respectively. The red line indicates fractures and a and a' where the cross section is taken.

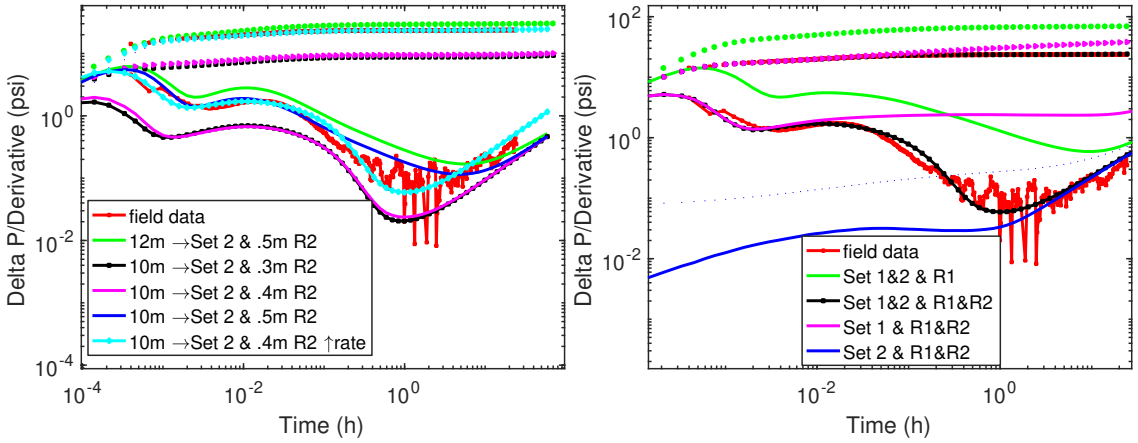

(a) (b)

Figure 6.20: Simulated pressure response showing the sensitivity to distance between the producer and the infinite-conductivity fracture set (Set 2) as well as rock-type R2 (a) and the four different geological scenarios that consider the presence of different fracture sets and rock-types (b). Note that all parameters in (b) are constant, only different geological features are included or excluded.

6.7 INTERPRETATION OF THE FIELD RESERVOIR FLOW SYSTEMS

Applying the geoengineering workflow presented in Chapter 3 and the findings from Chapters 4 and 5, we were able to produce a simple reservoir model that matches the observed pressure response for Field X unequivocally. This reservoir model provides a useful approximation for the likely field condition but does not require the complexity of a stochastic, high-resolution 3D model (Bentley 2015). This basic reservoir model allows us to decipher the main fracture systems and the supporting matrix properties that account for the flow response in the DST, i.e. it reveals the key characteristics and components of the reservoir flow systems.

We observed that the dual-porosity signature at early time (Figure 6.21) results from the exchange between the finite-conductivity fracture set and the surrounding low-permeability rock-type R1 (with $0.1mD$). This is somewhat surprising as we expect that the first exchange would be between the two fracture sets before the start of any contribution from the matrix. This simulated pressure response is most likely due to the distance of the infinite-conductivity fracture set to the producer, and considering that the fractures intersected by the producer is of finite conductivity with $F_{CD} = 5$. The low fracture conductivity implies that pressure gradient along the fracture length is significant (Cinco-Ley and Samaniego-V. 1981; Bourdet 2002) because of low fracture permeability. Cinco L. et al. (1978) and Bourdet (2002) stated that for finite conductivity where pressure drop along a fracture extension is not negligible, a second linear flow regime emerge from

the matrix perpendicular to the fracture plane before the series of linear flow within the fracture length reach the two ends of the fracture. This pressure behaviour they referred to as the bilinear flow regime. In this case, the two ends of the low permeability fracture intersected by the well is where the infinite conductivity fractures are located. Figure 5.14b and 5.15b show clearly that bilinear flow regime emerged before the effect of the infinite conductivity fractures was felt at the well. In the same way, the bilinear flow regime is expected for the field DST, at the early time, before the effect of the infinite-conductivity fracture set is felt at the producer. Hence, linear flow from the matrix in the near-well region should be expected at this early time. However, this early-time flow behaviour is not recognisable on the DST data and is masked by wellbore effect modelled on the simulated pressure derivatives from Figure 6.16b to Figure 6.20b. An increase in the conductivity of the finite-conductivity fracture set changes the flow dynamics and result in a significantly different pressure response where infinite-conductivity fracture flow dominates the pressure response from the onset. However, the recharge from the surrounding matrix into the producing fractures was not spontaneous because R1 has a low-permeability. The apparent delay in the surrounding matrix recharge thus yielded the first dual-porosity signature. With increase in matrix permeability, the first V-shape response will not be observed as shown in Figure 6.12b, 6.13b and 6.15. Shortly afterwards the effect of depletion of the infinite-conductivity fracture set reached the producer. Since fractures with the infinite conductivity have markedly higher conductivity than the fractures with finite conductivity and rock-type R1, we were able to reproduce the second dual-porosity signature. We have, however, shown that the conductivity contrast between the two fracture sets that produces the second dual-porosity signature is not able to fully match the observed pressure response. If R2 is present within $2m$ from the producer, a good match is obtained for the reservoir models presented. One other factor that enabled the agreement of the simulated pressure response and the field data is the distance of the fractures with infinite conductivity to the producer. The implies that a good match can still be obtained by tuning the later distance if the R2 distance to the producer increased.

The fluid exchange between the two fracture sets and rock-types R1 and R2 is complex but can be conceptualised in Figure 6.21. Our results suggest that most of the recharge from R2, which has the better reservoir properties compared to R1, reaches the infinite-conductivity fracture set and flows from there to the finite-conductivity fracture set intersected by the producer. We reckon that some of the recharge from R2 also reaches the fractures with finite conductivity where these fractures are located adjacent to R2 but away from the infinite-conductivity fracture set.

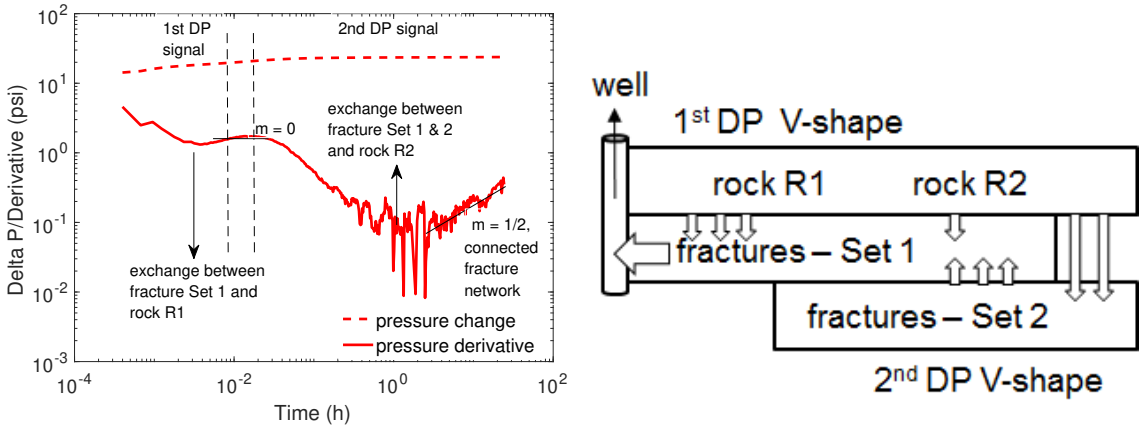

(a) (b)

Figure 6.21: Observed pressure data for Field X with an interpretation of the key reservoir components causing this particular pressure response (a) and schematic diagram illustrating the flow characteristic in Field X (b). DP denotes dual-porosity.

6.8 CHAPTER SUMMARY

In summary, we have successfully applied the geoengineering workflow described in Chapter 3 to a real field test. Using this workflow and the research findings in Chapter 4 and 5, different geological scenarios containing fractures and matrix were designed to reproduce multiple dual-porosity responses observed in DST data for Field X. Next, we eliminate the geological scenarios that are not consistent with other available data for Field X to ensure that the final model scenario is in agreement with the general geological understanding of the field. The results of the simulation model using Scenario 5 with a well that is intersecting fractures with finite conductivity in a reservoir containing both finite- and infinite-conductivity fractures was considered the most plausible geological scenario in consideration of the alternative geological scenarios. The calibration of the model with plausible geological scenario provided new insights into the reservoir geology and allow for a new interpretation of the flow behaviour in Field X. In addition, it is recommended that this thesis' interpretation of the DST data be integrated with the alternative interpretation that considered the potential impact of the gas cap in any future studies for completeness. Overall, this chapter provides novel reference solution for interpreting NFR where dual-porosity or multiple dual-porosity pressure signatures are present.

7

SUMMARY, CONCLUSION AND FUTURE WORK

7.1 SUMMARY

Geological well-testing is a valuable tool in reducing uncertainties that are inherent to fractured reservoirs and need to be captured in static reservoir models. Integration of both, dynamic well-testing data and static geological modelling, increases the understanding of complex fractured reservoirs and leads to better characterisation of these reservoirs. Usually, the pressure response from a production test correlates to the nature of the reservoir around the well and is essential to analyse the presence of heterogeneities and their consequences on reservoir performance, thus appraising the viability of a development project. In NFR, fractures often constitute the main heterogeneities, yet the pressure responses observed in the wells may not show the conventional well-test signatures or flow regimes for NFR. In order to better characterise a reservoir with well-test data, it is important to properly analyse and understand the diagnostic signatures of fracture flow.

The dual-porosity model is the key concept for simulating and interpreting pressure transient responses from NFR. However, several studies have highlighted that the pressure response corresponding to the dual-porosity model may not be appropriate for interpreting well-test data from all fractured reservoirs. To robustly and consistently analyse and quantify the limitations of the dual-porosity model when interpreting pressure transient data from NFR, we applied a geoengineering workflow using unstructured-PEBI grid and a DFM approach to simulate transient pressure responses and generate reference solutions for flow behaviour in vertically oriented fracture networks. We provide synthetic pressure transient responses for both simple and complex fracture geometries and for both idealised and realistic outcrop fracture patterns to ensure that all ranges of possible reservoir responses during the transition period are captured. This modelling approach provides new insights into reservoir features that cause the diagnostic dual-porosity signature (V-shape) and other unconventional fracture flow behaviour observed in well-test data from NFR.

Based on the numerical simulations and the results presented in preceding chapters, the following conclusions can be drawn from this thesis:

- Chapter 3 developed our geoengineering workflow with DFM modelling techniques using unstructured-grid reservoir simulations. The workflow was carefully validated and allows us to generate synthetic pressure transients for different fracture geometries. The workflow hence enabled us to correlate pressure responses observed in the reservoir to the known geological features in the reservoir model, which provides excellent calibration tool for simulation models and new insights into fundamental flow behaviours in fractured reservoirs.

- In Chapter 4 we demonstrated when the classic dual-porosity model response is valid for fracture networks with uniform conductivity and provided insights into the reservoirs features that cause the dual-porosity behaviours. For a well intersecting a fracture, the classical dual-porosity V-shape described by Warren and Root (1963) is caused by the following situations:

  i. The presence of fracture skin;

  ii. A tight matrix (less than $1mD$), similar to unconventional reservoirs (e.g. tight gas sands);

  iii. A well that intersects a small, unconnected fracture located near a single large fracture or a large fracture network;

  However, reservoirs can be fractured even if the dual-porosity V-shape is not visible in the well-test data. Overall, this chapter offers new insights into why the classical dual-porosity V-shape is observed in some NFR and absent in others.

- In Chapter 5 we showed how variable fracture conductivities and well locations impact the well-test response in NFR. The key outcomes of the study are that:

  i. The pressure responses due to variation in conductivity within and between different fractures and location of producers can be recognised in finite-conductivity fractures. However, these distinct pressure responses diminish with increasing fracture conductivity and may be undetectable in infinite-conductivity fractures;

  ii. The pressure transient response of the producer in two (or multiple) intersecting fractures with different conductivities is influenced at early times by the fracture that the well intersects; it only deviates at later time when

the effect of other fractures with infinite-conductivity begin to impact production;

iii. The simulated pressure behaviour for fractures with uniform and non-uniform apertures and conductivities can be significantly different, particularly for finite-conductivity fractures. None of the averaging techniques adequately capture the pressure responses for the fracture with variable conductivities;

iv. The pressure transient response of two intersecting fractures with different conductivities where the producer asymmetrically intersects a finite-conductivity fracture can be similar to that of a producer intersecting a fracture in a connected fracture network with uniform fracture conductivity;

v. A well-test carried out in a producer intersecting a finite-conductivity fracture in an NFR that comprises both finite- and infinite-conductivity fractures shows a dual-porosity V-shape that may otherwise be absent if the fracture network is assumed to have uniform conductivity.

This chapter explains why different pressure transient responses emerge in NFR with multiple fracture conductivities. It provides novel reference solutions for pressure transient responses in NFR for scenarios where fracture conductivities differ and locations of the producer within the fracture network varies. The chapter offers further insights to better characterise NFR where the unconventional pressure transient responses are often misinterpreted or completely missed, leading to detrimental impacts of fractures on production.

- In Chapter 6, we successfully applied the theoretical findings from Chapters 4 and 5 and the geoengineering workflow from Chapter 3 to provide new understanding about the flow system in a newly discovered fractured offshore carbonate reservoir. A reservoir model containing fractures and matrix was built and calibrated using the geoengineering workflow to match the complex pressure transients observed in the reservoir. Our simulation results provided new insights into reservoir geology and the key flow characteristics that lead to the emergence of a triple-porosity pressure transient in the well-test data. Although different geological scenarios could potentially explain the triple-porosity signature observed in the field, the combination with some basic reservoir data allowed us to rule out all but one concept, which could be readily and non-uniquely calibrated to obtain quantitative matches between the simulated and observed pressure transient data. Not only does this chapter demonstrate that the geoengineering workflow can be applied to improve the characterisation on NFR in a real field, we also provide novel reference

solution for interpreting NFR where dual-porosity or multiple dual-porosity pressure signatures are present.

7.3 RECOMMENDATIONS FOR FUTURE WORK

There are several options to extend and consequently improve the research work completed in this thesis. Some of these options can readily be exploited without modifications of the fracture meshing code developed for this study and using the open-sourced MRST simulator. Others would require further development of both the code and perhaps the simulation toolbox. Possible avenues for future research include, but are not limited to:

i. Interference well-tests and well-tests in horizontal wells. This research work considers a single, vertical well typically used for exploration or appraisal. Other tests, including interference tests and well-tests in horizontal/deviated wells, are carried out during the development and production stages. Investigation of the simulated pressure behaviour in such tests would improve the current research findings and perhaps provide additional information that could provide diagnostics to identify different fracture networks characteristics.

ii. Complex 3D fracture networks. All fracture simulation models considered in this thesis contain vertical fractures that fully penetrate the reservoir thickness. Future studies should analyse pressure responses for NFR with fracture networks that are more complex in the vertical direction, e.g. which contain both strata-bound and non-strata-bound fracture networks or joints and fracture corridors. This would provide further understanding on how pressure transients can differ from the results presented in this thesis if a producer intersects either the strata-bound or non-stratabound network in a reservoir containing both of the networks.

iii. Fracture skin. The reduction of permeability at the interface between fracture and matrix is currently assumed to be uniform and applied to all fractures present in the reservoir model. In reality, it is unlikely that all fractures in reservoir are affected by skin and for the skin to be uniformly distributed. Thus, it would be of practical benefit to further investigate the effect of variable fracture skin and degree of the skin to investigate if it can recognised in a well-test response.

iv. Heterogeneous matrix properties. Our simulation models assumed uniform and isotropic matrix properties. However, naturally fractured carbonate reservoirs often have very complex porosity and permeability distributions in the

rock matrix. This needs to be reflected in the simulation models to shed further light if the flow characteristics of complex multi-porosity systems, particularly triple-porosity systems, can be deciphered from transient pressure responses.

v. It is recommended that this thesis' interpretation of the Field X DST data presented in Chapter 6 should be integrated with the initial alternative interpretation that considered the potential impact of gas on the appraisal well pressure response.

REFERENCES

Abbaszadeh, M. and Cinco-Ley, H. (1995). Pressure-transient behavior in a reservoir with a finite-conductivity fault. *SPE Formation Evaluation*, 10(01):26 – 32.

Abdassah, D. and Ershaghi, I. (1986). Triple-Porosity Systems for Representing Naturally Fractured Reservoirs. *Spe Formation Evaluation*, (April):113–127.

Agada, S., Chen, F., Geiger, S., Toigulova, G., Agar, S., Benson, G., Shekhar, R., Hehmeyer, O., Amour, F., Mutti, M., Christ, N., and Immenhauser, A. (2013). Deciphering the Fundamental Controls of Flow in Carbonates Using Numerical Well-testing , Production Optimisation , & 3D High-res Outcrop Analogues for Fractured Carbonate Reservoir-. In *EAGE Annual Conference & Exhibition incorporating SPE Europec held in London, United Kingdom, 10-13 June 2013.*

Agada, S., Chen, F., Geiger, S., Toigulova, G., Agar, S., Shekhar, R., Benson, G., Hehmeyer, O., Amour, F., Mutti, M., Christ, N., and Immenhauser, A. (2014). Numerical simulation of fluid-flow processes in a 3D high-resolution carbonate reservoir analogue. *Petroleum Geoscience*, 20(1):125–142.

Agar, S. M., Geiger, S., and Matthäi, S. K. (2010). The Impact of Hierarchical Fracture Networks on Flow Partitioning in Carbonate Reservoirs : Examples Based on a Jurassic Carbonate Ramp Analog from the High Atlas , Morocco. *SPE Annual Technical Conference and Exhibition*, 2:1–19.

AGR Tracs (2014). Reservoir Engineering.

Aguilera, R. (1983). Exploring for naturally fractured reservoirs. In *SPWLA twenty-fourth annual logging symposium, June 27-30, 1983*.

Aguilera, R. (1995). *Naturally Fractured Reservoirs, Roberto Aguilera, 2nd edition.* PennWell Publishing Company.

Aguilera, R. (1998). Geologic aspects of naturally fractured reservoirs. *The Leading Edge*, 17(12):1667–1670.

Aguilera, R. (1999). Recovery factors and reserves in naturally fractured reservoirs. *Journal of Canadian Petroleum Technology*, 38(7):15–18.

Aguilera, R. (2003). Geologic and Engineering Aspects of Naturally Fractured Reservoirs. *CSEG Recorder*.

Aguilera, R. (2010). A method for estimating hydrocarbon cumulative production distribution of individual wells in naturally fractured carbonates, sandstones, shale gas, coalbed methane and tight gas formations. *Journal of Canadian Petroleum Technology*, 49(8):53–58.

Aguilera, R. and Van Poollen, H. K. (1977). Current status on the study of naturally fractured reservoirs.[214 references]. *The Log Analyst*, 13(3).

Ahmed, T. and McKinney, P. D. (2005). *Advanced resevoir engineering*. Gulf Professional Publishing.

Ahmed Elfeel, M. (2014). *Improved upscaling and reservoir simulation of enhanced oil recovery processes in naturally fractured reservoirs (Doctoral dissertation)*. Phd thesis, Heriot-Watt University.

Ahmed Elfeel, M. and Geiger, S. (2012). Static and Dynamic Assessment of DFN Permeability Upscaling. In *SPE Europec/EAGE Annual Conference*, number June, pages 4–7.

Al-Ghamdi, A. and Ershaghi, I. (1996). Pressure Transient Analysis of Dually Fractured Reservoirs. *SPE Journal*, 1(01):93–100.

Al Maqbali, A., Agada, S., Geiger, S., Haugen, Å., and Fernø, M. (2015). Modelling foam displacement in fractured carbonate reservoirs. *Society of Petroleum Engineers - Abu Dhabi International Petroleum Exhibition and Conference, ADIPEC 2015*.

Al-Mjeni, R., Arora, S., Cherukupalli, P., van Wunnik, J., Edwards, J., Felber, B., Gurpinar, O., Hirasaki, G. J., Miller, C. a., Jackson, C., Kristensen, M., Lim, F., and Ramamoorthy, R. (2010). Has the Time Come for EOR? *Oilfield Review*, 6(6):16–35.

Al-Thawad, F., Bin-Akresh, S., and Al-Obaid, R. (2001). Characterization of Fractures/Faults Network from Well Tests; Synergistic Approach. In *SPE Annual Technical Conference and Exhibition held in New Orleans, Louisiana, 30 September -3 October 2001*.

Al-Thawad, F. and Jamiolahmady, M. (2014). A Novel Semi-Analytical Solution for Transient Pressure Data Interpretation of a Fractured Well in an Asymmetric Reservoir. In *International Petroleum Technology Conference held in Kuala Lumpur, Malaysia, 10-12 December 2014*.

Ali, S. a., Clark, W. J., Moore, W. R., and Dribus, J. R. (2010). Diagenesis and Reservoir Quality. *Oilfield Review*, 22(2, Summer):14–27.

Aljuboori, F., Corbett, P., Bisdom, K., Bertotti, G., and Geiger, S. (2015). Using Outcrop Data for Geological Well Test Modelling in Fractured Reservoirs. *77th EAGE Conference and Exhibition 2015*, (June 2015):1–4.

Allan, J. and Sun, S. Q. (2003). Controls on Recovery Factor in Fractured Reservoirs: Lessons Learned from 100 Fractured Fields. In *Proceedings of SPE Annual Technical Conference and Exhibition held in Denver, Colorado, U.S.A., 5-8 October 2003*.

Arnold, D., Demyanov, V., Christie, M., Bakay, A., and Gopa, K. (2016). Optimisation of decision making under uncertainty throughout field lifetime: A fractured reservoir example. *Computers and Geosciences*, 95:123–139.

Bahrainian, S. S., Dezfuli, A. D., and Noghrehabadi, A. (2015). Unstructured grid generation in porous domains for flow simulations with discrete-fracture network model. *Transport in Porous Media*, 109(3):693–709.

Barenblatt, G., Zheltov, I., and Kochina, I. (1960). Basic concepts in the theory of seepage of homogeneous liquids in fissured rocks [strata]. *Journal of Applied Mathematics and Mechanics*, 24(5):1286–1303.

Belani, A. K. and Jalali, Y. (1988). Estimation of Matrix Block Size Distribution in Naturally Fractured Reservoirs.

Beliveau, D., Payne, D., and Mundry, M. (1993). Waterflood and CO2 Flood of the Fractured Midale Field (includes associated paper 22947). *Journal of Petroleum Technology*, 45(9):881–887.

Bentley, M. (2015). Modelling for comfort? *Petroleum Geoscience*, pages 2014–089.

Bentley, M., Oxlade, R., and Murison, M. (2017). Carbonate reservoir modelling and simulation workshop, Provence, France.

Berkowitz, B. (2002). Characterizing flow and transport in fractured geological media: A review. *Advances in Water Resources*, 25(8-12):861–884.

Bertotti, G., Bisdom, K., van Eijk, M., Hameka, F., Vis, A., Bezerra, H., and Reijmer, J. (2014). Fractures and fracture networks in carbonate reservoirs: A geological perspective. In *AAPG International Conference & Exhibition, 14-17 September 2014*, Istanbul, Turkey.

Bertotti, G., de Graaf, S., Bisdom, K., Oskam, B., B. Vonhof, H., H. R. Bezerra, F., J. G. Reijmer, J., and L. Cazarin, C. (2017). Fracturing and fluid-flow during post-rift subsidence in carbonates of the Jandaíra Formation, Potiguar Basin, NE Brazil. *Basin Research*, pages 1–18.

Berumen, S., Tiab, D., and Rodriguez, F. (2000). Constant rate solutions for a fractured well with an asymmetric fracture. *Journal of Petroleum Science and Engineering*, 25(1):49–58.

Bisdom, K., Bertotti, G., and Bezerra, F. (2017a). Inter-well scale natural fracture geometry and permeability variations in low-deformation carbonate rocks. *Journal of Structural Geology*, 97:23–36.

Bisdom, K., Bertotti, G., and Nick, H. M. (2016). The impact of different aperture distribution models and critical stress criteria on equivalent permeability in fractured rocks. *Journal of Geophysical Research: Solid Earth*, 119:8132–8153.

Bisdom, K., Nick, H., and Bertotti, G. (2017b). An integrated workflow for stress and flow modelling using outcrop-derived discrete fracture networks. *Computers & Geosciences*, 103:21–35.

Bogdanov, I. I., Mourzenko, V. V., Thovert, J.-F., and Adler, P. M. (2003). Pressure drawdown well tests in fractured porous media. *Water Resources Research*, 39(1).

Bosma, S. B. M., Hajibeygi, H., and Tene, M. (2017). Multiscale Finite Volume Method for Discrete Fracture Modeling with Unstructured Grids. In *Paper prepared for presentation at the SPE Reservoir Simulation Conference held in Montgomery, TX, USA, 20-22 February 2017*.

Boulton, N. S. and Streltsova, T. D. (1977). Unsteady flow to a pumped well in a fissured water-bearing formation. *Journal of Hydrology*, 35(3):257–270.

Bourbiaux, B. (2010). Fractured Reservoir Simulation: a Challenging and Rewarding Issue. *Oil & Gas Science and Technology - Rev. IFP*, 65(2):227–238.

Bourbiaux, B., Nguyen, Q.-l., Robin, M., and Rosenberg, E. (2015). Experimental and Numerical Assessment of Chemical Enhanced Oil Recovery in Oil-Wet Naturally Fractured Reservoirs. (June):1–14.

Bourdet, D. (2002). *Well Test Analysis: the Use of Advanced Interpretation Models Handbook of Petroleum Exploration and Production Vol 3*. Elsevier, first edition.

Bourdet, D., Ayoub, J., and Kniazeff, V. (1983). Interpreting well tests in fractured reservoirs. *World Oil;(United States)*, 197(5):77–87.

Bourdet, D., Ayoub, J. A., and Pirard, Y. M. (1989). Use of pressure derivative in well test interpretation. *SPE Formation Evaluation*, 4(02):293–302.

Bourdet, D. and Gringarten, A. C. (1980). Determination of fissure volume and block size in fractured reservoirs by type-curve analysis. In *SPE Annual Technical Conference and Exhibition, 21-24 September 1980, Dallas, Texas*.

Branets, L. V., Ghai, S. S., Lyons, S. L. L., and Wu, X.-H. (2009). Challenges and technologies in reservoir modeling. *Communications in Computational Physics*, 6(1):1–23.

Bratton, T., Gillespie, P., Li, B., Marcinew, R., Ray, S., Nelson, R., Schoderbek, D., and Sonneland, L. (2006). The Nature of Naturally Fractured Reservoirs.

Brown, J. S. (2010). Innovation for the Long Run. pages 1–7.

Bush, I. (2010). An Integrated Approach to Fracture Characterisation. *Oil Review Middle East*, 2:88–91.

Chen, Z.-X. (1989). Transient flow of slightly compressible fluids through double porosity, double-permeability systems - a state-of-the-art review. *Transport in Porous Media*, 4(2):147–184.

Cinco L., H., Samaniego V., F., and Dominguez A., N. (1978). Transient Pressure Behavior for a Well With a Finite-Conductivity Vertical Fracture. *Society of Petroleum Engineers Journal*, 18(04):253–264.

Cinco-Ley, H. (1996). Well-testing analysis for naturally fractured reservoirs. *Journal of Petroleum Technology*, 48(01):51–54.

Cinco-Ley, H. and Samaniego, V. F. (1977). Effect of wellbore storage and damage on the transient pressure behavior of vertically fractured wells. In *SPE Annual Fall Technical Conference and Exhibition, 9-12th Oct 1977*.

Cinco-Ley, H. and Samaniego, V. F. (1982). Pressure transient analysis for naturally fractured reservoirs. In *SPE Annual Technical Conference and Exhibition, 26-29 Sept. 1982*.

Cinco-Ley, H., Samaniego, V. F., and Kucuk, F. (1985). The pressure transient behavior for naturally fractured reservoirs with multiple block size. In *SPE Annual Technical Conference and Exhibition, 22-25 September 1985*.

Cinco-Ley, H. and Samaniego-V., F. (1981). Transient pressure analysis for fractured wells. *Journal of Petroleum Technology*, 33(09):1749–1766.

Cinco-Ley, H., Samaniego V., F., and Dominguez A., N. (1976). Unsteady-state flow behavior for a well near a natural fracture. In *SPE Annual Fall Technical Conference and Exhibition, 3-6 Oct. 1976*.

Clossman, P. (1975). An Aquifer Model for Fissured Reservoirs. *Society of Petroleum Engineers Journal*, 15(05):385–398.

Committee on Fracture Characterization and Fluid Flow (1996). *Rock Fractures and Fluid Flow: Contemporary Understanding and Applications*. The National Academies Press, Washington, DC.

Corbett, P., Zheng, S.-y., Pinisetti, M., Mesmari, A., and Stewart, G. (1998). The Integration of Geology and Well Testing for Improved Fluvial Reservoir Characterisation. *SPE International Conference and Exhibition*, 52:471–488.

Corbett, P. W. M. (2009). *Petroleum Geoengineering: Integration of Static and Dynamic Models, SEG/EAGE Distinguished Instructor Short Course*. Distinguished instructor series, 12. SEG Books, 2009.

Corbett, P. W. M. (2012). The role of geoengineering in oilfield development. In Gomes, J. S., editor, *New Technologies in the Oil and Gas Industry*. Intech E-Book.

Corbett, P. W. M., Couples, G. D., and Gardiner, A. (2013). Petroleum Geoscience.

Corbett, P. W. M., Geiger, S., Borges, L., Garayev, M., and Valdez, C. (2012). "The third porosity system: understanding the role of hidden pore systems in well-test interpretation in carbonates". *Petroleum Geoscience*, 18(1):73–81.

de Graaf, S., Reijmer, J. J., Bertotti, G. V., Bezerra, F. H., Cazarin, C. L., Bisdom, K., and Vonhof, H. B. (2017). Fracturing and calcite cementation controlling fluid flow in the shallow-water carbonates of the Jandaíra Formation, Brazil. *Marine and Petroleum Geology*, 80:382–393.

de Swaan O., A. (1976). Analytic solutions for determining naturally fractured reservoir properties by well testing. *Society of Petroleum Engineers Journal*, 16(03):117–122.

Dean, R. H. and Lo, L. L. (1988). Simulations of Naturally Fractured Reservoirs. *SPE Reservoir Engineering*, 3(02):638–648.

Deng, H., Liu, Y., Peng, X., Liu, Y., and Li, H. A. (2018). A new index used to characterize the near-wellbore fracture network in naturally fractured gas reservoirs. *Journal of Natural Gas Science and Engineering*, 55(November 2017):52–63.

Earlougher, R. J. (1977). Advances in Well Test Analysis, SPE Monograph Series.

Egya, D., Geiger, S., Corbett, P., Norgard, J. P., Hegndal-Andersen, S., and Sundal, L. (2018a). New calibration of fracture properties using geological well-testing. In *Third EAGE Workshop on Naturally Fractured Reservoirs held in Muscat, Oman, 5-7th Feb. 2018*.

Egya, D., Geiger, S., and Corbett, P. W. M. (2018b). Effect of Variation in Fractures Conductivity and Well Location on Pressure Transient Response from

Fractured Reservoirs. In *This paper was prepared for presentation at the SPE EUROPEC featured at the 80th EAGE Annual Conference & Exhibition to be held in Copenhagen, Denmark, 11-14 June 2018. SPE-190884-MS.*

Egya, D. O., Geiger, S., Corbett, P. W. M., March, R., Bisdom, K., Bertotti, G., and Bezerra, F. H. (2018c). Analysing the limitations of the dual-porosity response during well tests in naturally fractured reservoirs. *Petroleum Geoscience*.

Elkins, L. F. (1953). Reservoir performance and well spacing, Spraberry Trend area field ow West Texas. *Society of Petroleum Engineers*, 198(07):177–196.

Fekete.com (2015). Well Testing Fundamentals.

Fernø, M. (2012). Enhanced Oil Recovery in Fractured Reservoirs. *Introduction to Enhanced Oil Recovery (EOR) Processes and Bioremediation of Oil - Contaminated Sites*, pages 89–110.

Firoozabadi, A. (2000). Recovery mechanisms in fractured reservoirs and field performance. *Journal of Canadian Petroleum Technology*, 39(11):13–17.

Flemisch, B., Berre, I., Boon, W., Fumagalli, A., Schwenck, N., Scotti, A., Stefansson, I., and Tatomir, A. (2017). Benchmarks for single-phase flow in fractured porous media. *Advances in Water Resources*, 111(January 2017):239–258.

Friedel, T. (2004). Numerical Simulation of Production from Tight Gas Reservoirs by Advanced Stimulation Technologies. *Faculty of Geosciences, Geotechnology & Mining*, Doctor-Eng:126.

Gale, J. F. W., Laubach, S. E., Olson, J. E., Eichhubl, P., and Fall, A. (2014). Natural fractures in shale: A review and new observations. *AAPG Bulletin*, 98(September 2015):2165–2216.

Geiger, S., Dentz, M., and Neuweiler, I. (2013). A novel multi-rate dual-porosity model for improved simulation of fractured and multiporosity reservoirs. *SPE Journal*, 18(4):670–684.

Geiger, S. and Emmanuel, S. (2010). Non-Fourier thermal transport in fractured geological media. *Water Resources Research*, 46(7):1–13.

Geiger, S. and Matthäi, S. (2014). What can we learn from high-resolution numerical simulations of single- and multi-phase fluid flow in fractured outcrop analogues? *Geological Society, London, Special Publications*, 374(01):125–144.

Geiger, S., Matthäi, S., Niessner, J., and Helmig, R. (2009). Black-oil simulations for three-component, three-phase flow in fractured porous media. *SPE Journal*, 14(2):338–354.

Gilman, J. R. (2003). Practical Aspects of Simulation of Fractured Reservoirs. In *International Forum on Reservoir Simulation, Bühl, Germany, June 23-27, 2003*.

Gong, B., Karimi-Fard, M., and Durlofsky, L. J. (2013). Upscaling Discrete Fracture Characterizations to Dual-Porosity, Dual-Permeability Models for Efficient Simulation of Flow With Strong Gravitational Effects. *SPE Journal*, 13(01):58–67.

Gonzalez-Chavez, M. A. and Cinco-Ley, C. (2006). Effect of Pressure in a Well With a Vertical Fracture With Variable Conductivity and Skin Fracture. (1):1–11.

Gringarten, A. C. (1984). Interpretation of tests in fissured and multilayered reservoirs with double porosity behavior: theory and practice. *Journal of Petroleum Technology*, 36(04):549–564.

Gringarten, A. C. (1987). How to recognize 'double-porosity' systems from well tests. *Journal of Petroleum Technology*, 39(6):631–633.

Gringarten, A. C. (1998). Evolution of Reservoir Management Techniques : From Independent Methods to an Integrated Methodology . Impact on Petroleum Engineering Curriculum , Graduate Teaching and Competitive Advantage of Oil Companies. In *SPE Asia Pacific Conference on Integrated Modelling for Asset Managemen*, number 2, pages 1–8.

Gringarten, A. C., Ramey, H. J., and Raghavan, R. (1974). Unsteady-state pressure distributions created by a well with a single infinite-conductivity vertical fracture. *Society of Petroleum Engineers Journal*, 14(04):347–360.

Gringarten, A. C., Ramey Jr, H. J. ., and Raghavan, R. (1975). Applied pressure analysis for fractured wells. *Journal of Petroleum Technology*, 27(07):887–892.

Groves, D. L. and Abernathy, B. F. (1968). Early Analysis of Fractured Reservoirs Compared to Later Performance. In *43rd Annual Fall Meeting of the Society of Petroleum Engineers of AIME, held in Houston, Tex., Sept. 29th - Oct. 2, 1968. SPE 2259*.

Haile, B. G., Klausen, T. G., Czarniecka, U., Xi, K., Jahren, J., and Hellevang, H. (2017). How are diagenesis and reservoir quality linked to depositional facies? A deltaic succession, Edgeøya, Svalbard. *Marine and Petroleum Geology*, (August).

Hajibeygi, H., Karvounis, D., and Jenny, P. (2011). A hierarchical fracture model for the iterative multiscale finite volume method. *Journal of Computational Physics*, 230(24):8729–8743.

Hardebol, N. J., Maier, C., Nick, H., Geiger, S., Bertotti, G., and Boro, H. (2015). Multiscale fracture network characterisation and impact on flow. *Journal of Geophysical Research : Solid Earth*, 120(12):8197–8222.

Heinemann, Z. E. and Mittermeir, G. (2014). *Natural Fractured Reservoir Engineering*. Number February.

Hooker, J. N., Laubach, S. E., and Marrett, R. (2013). Fracture-aperture sized-frequency, spatial distribution, and growth processes in strata-bounded and non-strata-bounded fractures, cambrian mesón group, NW argentina. *Journal of Structural Geology*, 54:54–71.

Houze, O., Viturat, D., and Fjaere, O. S. (2017). *KAPPA Dynamic Data Analysis v5.12.01*.

Howell, J. A., Martinius, A. W., Good, T. R., Howell, J. A., Martinius, A. W., and Good, T. R. (2014). The application of outcrop analogues in geological modelling : a review , present status and future outlook. In Martinius, A. W., Howell, J. A., and Good, T. R., editors, *Sediment-Body Geometry and Heterogeneity: Analogue Studies for Modelling the Subsurface*, pages 1–25. Geological Society, London, Special Publications, 387.

Huskey, W. L. and Crawford, P. B. (1967). Performance of petroleum reservoirs containing vertical fractures in the matrix. *Society of Petroleum Engineers*, 7(02).

Hyman, J. D., Gable, C. W., Painter, S. L., and Makedonska, N. (2014). Conforming delaunay triangulation of stochastically generated three dimensional discrete fracture networks : a feature rejection algorithm for meshing strategy. *SIAM J. SCI. COMPUT.*, 36(4):1871–1894.

Kamal, M. M. and Co, A. P. (1986). Effects of Wellbore Storage and Skin on Vertical · Permeability Testing ·· I. (October):481–496.

Karimi-Fard, M., Durlofsky, L. J., and Aziz, K. (2004). An efficient discrete-fracture model applicable for general-purpose reservoir simulators. *SPE Journal*, 9(02):227–236.

Kazemi, H. (1969). Pressure transient analysis of naturally fractured reservoirs with uniform fracture distribution. *Society of Petroleum Engineers Journal*, 9(04):451 – 462.

Kazemi, H. and Gilman, J. R. (1993). Multiphase flow in fractured petroleum reservoirs. In J. Bear, C. F. Tsang, and G. de Marsily, E., editor, *Flow and Contaminant Transport in Fractured Rocks*, pages 267–323. Academic Press, New York.

Kazemi, H., Merrill Jr, L., Porterfield, K., and Zeman, P. (1976). Numerical Simulation of Water-Oil Flow in Naturally Fractured Reservoirs. *Society of Petroleum Engineers Journal*, 16(6):317–326.

Kazemi, H., Seth, M. S., and Thomas, G. W. (1969). The interpretation of interference tests in naturally fractured reservoirs with uniform fracture distribution. *Society of Petroleum Engineers Journal*, 9(4):463–472.

Kim, J.-G. and Deo, M. D. (2000). Finite element, discrete-fracture model for multiphase flow in porous media. *AlChE Journal*, 46(6):1120–1130.

Krevor, S. and Fitch, P. (2015). Carbonate Reservoir Evaluation 21. (April).

Kuchuk, F. and Biryukov, D. (2014). Pressure-transient behavior of continuously and discretely fractured reservoirs. *SPE Reservoir Evaluation & Engineering*, 17(01):82–97.

Kuchuk, F. and Biryukov, D. (2015). Pressure-transient tests and flow regimes in fractured reservoirs. *SPE Reservoir Evaluation and Engineering*, 18(02):187–204.

Kuchuk, F., Biryukov, D., and Fitzpatrick, T. (2014). *Fractured Reservoir Modeling and Interpretation*. Number December.

Kuchuk, F., Biryukov, D., and Fitzpatrick, T. (2015). Fractured-reservoir modeling and interpretation. *SPE Journal*, 20(05):983–1,004.

Kuchuk, F. J. and Biryukov, D. (2012). Transient Pressure Test Interpretation for Continuously and Discretely Fractured Reservoirs. In *Proceedings of SPE Annual Technical Conference and Exhibition held in San Antonio, Texas, USA, 8-10 October 2012.*

Lake, L. W., Schmidt, R. L., and Venuto, P. B. (1992). A Niche for Enhanced Oil Recovery in the 1990s. *Oilfield Review*, 17(January):62–67.

Lawry, T. F. (1946). Channeling in Water Flooding. *SPE J*, (2):221–227.

Lemonnier, P. and Bourbiaux, B. (2010a). Simulation of naturally fractured reservoirs. state of the art - part 1 - physical mechanisms and simulator formulation. *Oil & Gas Science and Technology - Rev. IFP*, 65(2):239–262.

Lemonnier, P. and Bourbiaux, B. (2010b). Simulation of naturally fractured reservoirs. state of the art - part 2 - matrix-fracture transfers and typical features of numerical studies. *Oil & Gas Science and Technology - Rev IFP*, 65(2):263–286.

Li, L. and Lee, S. H. (2008). Efficient Field-Scale Simulation of Black Oil in a Naturally Fractured Reservoir Through Discrete Fracture Networks and Homogenized Media. *SPE Reservoir Evaluation & Engineering*, 11(04):750–758.

Lie, K. A., Krogstad, S., Ligaarden, I. S., Natvig, J. R., Nilsen, H. M., and Skaflestad, B. (2012). Open-source MATLAB implementation of consistent discretisations on complex grids. *Computational Geosciences*, 16(2):297–322.

Luo, W., Liu, P., Tian, Q., Tang, C., and Zhou, Y. (2017). Effects of discrete dynamic-conductivity fractures on the transient pressure of a vertical well in a closed rectangular reservoir. *Scientific Reports*, 7(1):1–12.

Maier, C. (2014). Improved Simulations of Naturally Fractured Reservoirs Using Unstructured Grids and Multi-Rate Dual-Porosity Models. (November).

Makel, G. H. (2007). The modelling of fractured reservoirs: constraints and potential for fracture network geometry and hydraulics analysis. *Geological Society, London, Special Publications*, 292:375–403.

Mallison, B. T., Hui, M. H., and Narr, W. (2010). Practical Gridding Algorithms for Discrete Fracture Modeling Workflows. In *ECMOR XII, 12th European Conference on the Mathematics of Oil Recovery, 6-9 September 2010, Oxford, UK*, number September 2010, pages 1–11.

Mavor, M. and Cinco-Ley, H. (1979). Transient pressure behavior of naturally fractured reservoirs. In *SPE California Regional Meeting, 18-20 April 1979*.

Moench, A. F. (1984). Double-porosity models for a fissured groundwater reservoir with fracture skin. *Water Resources Research*, 20(07):831–846.

Moinfar, A., Varavei, A., Sepehrnoori, K., and Johns, R. T. (2013). Development of a Coupled Dual Continuum and Discrete Fracture Model for the Simulation of Unconventional Reservoirs. In *SPE Reservoir Simulation Symposium held in the Woodlands, Texas USA, 18-20 February 2013*.

Monsen, E., Pedersen, S. I., Bounaim, A., Nickel, M., Savary, B., Brenna, T., Tjostheim, B., Sonneland, L., Hunt, D., Gillespie, P., and Thurmond, J. (2006). Quantitative 3D outcrop interpretation. In *2006 SEG/New Orleans Annual Meeting. Society of Exploration Geophysicists*, pages 1043–1047.

Monteagudo, J. E. P. and Firoozabadi, A. (2004). Control-volume method for numerical simulation of two-phase immiscible flow in two- and three-dimensional discrete-fractured media. *Water Resources Research*, 40(7):1–20.

Morton, K. L., Booth, R. J. S., Chugunov, N., Biryukov, D., Fitzpatrick, A. F., and Kuchuk, F. J. (2013). Global sensitivity analysis for natural fracture geological modeling parameters from pressure transient tests. In *EAGE Annual Conference & Exhibition incorporating SPE Europec held in London, United Kingdom, 10-13 June 2013.*, number SPE-164894.

Morton, K. L., Kuchuk, F. J., and Fitzpatrick, A. J. (2015). Active and Interference Well Pressure Transient Data Interpretation in Naturally Fractured Reservoirs. In *77th EAGE Conference and Exhibition 1-4 June 2015*, number We N118 02.

Morton, K. L., Nogueira, P. d. B., Booth, R. J. S., and Kuchuk, F. (2012). Integrated Interpretation for Pressure Transient Tests in Discretely Fractured Reservoirs. In *74th EAGE Conference & Exhibition incorporating SPE EUROPEC 2012 Copenhagen, Denmark, 4-7 June 2012*, pages 4–7.

Møyner, O. and Lie, K.-A. (2016). A multiscale restriction-smoothed basis method for high contrast porous media represented on unstructured grids. *Journal of Computational Physics*, 304:46–71.

Najurieta, H. L. (1980). A theory for pressure transient analysis in naturally fractured reservoirs. *Journal of Petroleum Technology*, 32(07):1–241.

Narr, W., Schechter, D. S., and Thompson, L. B. (2006). *Naturally Fractured Reservoir Characterization*. Richardson, Tex. : Society of Petroleum Engineers.

Nelson, R. A. (2001). *Geologic analysis of naturally fractured reservoirs*. Gulf Professional Publishing.

Nogueira, P. D. B., Morton, K., Kuchuk, F., and Booth, R. (2013). Integrated workflow characterizes Campos basin fractured reservoirs using pressure-transient tests. *World Oil*, 234(2):103–106.

Nurmi, R., Akbar, M., Standen, E., Sharma, S., Panwar, P., Chaturvedi, J. G., and Dennis, B. (1993). Finding Fractures in deep and Tight Rocks. *Middle East Well Evaluation Review*, (November):25–43.

Odeh, A. S. (1965). Unsteady-state behavior of naturally fractured reservoirs. *Society of Petroleum Engineers Journal*, 5(1):60–66.

Odling, N. E. (1997). Scaling and connectivity of joint systems in sandstones from western Norway. *Journal of Structural Geology*, 19(10):1257–1271.

Olorode, O. M., Freeman, C. M., Moridis, G. J., and Blasingame, T. A. (2013). High-resolution numerical modeling of complex and irregular fracture patterns in shale-gas reservoirs and tight gas reservoirs. *SPE Reservoir Evaluation & Engineering*, 16(04):443–455.

Paillet, F. L. (1994). Application of Borehole Geophysics in the Characterization of Flow in Fractured Rocks - Water-Resources Investigations Report 93-4214. Technical report, U.S. Geological Survey.

Pirson, S. J. (1953). Performance of fractured oil reservoirs. *Bulletin of the American Association of Petroleum Geologists*, 37(2):232–244.

Pruess, K. (1990). Modeling of geothermal reservoirs: Fundamental processes, computer simulation and field applications. *Geothermics*, 19(1):3–15.

Ramsey, J. M. and Chester, F. M. (2004). Hybrid fracture and the transition from extension fracture to shear fracture. *Nature*, 428(6978):63–6.

Restrepo, D. P. and Tiab, D. (2009). Multiple fractures transient response. In *2009 SPE Latin American and Caribbean Petroleum Engineering Conference Proceedings, 31 May - 3 June in Cartagena, Colombia.*

Ringrose, P. and Bentley, M. (2015). *Reservoir Model Design*.

Rogers, S., Enachescu, C., Trice, R., and Buer, K. (2007). Integrating discrete fracture network models and pressure transient data for testing conceptual fracture models of the Valhall chalk reservoir, Norwegian North Sea. *Fractured Reservoirs*, 270(June):193–204.

Saidi, A. M. (1987). Reservoir Engineering of Fractured Reservoirs.

Salimi, S. and Alikarami, R. (2006). Mechanism of Fluid Invasion in Naturally Fractured Reservoirs: Experimental Study. *SPE International Symposium and Exhibition on Formation Damage Control*.

Schlumberger (2008). Characterization of Fractured Reservoirs: Reliable, predictive models to optimize carbonate reservoir performance.

Schmid, K. S. and Geiger, S. (2013). Universal scaling of spontaneous imbibition for arbitrary petrophysical properties: Water-wet and mixed-wet states and Handy's conjecture. *Journal of Petroleum Science and Engineering*, 101:44–61.

Seers, T. D. and Hodgetts, D. (2013). Comparison of digital outcrop and conventional data collection approaches for the characterization of naturally fractured reservoir analogues. In Spence, G. H., Redfern, J., Aguilera, R., Bevan, T. G., Cosgrove, J. W., Couples, G. D., and Daniel, J.-M., editors, *Advances in the study of fractured reservoirs*, volume 374, pages 51–77. Geological Society, London, Special Publications, 374.

Serra, K., Reynolds, A., and Raghavan, R. (1983). New Pressure Transient Analysis Methods for Naturally Fractured Reservoirs. *Journal of Petroleum Technology*, 35(12):2271–2283.

Shewchuck, J. (2002). Delaunay refinement algorithms for triangular mesh generation. *Applied Computational Geometry*, 22(01):21–74.

Singh, R. and Mohanty, K. K. (2016). Foams With Wettability-Altering Capabilities for Oil-Wet Carbonates: A Synergistic Approach. *SPE Journal*, 21(04):1126–1139.

Snow, S. and Brownlee, M. (1989). Practical and Theoretical Aspects of Well Testing in the Ekofisk Area Chalk Fields. In *64th SPE Annual Technical Conference and Exhibition held in San Antonio, TX, October 8-11, 1989*.

Spence, G. H., Redfern, J., Aguilera, R., Bevan, T. G., Cosgrove, J. W., Couples, G. D. &., and Daniel, J.-M., editors (2014). *Advance in the Study of Fractured Reservoirs*. Geological Society, London, special pu edition.

Stearns, D. W. and Friedman, M. (1969). Reservoirs in Fractured Rock. *in R. E. King, ed., Stratigraphic oil and gas fields-Classification, exploration methods, and case histories: AAPG Memoir 16/Society of Exploration Geophysicists Special Publication 10*, pages 82–106.

Stewart, G. (2014). Well Testing in Carbonate Formations, IPTC-18078. In *International Petroleum Technology Conference held in Kuala Lumpur, Malaysia, 10-12 December 2014*.

Streltsova, T. D. (1983). Well pressure behavior of a naturally fractured reservoir. *Society of Petroleum Engineers Journal*, 23(05):769–780.

Streltsova, T. V. (1976). Hydrodynamics of Groundwater Flow in Fractured Formations. *Water Resources Research*, 12(3):405–414.

Sun, J. and Schechter, D. (2015). Optimization-based unstructured meshing algorithms for simulation of hydraulically and naturally fractured reservoirs with variable distribution of fracture aperture, spacing, length and strike. *SPE Reservoir Evaluation & Engineering*, 18(04):463–480.

Sun, J., Schechter, D., and Rui, Z. (2016). Numerical Investigation of the Effect of Nonuniform Fracture Aperture of Eagle Ford Outcrop Maps on Production Performance. In *This paper was prepared for presentation at the SPE Annual Technical Conference and Exhibition held in Dubai, UAE, 26-28 September 2016.*

Swaby, P. and Rawnsley, K. (1996). An interactive 3D fracture modelling environment. *Petroleum Computer Conference*.

Syihab, Z. (2009). *Simulation of discrete fracture netmowrk using flexible voronoi gridding (Doctoral dissertation)*. PhD thesis, Texas A&M University.

Tiab, D. and Donaldson, E. C. (2016). Chapter 8 - Naturally Fractured Reservoirs. In *Petrophysics. Theory and Practice of Measuring Reservoir Rock and Fluid Transport Properties.*, pages 415–481. Petrophysi edition.

Trivedi, J. J. and Babadagli, T. (2008). Experimental Investigations on the Flow Dynamics and Abandonment Pressure for CO 2 Sequestration and Incremental Oil Recovery in Fractured Reservoirs: The Midale Field Case - ABSTRACT. *Canadian International Petroleum Conference*, (1):1.

Valdes-perez, A. R., Pulido, H., Cinco-Ley, H., and Galicia-muñoz, G. (2011). a new bilinear flow model for naturally fractured reservoirs with transient interporosity transfer. In *PROCEEDINGS, Thirty-Sixth Workshop on Geothermal Reservoir Engineering Stanford University, Stanford, California, January 31 - February 2, 2011*.

Vasilev, I., Alekshakhin, Y., and Kuropatkin, G. (2016). Pressure Transient Behavior in Naturally Fractured Reservoirs: Flow Anaysis (Russian). *SPE Annual Caspian Technical Conference & Exhibition*.

Wanjing, L. and Changfu, T. (2014). Pressure-transient analysis of multiwing fractures connected to a vertical wellbore. *SPE Journal*, 20(02):360–367.

Warren, G. (1993). Numerical solutions for pressure transient analysis. *SPE Gas Technology Symposium*.

Warren, J. E. and Root, P. J. (1963). The behavior of naturally fractured reservoirs. *Society of Petroleum Engineers Journal*, 3(03):245–255.

Wei, L., Hadwin, J., Chaput, E., Rawnsley, K., and Swaby, P. (1998). Discriminating fracture patterns in fractured reservoirs by pressure transient tests. In *SPE Annual Technical Conference and Exhibition, New Orleans, Lousiana, U.S.A., 27-30 September 1998, SPE 49233*.

Wennberg, O. P., Casini, G., Jonoud, S., and Peacock, D. C. (2016). The characteristics of open fractures in carbonate reservoirs and their impact on fluid flow: a discussion. *Petroleum Geoscience*, pages 2015–003.

Whittle, T. (2017). Pressure Transient Analysis. In *Course note of SPE Europec featured at the 79th EAGE Conference and Exhibition presented on 12th June 2017 in Paris, France.*

Wong, D. W., Harrington, A. G., and Cinco-Ley, H. (1986). Application of the pressure derivative function in the pressure transient testing of fractured wells. *SPE Formation Evaluation*, 1(5):470–480.

Zheng, S. Y., Legrand, V. M., and Corbett, P. W. M. (2007). Geological model evaluation through well test simulation : a case study from the Wytch farm oilfield , southern England. *Journal of Petroleum Geology*, 30(01):41–58.

Zhou, F., Shi, A., and Wang, X. (2014). An efficient finite difference model for multiphase flow in fractured reservoirs. *Petroleum Exploration and Development*, 41(2):262–266.